

Numerical Study of Primary Breakup of Liquid Sheets

Mohammad Movassat

A Thesis

in

Department of

Mechanical and Industrial Engineering

Presented in Partial Fulfillment of the Requirements

for the Degree of Master of Applied Science at

Concordia University

Montreal, Quebec, Canada

July 2007

© Mohammad Movassat, 2007



Library and
Archives Canada

Bibliothèque et
Archives Canada

Published Heritage
Branch

Direction du
Patrimoine de l'édition

395 Wellington Street
Ottawa ON K1A 0N4
Canada

395, rue Wellington
Ottawa ON K1A 0N4
Canada

Your file Votre référence

ISBN: 978-0-494-34448-4

Our file Notre référence

ISBN: 978-0-494-34448-4

NOTICE:

The author has granted a non-exclusive license allowing Library and Archives Canada to reproduce, publish, archive, preserve, conserve, communicate to the public by telecommunication or on the Internet, loan, distribute and sell theses worldwide, for commercial or non-commercial purposes, in microform, paper, electronic and/or any other formats.

The author retains copyright ownership and moral rights in this thesis. Neither the thesis nor substantial extracts from it may be printed or otherwise reproduced without the author's permission.

AVIS:

L'auteur a accordé une licence non exclusive permettant à la Bibliothèque et Archives Canada de reproduire, publier, archiver, sauvegarder, conserver, transmettre au public par télécommunication ou par l'Internet, prêter, distribuer et vendre des thèses partout dans le monde, à des fins commerciales ou autres, sur support microforme, papier, électronique et/ou autres formats.

L'auteur conserve la propriété du droit d'auteur et des droits moraux qui protègent cette thèse. Ni la thèse ni des extraits substantiels de celle-ci ne doivent être imprimés ou autrement reproduits sans son autorisation.

In compliance with the Canadian Privacy Act some supporting forms may have been removed from this thesis.

Conformément à la loi canadienne sur la protection de la vie privée, quelques formulaires secondaires ont été enlevés de cette thèse.

While these forms may be included in the document page count, their removal does not represent any loss of content from the thesis.

Bien que ces formulaires aient inclus dans la pagination, il n'y aura aucun contenu manquant.


Canada

Abstract

Numerical Study of Primary Breakup of Liquid Sheets

Mohammad Movassat

The primary breakup of liquid sheets into ligaments has a great effect on the size, velocity, and penetration of the droplets produced further by the disintegration of ligaments. The generated ligaments can be categorized in two general types based on their orientation with respect to the flow field; span-wise and stream-wise ligaments. This work contains a two- and three-dimensional computational study of the primary breakup of a viscous liquid sheet. A Volume of Fluid (VOF) based code is used to solve the governing equations and capture the interface between the liquid sheet and the surrounding gas. Since the interaction between the liquid and gas is the major source of the breakup, the liquid-gas interface boundary is modified in this work and it is implemented using linear stability analysis.

The variation in the breakup time and breakup length of liquid sheets with fluid properties is investigated by a two-dimensional study. Fluid properties are stated in three non-dimensional numbers: Weber number, Ohnesorge number and the gas to liquid density ratio. The liquid surface tension shows a stabilizing effect by increasing both the breakup time and breakup length of liquid sheets. The liquid viscosity has more complicated effects; it increases the breakup length while at a certain range of Weber numbers, increasing the viscosity decreases the breakup time. Increasing the surrounding gas density decreases both breakup length and time. The study is extended to three-

dimension to capture the stream-wise ligaments as well as span-wise ligaments captured in two-dimension. The effect of fluid parameters on the formation of stream-wise ligaments is presented. A mesh refinement study is conducted which demonstrates that providing at least 7 computational cells per sheet thickness would lead to results which are not dependent on the mesh size.

Acknowledgments

I am deeply grateful for the support and guidance of Dr. Ali Dolatabadi . This thesis could not have been completed without his help, patience, and valuable advices. Also, I would like to acknowledge my friends Shahin Ghomeshi, Kasra Daneshkhah, Alborz Arzpeyma, Babak Samareh, Sanaz Arabzadeh, and Xiaoxia Hu. Finally, I would like to thank my parents for their moral support and patience.

Table of Contents

List of Figures.....	viii
List of Tables.....	x
1. Introduction.....	1
1.1. Overview.....	1
1.2. Previous works.....	4
1.2.1. Experimental Works	4
1.2.2. Theoretical/Numerical Studies.....	9
1.3. Numerical Methods in Two-phase Flows	15
1.3.1. Overview	15
1.3.2. Height Functions	16
1.3.3. Line Segments.....	17
1.3.4. Marker Methods.....	18
1.3.5. Volume of Fluid Methods	19
1.4. Objectives	25
1.5. Thesis Outline	26
2. Mathematical Formulation and Numerical Methodology.....	27
2.1. Mathematical Formulation.....	27
2.2. Numerical Model	29
2.2.1. Convection	32
2.2.2. Viscosity	35
2.2.3. Surface Tension	37
2.2.4. Pressure	38
2.2.5. Volume Fraction Advection.....	41
2.2.6. Time Step Restriction	44
2.3. Boundary Conditions	45
2.3.1. Domain Boundary Conditions	45
2.3.2. Interface Boundary Condition.....	47
3. Linear Stability Theory	50
3.1. Temporal Linear Stability Analysis	53
3.2. Spatial Linear Stability Analysis	58
4. Results.....	62
4.1. Two-Dimensional Results.....	62
4.1.1. Breakup Time.....	63
4.1.2. Breakup Length.....	71
4.2. Three-Dimensional Results.....	77
4.3. Effect of Initial Disturbance.....	89
.....	91

5. Closure	91
5.1. Conclusion	91
5.2. Future Work	93
Appendix A.....	100
Appendix B.....	104

List of Figures

Figure 1.1 Breakup of the liquid sheet.....	2
Figure 1.2 Two types of liquid streams, (a) liquid jet, (b) liquid sheet	3
Figure 1.3 Two types of instabilities, (a) anti-symmetric, (b) symmetric	4
Figure 1.4: Two types of ligaments, (a) span-wise, (b) stream-wise.....	6
Figure 1.5: Stretched stream-wise ligament breakup mechanism	9
Figure 1.6: Semi-infinite liquid sheets.....	13
Figure 1.7: Height Function.....	16
Figure 1.8: Line segments.....	17
Figure 1.9: Marker method	19
Figure 1.10: VOF method	20
Figure 1.11: Operator split method to advect the liquid	21
Figure 1.12: Two interface reconstruction method, (a) PLIC, (b) SLIC	24
Figure 2.1: Control volume used to compute the convection term, shaded control volume is the x-momentum control volume	33
Figure 2.2: Flux velocities defined at the faces of the momentum control volumes.....	34
Figure 2.3: The x-momentum control volume used to calculate viscous forces	36
Figure 2.4: Stencil used to solve the pressure equation.....	39
Figure 2.5: Interface representation at computational cells, PLIC method	42
Figure 2.6: Volume fraction advection	42
Figure 2.7: Flow chart of the analyses performed	46
Figure 2.8: Boundary conditions for temporal analysis.....	46
Figure 2.9: Boundary conditions for spatial analysis	47
Figure 2.10: Interface velocities, (a) external velocity, $w_{i,j,k+1/2}$, (b) tangential velocity, $u_{i+1/2,j,k}$	48
Figure 3.1: Disturbances traveling on the liquid sheet	50
Figure 3.2: Solution of inviscid dispersion equation for (a) $\rho_g/\rho_l=1/100$ (b) $We_g=0.5$	57
Figure 3.3: Inviscid solution of dispersion equation for spatial analysis for (a).....	61
$\rho_g/\rho_l=1/1000$ (b) $We_l=500$	61
Figure 4.1: Time evolution of the liquid sheet for $We_g=0.3$, $Oh=1$, and $\rho_g/\rho_l=1/1000$, (a) $t^*=0$, (b) $t^*=\tilde{t}/4$, (c) $t^*=3\tilde{t}/4$, (d) $t^*=\tilde{t}$	65
Figure 4.2: Time evolution of the liquid sheet for $We_g=0.3$, $Oh=1$, and $\rho_g/\rho_l=1/500$, (a) $t^*=0$, (b) $t^*=\tilde{t}/4$, (c) $t^*=3\tilde{t}/4$, (d) $t^*=\tilde{t}$	66
Figure 4.3: Time evolution of the liquid sheet for $We_g=0.5$, $Oh=1$, and $\rho_g/\rho_l=1/1000$, (a) $t^*=0$, (b) $t^*=\tilde{t}/4$, (c) $t^*=3\tilde{t}/4$, (d) $t^*=\tilde{t}$	67
Figure 4.4: Effect of We_g and ρ_g/ρ_l on the breakup time for $Oh=1$	68
Figure 4.5: Effect of the Ohnesorge number on the breakup time, (a) $\rho_g/\rho_l=1/500$, (b) $\rho_g/\rho_l=1/1000$	70
Figure 4.6: Breakup length	71
Figure 4.7: Spatial evolution of the liquid sheet with $\rho_g/\rho_l=1/1000$ and $Oh=1$ for various Weber numbers (a) $We_l=500$, (b) $We_l=400$, (c) $We_l=300$	73
Figure 4.8: Spatial evolution of the liquid sheet with $We_l=400$ and $Oh=1$ for various gas to liquid density ratios (a) $\rho_g/\rho_l=1/800$, (b) $\rho_g/\rho_l=1/1200$	74

Figure 4.9: The effect of Weber number on the breakup length for different gas to liquid density ratios for $Oh=1$	75
Figure 4.10: Variation of the breakup length with Ohnesorge number for $We_l=100$ and $\rho_g/\rho_l=1/1000$	76
Figure 4.11: 3D liquid sheet, (a) 3D view, (b) span-wise ligaments, (c) stream-wise ligaments	78
Figure 4.12: Stream-wise counter-rotating vorticities	79
Figure 4.13: Top view of the liquid sheet	80
Figure 4.14: Effect of gas to liquid density ratio on the stream-wise vorticity for $We_l=500$ and $Oh=1$, (a) $\rho_g/\rho_l=1/500$, (b) $\rho_g/\rho_l=1/700$, (c) $\rho_g/\rho_l=1/800$	81
Figure 4.15: The effect of Weber number on the x -vorticity for $\rho_g/\rho_l=1/700$ and $Oh=1$, (a) $We_l = 500$ (b) $We_l = 400$	82
Figure 4.16: The effect of Weber number on the x -vorticity for $\rho_g/\rho_l=1/1000$ and $Oh=1$ (a) $We_l = 500$, (b) $We_l = 400$	83
Figure 4.17: Effect of Ohnesorge number on the x -vorticity for $\rho_g/\rho_l=1/700$ and $We_l = 500$, (a) $Oh = 2$, (b) $Oh=3$	84
Figure 4.18: Effect of Ohnesorge number on the x -vorticity for $\rho_g/\rho_l=1/700$ and $We_l = 300$, (a) $Oh = 2$, (b) $Oh=3$	85
Figure 4.19: Variation of the breakup length with the mesh size	87
Figure 4.20: The effect of the mesh size on a 3D liquid sheet for $We_l = 500$, $Oh = 2$, $\rho_g/\rho_l = 1/1000$, (a) case 1, (b) case 2, (c) case 3.....	88
Figure 4.21: Span-wise locations used in Table 4.5	90
Figure 5.1: Velocity vectors for different span length, (a) three-wavelength, (b) four-wavelength, (c) five-wavelength.....	94
Figure 5.2: x -vorticity contour for different span lengths, (a) three-wavelength, (b) four-wavelength, (c) five-wavelength.....	95

List of Tables

Table 1.1: Review of VOF methods	23
Table 4.1: Exclusive dependency of the non-dimensional breakup time on the non-dimensional parameters for $\rho_g/\rho_l = 1/100$	64
Table 4.2: Exclusive dependency of the non-dimensional breakup length on the non-dimensional parameters for $\rho_g/\rho_l = 1/800$	72
Table 4.3: The effect of the mesh size on the breakup length for $We_l = 500$, $Oh = 2$, $\rho_g/\rho_l = 1/1000$	86
Table 4.4: Grid size used for the mesh study.....	87
Table 4.5: Effect of the initial disturbance on the non-dimensional breakup length.....	89

1. Introduction

1.1. Overview

Liquid sprays are used in many industrial processes. Among these processes are combustion in jet engines, internal combustion engines, icing phenomenon on the wings of aircrafts, heat exchangers, industrial washing and cleaning processes, ink-jet printers, coating, painting, and environmental protection. The diameter and velocity of the produced droplets from the spray are two most important characteristics of liquid sprays. These characteristics are greatly affected by the breakup of the initial liquid streams into ligaments and furthermore, by the disintegration of these ligaments into smaller droplets.

In most spray applications, liquid streams come out of an injector through a nozzle. There are many types of injectors which provide energy needed for the breakup of liquid streams into small droplets. Energy can be provided through various mechanisms such as liquid pressure, air pressure, rotation of cups or disks, vibration or acoustics, and electric fields [1]. The disintegration of liquid streams into small droplets can be divided into two main processes; primary and secondary breakup. Primary breakup, which is the subject of the present work, is defined as the disintegration of liquid streams into smaller ligaments. These ligaments may be formed in different orientations with respect to the direction in which the liquid stream flows. Further breakup of the generated ligaments into smaller droplets is called secondary breakup. The two mechanisms are shown in Figure 1.1. The primary breakup of liquid streams downstream of the nozzle exit can be caused by various phenomena. The most important of these are turbulence within the liquid and gas

phases, implosion of cavitation bubbles, and aerodynamic forces acting on the liquid stream.

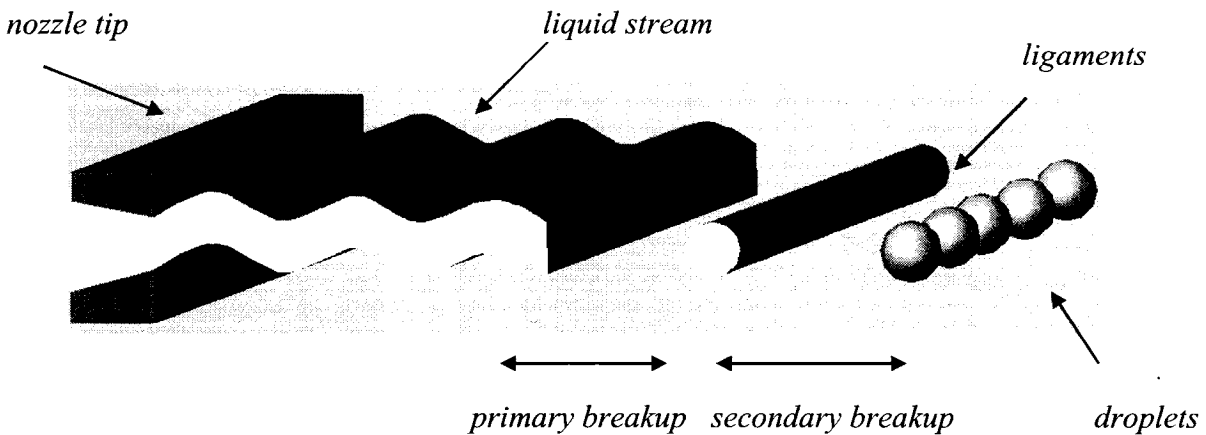


Figure 1.1 Breakup of the liquid sheet

Generally, the pressure drops along the spray nozzle results in liquid acceleration. Therefore, a high level of turbulence is generated within the liquid phase which has a destabilizing effect on the liquid once it exits the nozzle. Additionally, at sharp edges along the flow path inside the nozzle, the streamlines are contracted such that the effective cross-section of the flow is reduced and the flow is accelerated. According to Bernoulli's law this causes a reduction in the static pressure and local static pressure may be decreased to a value as low as the vapor pressure of the liquid. This phenomenon is called cavitation which may generate bubbles inside the nozzle [2]. These bubbles may be exploded downstream causing instabilities on the liquid stream.

Turbulence and cavitation effects, mentioned above, occur inside of the nozzle and generate disturbances on the surface of the liquid stream exiting the nozzle. Upon emerging from the nozzle, aerodynamic forces rising from the interaction between the

liquid and surrounding gas amplify the generated disturbances and cause the liquid stream to breakup. The growth of instabilities depends on the flow characteristics and shape of the liquid stream exiting the nozzle.

In most of the cases liquid stream emerging from a spray nozzle is in the form of a circular jet or sheet as shown in Figure 1.2. Primary breakup of liquid jets has been extensively investigated, [3], [4], and [5]. Concerning the primary breakup of liquid sheets, particular attention has been paid to the atomization of flat sheets because of their simplicity, extensive use, and additionally because they provide a convenient model for both experimental and theoretical studies. Present work studies the primary breakup of planar liquid sheets. A review of previous studies conducted on the primary breakup of liquid sheets follows. These studies can be divided into experimental and theoretical/numerical works.

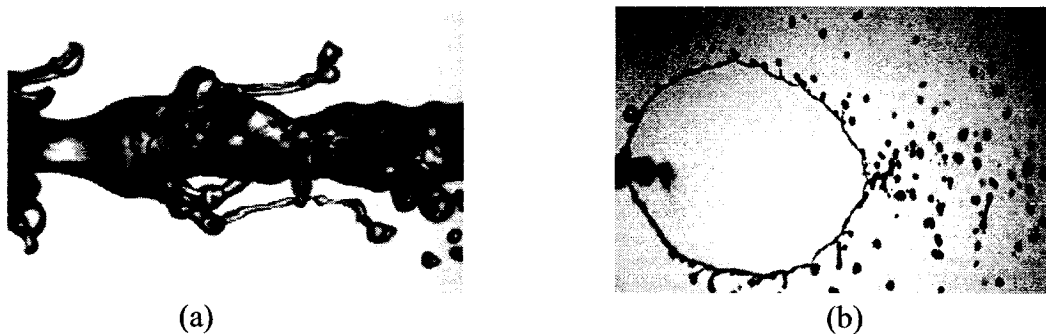


Figure 1.2 Two types of liquid streams, (a) liquid jet, (b) liquid sheet
(Photos from, (a) www.irphe.univ-mrs.fr, (b) www.mie.utoronto.ca/labs/MUSSL)

1.2. Previous works

1.2.1. Experimental Works

Initial studies on the disintegration of planar liquid sheets were conducted by Hagerty and Shea [6]. Their work included a theoretical and experimental investigation of inviscid liquid sheets moving in an inviscid gaseous medium. The experimental setup consisted of a slender orifice producing a flat sheet of liquid. The orifice was subjected to harmonic waves with different frequencies to produce a spectrum of instabilities on the liquid sheet. It was concluded that only two types of instabilities may grow on the surfaces of the liquid sheet. Either the two surfaces of the sheet oscillate in-phase to produce sinuous waves, i.e. anti-symmetric mode, or the two surfaces may oscillate out of phase to generate dilatational waves, i.e. symmetric mode. These two modes are shown in Figure 1.3 for a sheet with the undisturbed thickness of $2h$. Aerodynamic forces rising from interactions between the liquid sheet and surrounding gas were introduced as the main source of the breakup of the liquid sheet. Surface tension force was introduced as the main force counteracting the disintegration process. Since the liquid sheet and surrounding gas were assumed to be inviscid, viscous effects were not investigated.

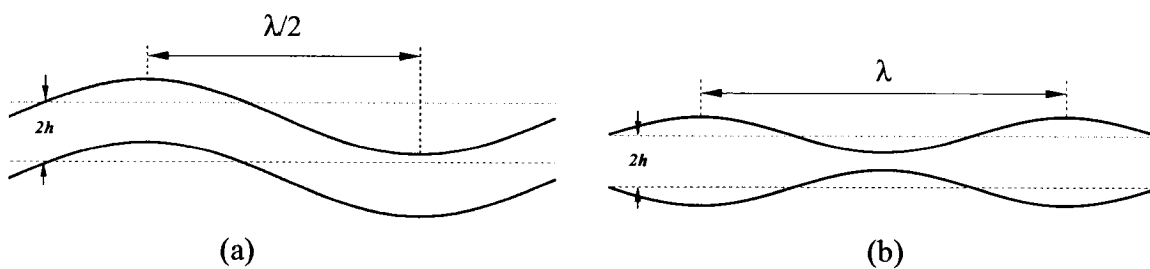


Figure 1.3 Two types of instabilities, (a) anti-symmetric, (b) symmetric

Dombrowski and Fraser [7] performed a photographic investigation on the disintegration of liquid sheets considering the effects of surface tension, viscosity and density on the stability of the liquid sheet. To study the effect of these parameters independently, a wide variety of liquids were used at a constant liquid-air relative velocity by adjusting the injection pressure to achieve the same flow rate. Results showed that surface tension has a stabilizing effect on the liquid sheet. Additionally it was noticed that with an increase in viscosity, the position of the disintegration of the sheet (i.e. breakup length) might move much further away from the nozzle exit. Results were presented using non-dimensional numbers including Weber number, which can be stated based on the gas or liquid density, Reynolds number, and gas to liquid density ratio.

$$We_l = \frac{\rho_l U^2 h}{\sigma}, \quad We_g = \frac{\rho_g U^2 h}{\sigma}, \quad Re = \frac{\rho_l U h}{\mu}, \quad \frac{\rho_g}{\rho_l} \quad (1.1)$$

where ρ_l , ρ_g , μ , and σ are liquid density, gas density, liquid viscosity and surface tension, respectively. U is the relative velocity between the liquid and gas and h is half of the sheet thickness.

Dombrowski and Fraser [7] studied the mechanisms of the formation of liquid ligaments from liquid sheets as well. They deduced that in the disintegration of liquid sheets the formation of ligaments is a necessary stage before the production of droplets. Two mechanisms for the formation of ligaments were identified; ligaments formed at the free edge of stable sheets and ligaments formed during the disruption of sheets. The latter, produces two types of ligaments, span-wise ligaments and stream-wise ligaments which

is dependent on the orientation of the formed ligaments as demonstrated in Figure 1.4 which shows the top view of a liquid sheet at two different flow conditions.

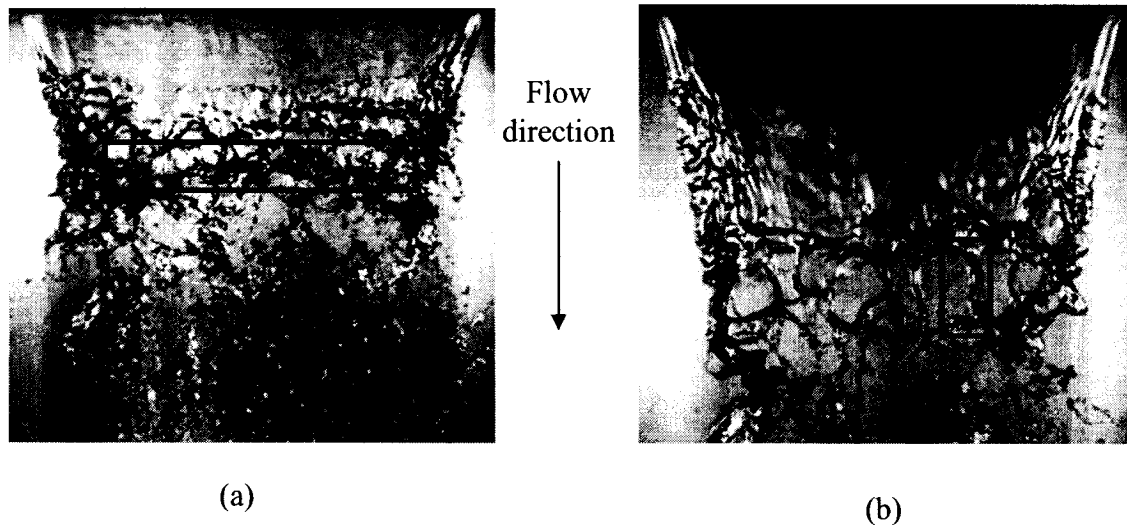


Figure 1.4: Two types of ligaments, (a) span-wise, (b) stream-wise
(Photos from Li et al. Physics of Fluids, 16, 2004)

Mansour and Chigier [8] conducted some experiments to study the aerodynamic instabilities formed on the surface of the liquid sheets emerging from a two dimensional nozzle. Detailed measurements of the frequency of the oscillation of the liquid sheets were made. Based on these results, three distinct modes for breakup of liquid sheets were found. At low liquid flow rates, the sinuous mode waves are dominant. At intermediate liquid flow rates both the sinuous and dilatational waves are superimposed on the surfaces of the liquid sheet. With a further increase in liquid flow rate, the liquid sheet oscillations mainly become of the dilatational type. It was also shown that the effect of introducing air into the nozzle is similar to the effect of inducing forced vibrations on the nozzle.

An experimental study on the liquid film disintegration regimes was done by Carvalho et al. [9] In their study, disintegration and breakup of liquid sheets into sprays were studied considering a flat liquid sheet surrounded by two air streams. Three different experimental techniques were used: back light and laser light sheet illumination to measure the amplitude of instabilities, strobe light illumination to quantify the breakup length and frequency of liquid sheets, and laser attenuation technique to measure the frequency and then compare with visualization technique. Three distinct breakup regimes were identified to be consistent with the results obtained by Mansour and Chigier [8]. They showed that at low liquid velocities (<1 m/s) sinuous waves are dominant while at high liquid velocities (> 3 m/s) dilatational waves dominate the breakup processes. At intermediate liquid velocities both sinuous and dilatational waves are observed to grow on the liquid sheet. Not only the effect of the relative velocity between the liquid and gas on the breakup of liquid sheets was studied, but also the variation in breakup lengths with absolute values of the liquid and gas velocities was considered. The effect of the gas injection angle on the breakup length was investigated as well. Although they considered some 3-D characteristics of liquid sheets such as the spray angle, their results are based on the formation of only span-wise ligaments.

Stapper et al. [10] conducted a thorough experimental study on the effect of liquid properties on the breakup length and breakup mechanisms of liquid sheets. Three liquids were selected that would demonstrate the differences in viscosity, surface tension, and density effects on the breakup mechanisms. The major source for the sheet breakup was identified to be the span-wise vorticities. These vorticities are generated as a result of the shear force rising from the relative velocity between the liquid and surrounding gas. The

span-wise vortical waves extend to the edges of the sheet and propagate in the stream-wise direction. Additionally, stream-wise waves are present at the nozzle tip and extend through the length of the sheet at fixed span-wise locations. These stream-wise waves are attributed to stream-wise vortices generated by background disturbances and amplified by the close coupling with the span-wise vortices. They identified two mechanisms of sheet breakup; cellular breakup and stretched stream-wise ligament breakup which are described below.

Cellular breakup regime occurs at high relative velocities between the liquid and gas. This mechanism is characterized by the presence of span-wise vortical waves that are approximately equal in strength to the stream-wise vortical waves. As the sheet is extruded by the shearing action of the air, the membranes stretch between the span-wise and stream-wise vortical waves, forming cell-like structures. The span-wise vortical waves separate into span-wise ligaments. The small droplets in the spray distribution originate from the bursting of membranes. Larger droplets are associated with the breakup of the span-wise ligaments.

Stretched stream-wise ligament breakup mechanism occurs at low relative velocities between the liquid and gas. This mechanism is dominated by the stream-wise vortical waves. As the sheet is stretched by the co-flowing air, the stream-wise vortices are amplified with thin liquid membranes stretched between. When the membranes burst, the liquid film forms small drops, while the vortical waves form stream-wise ligaments. Stream-wise ligaments and membranes formed between are shown in Figure 1.5 which is a more close view of Figure 1.4 (b).

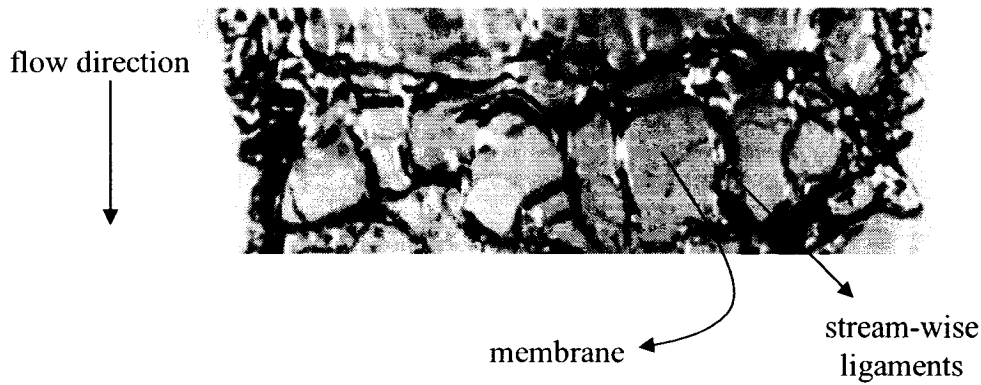


Figure 1.5: Stretched stream-wise ligament breakup mechanism

1.2.2. Theoretical/Numerical Studies

First theoretical studies on the breakup of liquid sheets were conducted by Dombrowski and John [11] assuming infinite sheets in the span-wise direction. The linear stability theory was applied on the liquid sheet. This theory assumes small disturbances with a spectrum of wavelengths, growth rates, and frequencies move on the surface of the liquid sheet. Linearized governing equations for the liquid are solved to find the relation between the wavelength and growth rate of the waves. Extensive description of the linear stability theory is explained in Chapter 3 of this work. Dombrowski and John [11] postulated that the size of the generated ligaments is related to the wavelength of the most unstable wave traveling on the surface of the liquid sheet. It was proposed that sinuous waves break into ligaments which are equal to half of the most unstable wavelength, while dilatational waves make ligaments which are equal to the full wavelength.

A temporal linear stability analysis was done by Xianguo et al. [12] considering a thin viscous liquid sheet moving in an inviscid gaseous medium. The effects of liquid and gas properties on the breakup time of liquid sheets were studied. It was shown that for small

gas to liquid density ratios, sinuous waves dominate the breakup of the sheet. For the first time, it was proposed that breakup of the liquid sheets might be categorized into two regimes; aerodynamic instability and viscosity-enhanced instability. For sinuous disturbances, viscosity amplifies instabilities at small Weber numbers for viscosity-enhanced regime, while liquid viscosity reduces the growth rate of instabilities at large Weber numbers for aerodynamic instability regime. At intermediate Weber numbers, liquid viscosity has complicated effects due to the interaction of the two regimes.

One year later, Li [13] extended the linear analysis from temporal to spatial to study the effect of liquid properties on the breakup length of liquid sheets. The study of the spatial evolution of liquid sheets is more descriptive as experimental observations show that breakup of liquid sheets does not occur at the nozzle exit but further downstream of the nozzle. It was shown that the gas to liquid density ratio has a great effect on the growth rate of instabilities traveling on the sheet. Considering spatial analysis, surface tension and liquid viscosity have a stabilizing effect on the breakup of the liquid sheet. The stabilizing effect of viscosity was in contrast to the results based on the temporal analysis.

Senecal et al. [14] applied the linear stability theory on liquid sheets to calculate the size and velocity of the droplets generated in pressure-swirl atomizers used in internal combustion engines. A temporal stability analysis was performed on the sheet to find breakup time. They considered both sinuous and dilatational instabilities and showed that sinuous waves are more unstable at small gas to liquid density ratios. They identified two regimes for the primary breakup of liquid sheets. It was shown that at relatively low Weber numbers, long waves dominate the breakup process but by increasing the Weber

number, the wavelength of the most dominant instability decreases. Gas based Weber number of 27/16 was introduced as the criterion between the long wave and short wave regimes. After finding the primary breakup time and length and the size of the generated ligaments, Rayleigh's theory [3] was applied to find the droplet size generated by further breakup of the ligaments. The calculated drop size distribution was used to model drop deformation and penetration in internal combustion engines using the KIVA [15] code. The results obtained were in an agreement with the experimental data.

Inoue [16] was the first who performed a 3D analytical and numerical study on the breakup of the liquid sheets using vortical mixing layers. In his work, the initial liquid sheet only contains span-wise vortices. Downstream of the nozzle, stream-wise vortices are generated due to the coupling with span-wise vortices. It was shown that just by subjecting the liquid sheet to small amplitude three-dimensional disturbances vortex filaments, which are initially in span-wise direction, would deform. This deformation would then cause the vortex lines to have both span-wise and stream-wise components. The stream-wise component would grow further and become as the same strength as the span-wise component. This component would make the sheet breakup in the stream-wise direction. However, as mentioned earlier, the initial amplitude and the location of the initial disturbance has a great effect on the primary breakup of liquid sheets.

The most thorough theoretical and numerical studies of planar liquid sheets have been conducted by Mehring et al. [17] and Kim et al. [18]. Mehring et al. [17] reviewed theories about distortion and disintegration of liquid streams as their work included both liquid jets and sheets. Two dimensional temporal analysis was accomplished to find the

breakup time of liquid sheets. The study composed of the linear and non-linear instability analyses. The results of the linear stability analysis were almost the same as the results of Senecal et al. [14]. It was shown that the results of the linear analysis are valid during the initial evolution of the disturbances. For a growing disturbance, the non-linear effects become dominant.

The basis for non-linear analysis is due to the presence of a non-zero vorticity component, span-wise vorticity, convected by the flow field according to Kelvin's theorem [19]. The liquid sheet is considered to be covered by a vortex sheet. The vortex sheet is discretized into a finite number of vortex panels, whose strength is not initially known. The vortex strength of each panel is found by considering that there is no mass flux normal to the surface of the liquid sheet. Two components of velocities on each computational panel are calculated based on the vortex strengths. Results based on this method demonstrate consistency with previous experimental data.

Both linear and non-linear analyses conducted by Mehring et al. [17] considered temporal analysis to find the breakup time of liquid sheets. Kim and Sirignano [18] published a review paper on 2D and 3D linear and nonlinear analyses of dilatational and sinuous waves on inviscid infinite and semi-infinite planar liquid sheets which cover most of the theoretical works done on the breakup of liquid sheets. The basis of the breakup of infinite sheets (temporal analysis) was described above. The stability analysis of semi-infinite sheets is further described.

A semi-infinite liquid sheet moving in the x -direction (infinite span is in the z direction) as shown in Figure 1.6 was studied. The liquid sheet is modulated at the nozzle exit ($x=0$) to make instabilities in both x and z directions with different wave numbers k and l , respectively. The wave number is defined as $2\pi/\lambda$ where λ is the wavelength. Applying linear stability analysis, the results of the 3D analysis with $l=0$ was identical to the 2-dimensional results of previous works. For $l \neq 0$, it was shown that the most unstable waves are the ones with the same wave numbers in the x and z directions (i.e. when $k=l$). For small amplitude disturbances, the results based on the linear stability theory were consistent with the results of the non-linear analysis. By increasing the amplitude of disturbances, non-linear effects would rise and thus the linear analysis is not valid anymore.

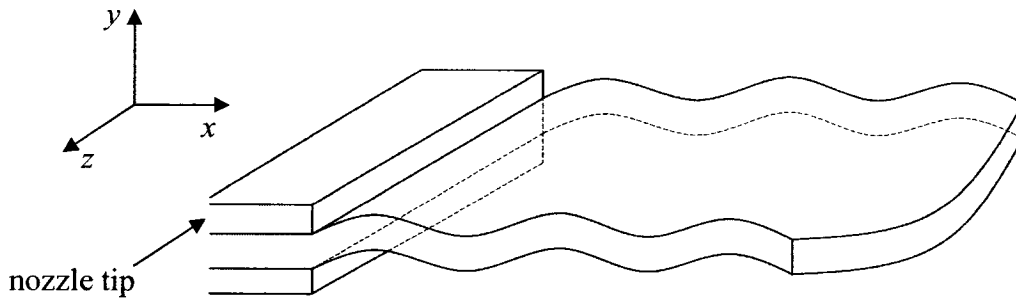


Figure 1.6: Semi-infinite liquid sheets

Non-linear results showed that most unstable waves are those with the same wave numbers in the x and z directions. Results demonstrated that while there is no velocity component in the z direction at the nozzle exit, this component is non-zero further downstream. The generated velocity in the z -direction makes stream-wise vorticities leading to the generation of stream-wise ligaments from the liquid sheet. This was concurrent to the theoretical results of Inoue [16]. Kim et al. [18] reported that for a specific range of Weber number, ligaments detached from the liquid sheet are both in

span-wise and stream-wise directions which is consistent with the cellular breakup regime proposed by Stapper et al [10].

Recently, Lin et al. [20] investigated three types of linear theories to study the stability of the liquid sheets; temporal analysis, spatial analysis, and spatial-temporal analysis. As mentioned in their work, the temporal theory is most commonly used because of its simplicity, while the spatial theory is used less but it is more descriptive due to considering that breakup occurs in the region downstream of the nozzle exit. Spatial-temporal analysis was introduced as the most complete linear theory to study the behavior of instabilities growing on liquid sheets. Some examples were demonstrated in which pure temporal or spatial analysis would lead to the damping of instabilities while disturbances would grow using spatial-temporal analysis.

Gaster [21] published a brief but very interesting note concerning the comparison of the results based on the temporal and spatial analyses. It was shown that the growth rate of disturbances in both analyses can be mathematically related. However it should be noted that one can not obtain the breakup length (calculated from spatial analysis) based on the breakup time (calculated from temporal analysis) and the absolute velocity of the liquid sheet. Only growth rates of two analyses can be related using the liquid sheet velocity.

Most of the theoretical and analytical works mentioned earlier were based on 2D and 3D linear and non-linear stability analyses of liquid sheets. Although these analyses consider precise boundary conditions at the interface of the liquid sheet and surrounding gas, higher order terms of governing equations are neglected. It is important to note that these

methods do not track the liquid-gas interface as physically there is a sharp discontinuity in the density of the materials at the interface. Several numerical methods have been developed to track or capture the interface between liquid and gas phases, especially when the interface has large distortions. These methods are summarized in the next section.

1.3. Numerical Methods in Two-phase Flows

1.3.1. Overview

The available methods to model two-phase flows can be divided into two classes; fixed grid (Eulerian), or moving grid (Lagrangian). In Eulerian methods, there is a predefined grid that does not move with the interface. In Lagrangian methods the interface is a boundary between two sub-domains of the grid. In both cases the grid may be structured or unstructured which facilitates the analysis near the interface.

The two methods differ in the manner in which the fluid elements are moved when their new velocities have been computed. In the Lagrangian case, the grid simply moves with the computed element velocities, while in an Eulerian calculation it is necessary to compute the flow of fluid through the mesh. This flow, or convective flux calculation, requires an averaging of the flow properties of all fluid elements that find themselves in a given mesh cell at a given time [22].

Convective averaging results in a smoothing of all variations in flow parameters, in particular, it results in the smearing of discontinuities such as free surfaces. The only way

to overcome this loss in resolution for free surfaces is to introduce some special treatment that recognizes a discontinuity and avoids any averaging across it [22]. Since the method applied in the present work is a fixed grid method, a brief review of the mostly used Eulerian methods follows.

1.3.2. Height Functions

A simple way to represent a free surface is to define its distance from a reference line as a function of position along the reference line. For example, in a 2D domain with a rectangular mesh of cells of width Δx and height Δy , one might define the vertical height, h , of the free surface above the bottom of the mesh in each column of cells. This would approximate a curve $h = f(x, t)$ by assigning values of h to discrete values of x as shown in Figure 1.7. This method does not work well when the slope of the boundary dh/dx , exceeds the mesh aspect ratio $\Delta y/\Delta x$ and does not work at all for multi-valued surfaces having more than one y value for a given x value. This is a severe limitation because many simple shapes, such as bubbles or drops can not be treated [22].

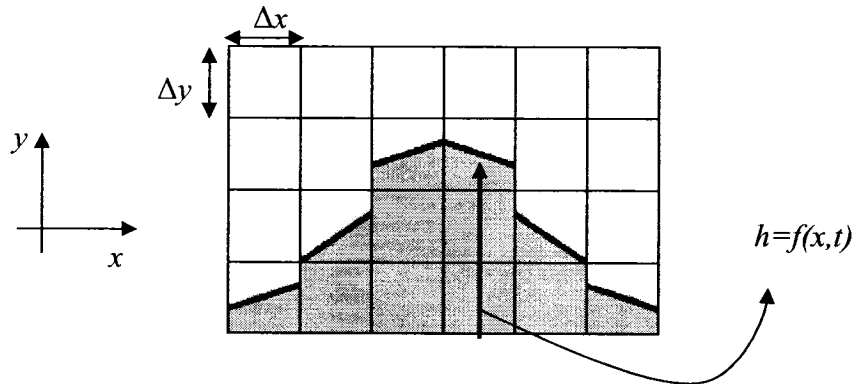


Figure 1.7: Height Function

The time evolution of the height function is governed by a kinematic equation expressing the fact that the surface must move with the liquid.

$$\frac{\partial h}{\partial t} + u \frac{\partial h}{\partial x} = v \quad (1.2)$$

where (u, v) are liquid velocity components in the (x, y) coordinate directions. The height function method is directly extendable to 3-dimensional problems for single-valued surfaces by $h = f(x, y, t)$.

1.3.3. Line Segments

A generalization of the height function method uses chains of short line segments at each computational cell. Coordinates for each point must be stored and for accuracy it is best to limit the distance between neighboring points to less than the minimum mesh size. Therefore, slightly more storage is required for this method, but it is not limited to single-valued surfaces. One example of line segments method is shown in Figure 1.8.

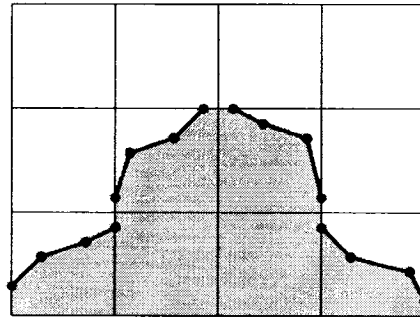


Figure 1.8: Line segments

The evolution of a chain of line segments is easily accomplished by moving each point with the local fluid velocity determined by interpolation in the surrounding cells. There is

one serious difficulty with the line segment method; when two surfaces intersect, segment chains must be reordered, possibly with the addition or removal of some chains [23]. In a general case, the detection of intersections and determining how a reordering should be done is not a trivial task. Also the extension of the line segment to three-dimensional surfaces is non-trivial. Linear ordering for two-dimensional lines does not work for three-dimensional surfaces.

1.3.4. Marker Methods

In marker methods, marker particles are used to identify phases. Interfacial or surfer marker methods use marker particles only on the interface. Volume marker methods have marker particles in the whole domain.

For two-phase flows, surfer markers are more accurate than volume markers because they track the exact location of the interface [24]. However where there are more than two phases, it may become difficult to handle the complexity of triple lines. Volume markers then afford a simple way of dealing with the problem. However an additional difficulty is that volume markers become distorted as time goes by and may need remeshing.

An illustration of the surfer marker method, in two particular cases, is shown in Figure 1.9. An advantage in using surface markers is that it allows forming very thin liquid bridges that do not break as shown in Figure 1.9 (a). However this is a real gain only in some cases. The situation may be made quite clear by considering the spiraling wave in Figure 1.9 (b). If both phases have the same viscosity and density and there is no surface tension, the interface is transparent to the fluid i.e. the fluid, in a way does not know that

there is an interface. The phases are only distinguished by their color. In that case it makes sense to track details smaller than the grid size [25].

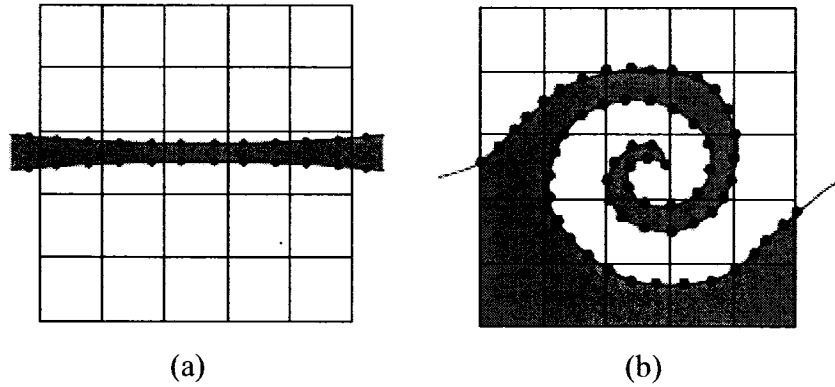


Figure 1.9: Marker method

Marker methods have other advantages including the high degree of accuracy that may be achieved by representing the interface through high-order interpolation polynomials. This accuracy may allow improving the accuracy of surface tension calculations. While the marker methods have the mentioned advantages, they suffer from a significant increase in required computer storage. They also require additional computational time to move all the points to new locations. Therefore it is natural to seek an alternative without excessive use of computer resources.

1.3.5. Volume of Fluid Methods

At each cell of the computational mesh, it is customary to use one value for each independent variable. The Volume of Fluid (VOF) method introduces a scalar field, f , called volume fraction whose value is unity at any point occupied by the fluid and zero

otherwise. The average value of f in a cell would then represent the fractional volume of the cell occupied by the fluid. In particular, a unit value of f would correspond to a cell full of fluid, while a zero value would indicate that the cell contains no fluid [22]. Cells with f values between zero and one must then contain a free surface. A schematic showing how the volume fractions are defined at computational cells is illustrated in Figure 1.10. Generally VOF algorithms consist of two main parts; reconstruction and propagation.

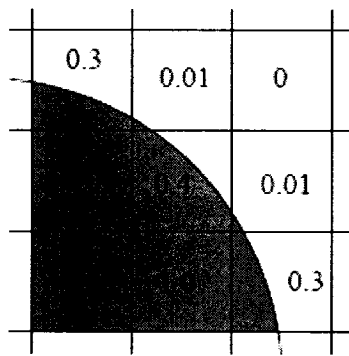


Figure 1.10: VOF method

The key part of the reconstruction step is the determination of the orientation of the interface. This is equivalent to resolve a unit normal vector in 2D or 3D. The normal direction to the interface lies in the direction in which the value of f changes most rapidly. After calculating the derivatives of f , these values can be used to determine the normal vector of the interface. By knowing the normal vector and the value of f at each cell, the line (in 2D) or surface (in 3D) representing the interface could be determined.

The second step of the VOF algorithm is propagation. Once the interface has been reconstructed, its motion by the underlying flow field must be modeled by a suitable advection algorithm. The volume fraction advection equation can be stated as:

$$\frac{\partial f}{\partial t} + u \frac{\partial f}{\partial x} + v \frac{\partial f}{\partial y} + w \frac{\partial f}{\partial z} = 0 \quad (1.3)$$

where u , v , and w are the velocities in the x , y , and z direction. Fractional step or operator-split methods will be described in which volume fraction, f , is advected each time along one spatial direction. Intermediate f values are calculated during this process, and the final f field is obtained only after advection of the interface along all coordinate directions.

One extensively used method to calculate fluxes along the x -direction is shown in Figure 1.11 where all of the liquid right to the bold solid line will cross the right boundary of the corresponding cell during time Δt . The liquid velocity in the x -direction is assumed to be u . For each cell, two contributions are calculated, the liquid fluxes entering the cell from its neighbors and the amount of liquid contained at the beginning of the step in the control volume which remains there.

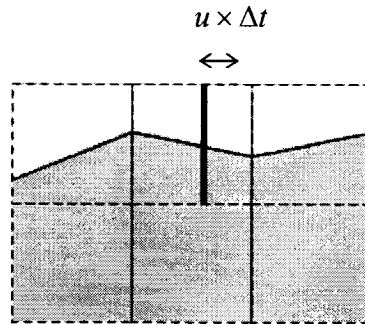


Figure 1.11: Operator split method to advect the liquid

VOF methods are more efficient compared to the other methods described above for several reasons [25]:

1. They preserve mass in a natural way, as a direct consequence of the development of an advection algorithm based on a discrete representation of the conservation law.
2. No special provision is necessary to perform reconnection or breakup of the interface and in this sense the change of topology is implicit in the algorithm.
3. They can be relatively simply extended from two dimensional to three dimensional domains.
4. The scheme is local in the sense that only the f values of the neighboring cells are needed to update the f value in each cell. For this reason, it is relatively simple to implement these algorithms in parallel, in particular within the framework of domain decomposition techniques.

However, in problems considering breakup, VOF methods suffer from being dependent on the mesh size since the breakup is captured based on the numerical errors. This dependency rises from the geometric nature of the steps including interface reconstruction and calculating the normal vectors [26].

Table 1.1 summarizes the notable volume tracking methods published since 1974. For each method important aspects of the interface reconstruction and volume advection algorithms are listed. Reconstruction features include piecewise constant and piecewise linear methods, as well the methodology used to calculate the normal vector of the

interface which can be either operator-split or multidimensional. Similarly, time integration of the volume advection equation can be done in an operator-split or multidimensional manner.

Table 1.1: Review of VOF methods

Author(s)	Reconstructed interface geometry	Time integration
DeBar (1974)	Piecewise linear, operator split	Operator split
Noh and Woodward (1976)	Piecewise constant, operator split	Operator split
Hirt and Nichols (1981)	Piecewise constant, multidimensional	Operator split
Chorin (1980)	Piecewise constant, multidimensional	Operator split
Barr and Ahurst (1984)	Piecewise constant, multidimensional	Operator split
Ashgriz and Poo (1991)	Piecewise linear, Operator split	Operator split
Youngs (1982)	Piecewise linear, multidimensional	Operator split
Pilliod and Puckett (1992)	Piecewise linear, multidimensional	Multidimensional

In the early 1970's, the first three volume tracking methods were introduced: Debar's method, Hirt and Nichols VOF method, and Noh and Woodward's SLIC method. Each of these methods had a different way to reconstruct the interface. The Debar's algorithm used a piecewise linear interface calculation (PLIC). In PLIC methods the interface is defined at each computational cell by a slope and an intercept. The slope of the interface

is calculated based on the volume fractions of neighboring cells. The SLIC method used a piecewise constant approximation in which the interfaces within each cell are aligned with one of the mesh coordinates. The VOF method also used a piecewise constant approximation in which interfaces are forced to align with mesh coordinates but are additionally allowed to be aligned with more than one mesh coordinate. The difference between the PLIC and SLIC methods can be investigated through Figure 1.12. In both cases, the real interface is shown by the thin solid line while the approximated interface is illustrated using bold solid line segments. As shown in Table 1.1, most volume tracking algorithms published to date fall into one of these three interface reconstruction categories. DeBar's piecewise PLIC choice for the reconstructed interface geometry is generally preferred in modern volume tracking algorithms. The reconstruction method used in the present work is that of Youngs' which lies in the piecewise linear category.

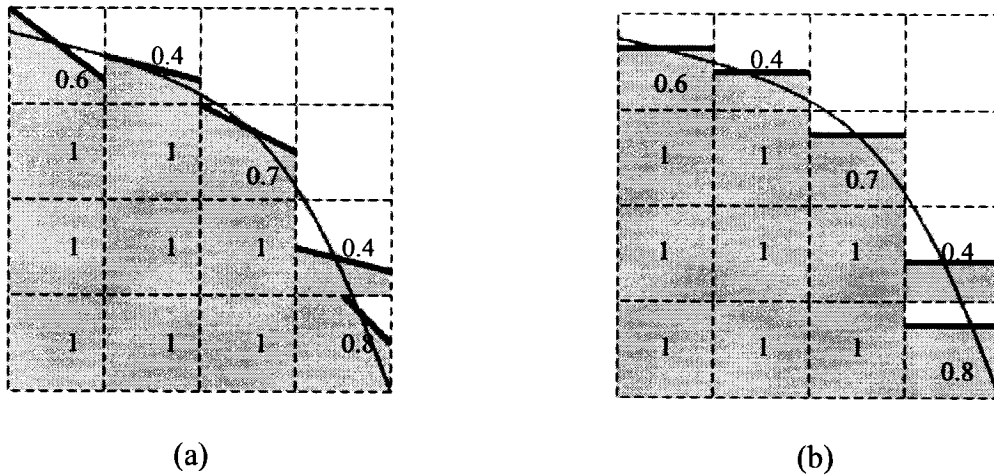


Figure 1.12: Two interface reconstruction method, (a) PLIC, (b) SLIC

1.4. Objectives

The objective of the present study is to model the primary breakup of planar liquid sheets. A numerical simulation of a thin liquid sheet is performed to study the effects of fluid properties, including liquid viscosity, surface tension and gas to liquid density ratio, on the breakup time and breakup length of liquid sheets. A Volume of Fluid (VOF) based code is used to solve governing equations and capture the interface between the liquid and gas. Piecewise linear algorithm of Youngs [27] is implemented to reconstruct the free surface. Since the major source of the primary breakup of liquid sheets is the aerodynamic interaction between two phases, the liquid-gas boundary needs special treatment to reduce the effect of mesh size on the breakup of liquid sheets associated with VOF methods. Linear stability theory is used to implement liquid-gas interface boundary. Depending on the type of simulation performed, temporal or spatial linear stability theory is applied. The objectives of this work can be stated as:

- Capture span-wise ligaments using 2D simulation.
- Study the effect of fluid properties on the breakup time of liquid sheets applying temporal linear stability analysis at liquid-gas interface.
- Study the effect of fluid properties on the breakup length of liquid sheets applying spatial linear stability analysis at liquid-gas interface.
- Extend the analysis to 3D to capture both span-wise and stream-wise ligaments.
- Study the effect of fluid properties on the formation of stream-wise ligaments.

1.5. Thesis Outline

Mathematical formulation, numerical model used to solve the governing equations, and applied boundary conditions are described in Chapter two. Modification of interface boundary condition using linear stability theory is explained in Chapter three. Results for two- and three-dimensional analyses are presented in Chapter four. Chapter five concludes the work and gives suggestions for the extension of this work.

2. Mathematical Formulation and Numerical Methodology

The computational code solves the governing equations for the liquid phase and introduces the effect of the surrounding gas at the liquid-gas interface boundary. The equations governing the flow field are mass and momentum conservation as well as volume fraction advection equations. Mathematical formulation of these equations is presented following by the description of the numerical scheme used to discretize equations and applied boundary conditions. It would be helpful to note that equations are generally explained in 3D, but for clarity the figures are illustrated in 2D.

2.1. Mathematical Formulation

Mass and momentum conservation equations can be stated as:

$$\nabla \cdot \vec{V} = 0 \quad (2.1)$$

$$\frac{\partial \vec{V}}{\partial t} + \nabla \cdot (\vec{V}\vec{V}) = -\frac{1}{\rho} \nabla p + \frac{1}{\rho} \nabla \cdot \tau + \vec{g} + \frac{1}{\rho} \vec{F}_b \quad (2.2)$$

where \vec{V} represents velocity vector, p the pressure, ρ the fluid density, τ the shear stress tensor, \vec{g} gravitational acceleration, and \vec{F}_b is the total body force (per unit volume) acting on the fluid. The fluid is assumed to be Newtonian, therefore the shear stress tensor can be written as:

$$\tau = \mu \left(\nabla \vec{V} + (\nabla \vec{V})^T \right) \quad (2.3)$$

where μ is the dynamic viscosity of the fluid. The most important body force considered in this work is the surface tension force. This force is applied by implementing the

Continuum Surface Force (CSF) model proposed by Brackbill et al. [28]. In the CSF model surface tension force is calculated as:

$$\vec{F}_{ST}(\vec{x}) = \sigma \int_S \kappa(\vec{y}) \hat{n}(\vec{y}) \delta(\vec{x} - \vec{y}) dS \quad (2.4)$$

where σ is the liquid surface tension at the interface, κ is the local curvature, \hat{n} is the local unit normal to the interface, and δ is the Dirac delta function. In equation (2.4), S corresponds to the area of the free surface. \vec{x} and \vec{y} are vectors indicating the location in which the force is calculated and the location of free surface, respectively. Curvature is defined as:

$$\kappa = -\nabla \cdot \hat{n} \quad (2.5)$$

Calculating \hat{n} requires a method to represent the interface between the two phases (liquid and gas). As mentioned in the first chapter, a VOF method based on a piecewise linear reconstruction of the interface is used to capture the interface between two fluids. VOF methods assume a scalar field, f , called volume fraction which is defined as:

$$\begin{cases} f = 0 & \text{no liquid phase} \\ 0 < f < 1 & \text{interface} \\ f = 1 & \text{within liquid phase} \end{cases}$$

Since the volume fraction represents the volume occupied by the liquid, it should be advected by the flow field. The equation which governs volume fraction advection is:

$$\frac{\partial f}{\partial t} + (\vec{V} \cdot \nabla) f = 0 \quad (2.6)$$

Following the advection, the interface is reconstructed by the piecewise linear method proposed by Youngs [27]. The normal vector to the interface is calculated using the gradient of the f field as:

$$\hat{n} = \frac{\nabla f}{|\nabla f|} \quad (2.7)$$

This vector is applied to find the local curvature from equation (2.5), and finally calculate the surface tension force using equation (2.4).

2.2. Numerical Model

The numerical model is based on RIPPLE [29] code. RIPPLE is a two-dimensional Eulerian fixed-grid code developed for free surface flows. The development of RIPPLE to 3D was done by Bussmann et al [30].

Equations (2.1), (2.2), and (2.6) are discretized on a Cartesian mesh. As originally described in the marker and cell (MAC) method [31], velocities are specified at the cell faces and pressure at each cell center. The scalar f is discretized by integrating over a cell volume, $\Omega_{i,j,k}$, to obtain the volume fraction $f_{i,j,k}$.

$$f_{i,j,k} = \frac{1}{\Omega_{i,j,k}} \int_{\Omega_{i,j,k}} f d\Omega \quad (2.8)$$

Cells filled with the liquid are characterized by $f_{i,j,k} = 1$, empty cells by $f_{i,j,k} = 0$, and cells which contain a portion of the interface by $0 < f_{i,j,k} < 1$. While the pressure $p_{i,j,k}$ represents the value of pressure at the center of cell (i, j, k) , the volume fraction $f_{i,j,k}$ is an integral quantity associated only with the volume of cell (i, j, k) . It would be inappropriate to interpret $f_{i,j,k}$ as the value of f at the center of the cell (i, j, k) .

Equations (2.1) and (2.2) are solved using a two-step projection method in which the forward time discretization includes two sub-steps. First, an intermediate velocity, \vec{V}' , is computed explicitly from convective, viscous, gravitational and body force accelerations based on the known velocity, \vec{V}^n , for a time step Δt .

$$\frac{\vec{V}' - \vec{V}^n}{\Delta t} = -\nabla \cdot (\vec{V}\vec{V})^n + \frac{1}{\rho} \nabla \cdot \tau^n + \vec{g}^n + \frac{1}{\rho} \vec{F}_b^n \quad (2.9)$$

The next step is to project \vec{V}' into a divergence free velocity field. Basically this projection states that the new velocity field \vec{V}^{n+1} should include the effect of the pressure force and satisfy continuity equation which are stated mathematically in equations (2.10) and (2.11), respectively.

$$\frac{\vec{V}^{n+1} - \vec{V}'}{\Delta t} = -\frac{1}{\rho^n} \nabla p^{n+1} \quad (2.10)$$

$$\nabla \cdot (\vec{V}^{n+1}) = 0 \quad (2.11)$$

Substituting equation (2.10) into equation (2.11), after rearrangement, would result in equation (2.12) in which the pressure at time step $n+1$ is unknown and should be calculated implicitly based on the known intermediate velocity.

$$\nabla \cdot \left(\frac{1}{\rho^n} \nabla p^{n+1} \right) = \frac{1}{\Delta t} \nabla \cdot \vec{V}' \quad (2.12)$$

Note that the summation of equations (2.9) and (2.10) yields to the complete momentum conservation equation.

The right hand side (RHS) of equation (2.9) is discretized according to the conventions typical of the finite volume methods [32]. Integrating equation (2.9) over a control volume $\Omega_{i,j,k}$:

$$\frac{1}{\Delta t} \int_{\Omega_{i,j,k}} (\vec{V}' - \vec{V}^n) d\Omega = - \int_{\Omega_{i,j,k}} \nabla \cdot (\vec{V} \vec{V})^n d\Omega + \frac{1}{\rho} \int_{\Omega_{i,j,k}} \nabla \cdot \tau^n d\Omega + \int_{\Omega_{i,j,k}} \vec{g}^n d\Omega + \frac{1}{\rho} \int_{\Omega_{i,j,k}} \vec{F}_b^n d\Omega \quad (2.13)$$

Applying Gauss' theorem to convert the first two volume integrals on the RHS of equation (2.13) over the control surface $S_{i,j,k}$ and assuming that other integrands are constant within the volume $\Omega_{i,j,k}$, equation (2.13) yields to:

$$\frac{\vec{V}' - \vec{V}^n}{\Delta t} = - \frac{1}{\Omega_{i,j,k}} \int_{S_{i,j,k}} \vec{V}^n (\vec{V}^n \cdot \hat{n}_s) dS + \frac{1}{\rho \Omega_{i,j,k}} \int_{S_{i,j,k}} (\tau^n \cdot \hat{n}_s) dS + \vec{g}_n + \frac{1}{\rho} \vec{F}_b^n \quad (2.14)$$

\hat{n}_s is the unit normal vector of the surface $S_{i,j,k}$ facing outside of the volume $\Omega_{i,j,k}$.

Discretization of each of the terms in equation (2.14) would follow. In summary, the algorithm which advances the solution in time includes:

- compute \vec{V}' explicitly.
- solve the equation (2.12) to find p^{n+1} implicitly.
- compute \vec{V}^{n+1} from equation (2.10) and apply boundary conditions on \vec{V}^{n+1}
- compute the new volume fraction distribution f^{n+1} using equation (2.6)
- reconstruct the interface using equations (2.5) and (2.7).

2.2.1. Convection

Consider discretization of the x -component of the convective term in equation (2.14). A 2D control volume used to discretize this term, the x -momentum control volume, is shown in Figure 2.1. The convection term in equation (2.14) can be stated as:

$$\begin{aligned}
 -\frac{1}{\Omega_{i+\frac{1}{2},j,k}} \int_{S_{i+\frac{1}{2},j,k}} u(\vec{V} \cdot \hat{n}_s) dS = & -\frac{u_{i+1,j,k}^{fl} \langle u \rangle_{i+1,j,k} - u_{i,j,k}^{fl} \langle u \rangle_{i,j,k}}{\Delta x_{i+\frac{1}{2}}} - \\
 & \frac{v_{i+\frac{1}{2},j+\frac{1}{2},k}^{fl} \langle u \rangle_{i+\frac{1}{2},j+\frac{1}{2},k} - v_{i+\frac{1}{2},j-\frac{1}{2},k}^{fl} \langle u \rangle_{i+\frac{1}{2},j-\frac{1}{2},k}}{\Delta y_j} \\
 & \frac{w_{i+\frac{1}{2},j,k+\frac{1}{2}}^{fl} \langle u \rangle_{i+\frac{1}{2},j,k+\frac{1}{2}} - w_{i+\frac{1}{2},j,k-\frac{1}{2}}^{fl} \langle u \rangle_{i+\frac{1}{2},j,k-\frac{1}{2}}}{\Delta z_k}
 \end{aligned} \tag{2.15}$$

The flux velocities u^{fl} , v^{fl} and w^{fl} represent the rates of transport of the quantity $\langle u \rangle$ in or out of the control volume of Figure 2.1. Flux velocities are defined at the faces of momentum control volumes and are basically calculated by the interpolation of the surface velocities of the computational mesh. These velocities are shown in Figure 2.2 and are calculated as below.

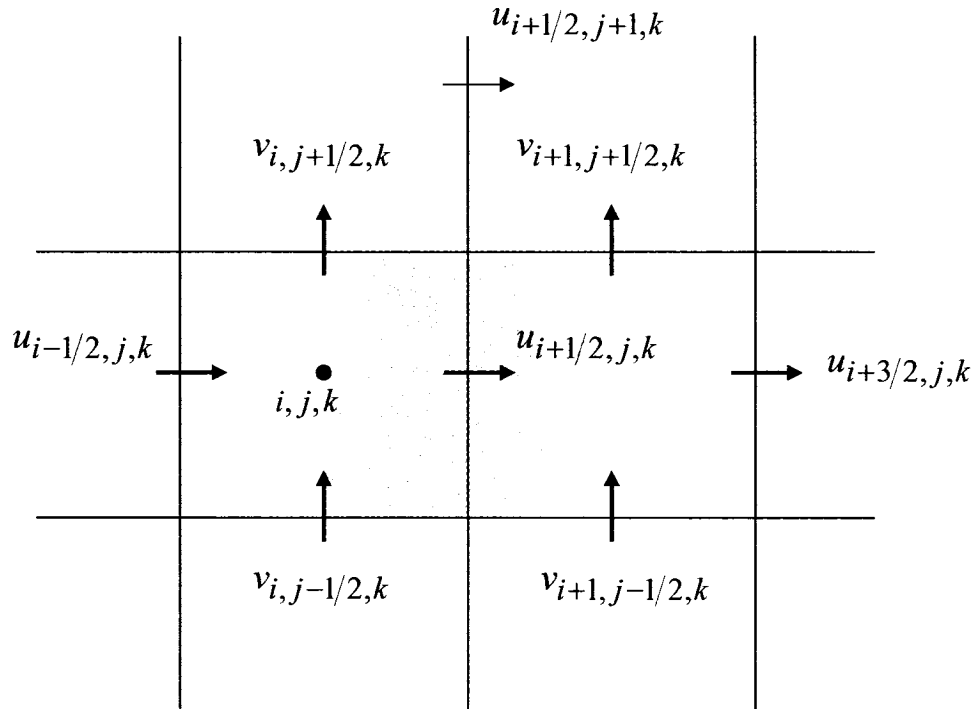


Figure 2.1: Control volume used to compute the convection term, shaded control volume is the x-momentum control volume

$$\begin{aligned}
 u_{i,j,k}^n &= \frac{u_{i-\frac{1}{2},j,k} + u_{i+\frac{1}{2},j,k}}{2} \\
 u_{i+1,j,k}^n &= \frac{u_{i+\frac{1}{2},j,k} + u_{i+\frac{3}{2},j,k}}{2} \\
 v_{i+\frac{1}{2},j-\frac{1}{2},k}^n &= \frac{\Delta x_{i+1} v_{i,j-\frac{1}{2},k} + \Delta x_i v_{i+1,j-\frac{1}{2},k}}{\Delta x_i + \Delta x_{i+1}} \\
 v_{i+\frac{1}{2},j+\frac{1}{2},k}^n &= \frac{\Delta x_{i+1} v_{i,j+\frac{1}{2},k} + \Delta x_i v_{i+1,j+\frac{1}{2},k}}{\Delta x_i + \Delta x_{i+1}} \\
 w_{i+\frac{1}{2},j,k-\frac{1}{2}}^n &= \frac{\Delta x_{i+1} w_{i,j,k-\frac{1}{2}} + \Delta x_i w_{i+1,j,k-\frac{1}{2}}}{\Delta x_i + \Delta x_{i+1}} \\
 w_{i+\frac{1}{2},j,k+\frac{1}{2}}^n &= \frac{\Delta x_{i+1} w_{i,j,k+\frac{1}{2}} + \Delta x_i w_{i+1,j,k+\frac{1}{2}}}{\Delta x_i + \Delta x_{i+1}}
 \end{aligned} \tag{2.16}$$

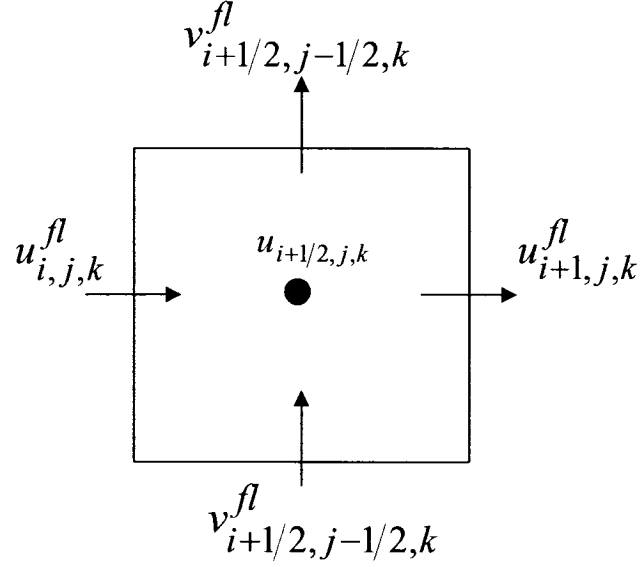


Figure 2.2: Flux velocities defined at the faces of the momentum control volumes

For two neighbor cells filled with the liquid, the flux quantity $\langle u \rangle$ is approximated by the method of Van Leer [33]. As an example, $\langle u \rangle_{i,j,k}$ at the left face of control volume showed in Figure 2.2 can be stated as:

$$\langle u \rangle_{i,j,k} = \begin{cases} u_{i-\frac{1}{2},j,k} + \frac{\Delta x_i}{2} \alpha^{vl} \left(\frac{\partial u}{\partial x} \right)_{i-\frac{1}{2},j,k} \left[1 - \frac{u_{i,j,k}^{fl} \Delta t}{\Delta x_i} \right] & u_{i,j,k}^{fl} > 0 \\ u_{i+\frac{1}{2},j,k} - \frac{\Delta x_i}{2} \alpha^{vl} \left(\frac{\partial u}{\partial x} \right)_{i+\frac{1}{2},j,k} \left[1 + \frac{u_{i,j,k}^{fl} \Delta t}{\Delta x_i} \right] & u_{i,j,k}^{fl} < 0 \end{cases} \quad (2.17)$$

where the velocity gradients are approximated as:

$$\begin{aligned}
\left(\frac{\partial u}{\partial x}\right)_{i-\frac{1}{2},j,k} &= \frac{u_{i+\frac{1}{2},j,k} - u_{i-\frac{3}{2},j,k}}{\Delta x_{i-1} + \Delta x_i} \\
\left(\frac{\partial u}{\partial x}\right)_{i+\frac{1}{2},j,k} &= \frac{u_{i+\frac{3}{2},j,k} - u_{i-\frac{1}{2},j,k}}{\Delta x_i + \Delta x_{i+1}}
\end{aligned} \tag{2.18}$$

Equation (2.17) corresponds to the first order upwind approximation when $\alpha^{vL} = 0$ and to a conditionally unstable second order central difference when $\alpha^{vL} = 1$. Details of calculating α^{vL} can be found in the work of Bussmann [34]. Due to complications, for control volumes at the interface, strict upwind scheme is applied ($\alpha^{vL} = 0$).

2.2.2. Viscosity

The viscous term in the equation (2.14) can be expanded as:

$$\nabla \cdot \tau = \left(\frac{\partial \tau_{xx}}{\partial x} + \frac{\partial \tau_{yx}}{\partial y} + \frac{\partial \tau_{zx}}{\partial z} \right) \hat{i} + \left(\frac{\partial \tau_{xy}}{\partial x} + \frac{\partial \tau_{yy}}{\partial y} + \frac{\partial \tau_{zy}}{\partial z} \right) \hat{j} + \left(\frac{\partial \tau_{xz}}{\partial x} + \frac{\partial \tau_{yz}}{\partial y} + \frac{\partial \tau_{zz}}{\partial z} \right) \hat{k} \tag{2.19}$$

Similar to the convection part, only the x-component of the viscous term is explained. Expansion to the y- and z-components is straightforward. The x-momentum control volume used to discretize the viscous term is shown in Figure 2.3.

$$\left(\frac{\partial \tau_{xx}}{\partial x} + \frac{\partial \tau_{yx}}{\partial y} + \frac{\partial \tau_{zx}}{\partial z} \right)_{i+\frac{1}{2},j,k} = \frac{\tau_{xx,i+1,j,k} - \tau_{xx,i,j,k}}{\Delta x_{i+\frac{1}{2}}} + \frac{\tau_{yx,i+\frac{1}{2},j+\frac{1}{2},k} - \tau_{yx,i+\frac{1}{2},j-\frac{1}{2},k}}{\Delta y_j} + \frac{\tau_{zx,i+\frac{1}{2},j,k+\frac{1}{2}} - \tau_{zx,i+\frac{1}{2},j,k-\frac{1}{2}}}{\Delta y_k} \tag{2.20}$$

Each component of the above equation is evaluated based on the neighboring velocities.

Expansion of each term in equation (2.20) can be stated as:

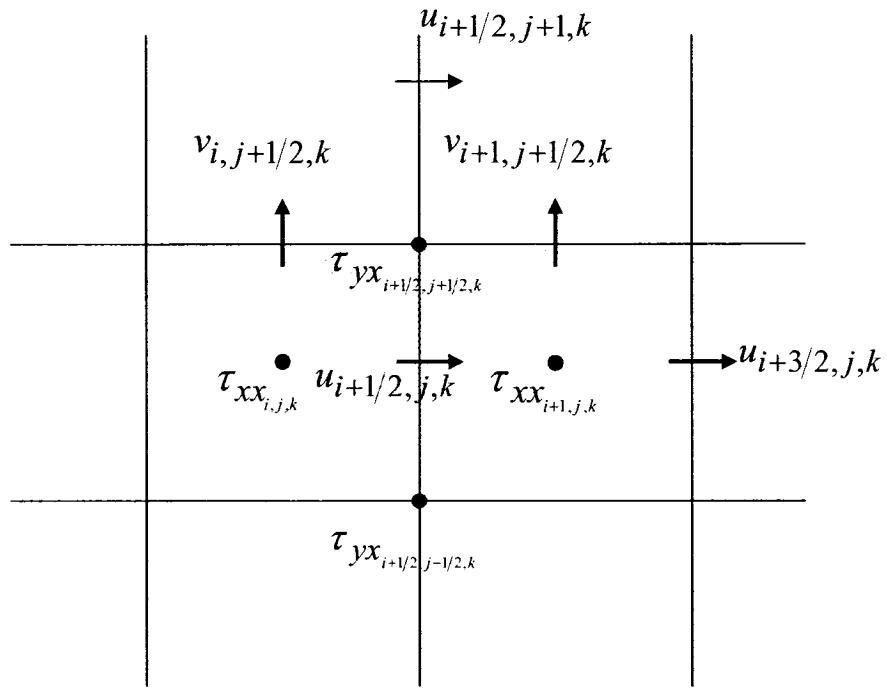


Figure 2.3: The x-momentum control volume used to calculate viscous forces

$$\begin{aligned}
\tau_{xx_{i+1,j,k}} &= 2\mu \frac{u_{i+\frac{3}{2},j,k} - u_{i+\frac{1}{2},j,k}}{\Delta x_{i+1}} \\
\tau_{xx_{i,j,k}} &= 2\mu \frac{u_{i+\frac{1}{2},j,k} - u_{i-\frac{1}{2},j,k}}{\Delta x_i} \\
\tau_{yx_{i+\frac{1}{2},j+\frac{1}{2},k}} &= \mu \left(\frac{u_{i+\frac{1}{2},j+1,k} - u_{i+\frac{1}{2},j,k}}{\Delta y_{j+\frac{1}{2}}} + \frac{v_{i+1,j+\frac{1}{2},k} - v_{i,j+\frac{1}{2},k}}{\Delta x_{i+\frac{1}{2}}} \right) \\
\tau_{yx_{i+\frac{1}{2},j-\frac{1}{2},k}} &= \mu \left(\frac{u_{i+\frac{1}{2},j,k} - u_{i+\frac{1}{2},j-1,k}}{\Delta y_{j-\frac{1}{2}}} + \frac{v_{i+1,j-\frac{1}{2},k} - v_{i,j-\frac{1}{2},k}}{\Delta x_{i+\frac{1}{2}}} \right) \\
\tau_{zx_{i+\frac{1}{2},j,k+\frac{1}{2}}} &= \mu \left(\frac{u_{i+\frac{1}{2},j,k+1} - u_{i+\frac{1}{2},j,k}}{\Delta z_{k+\frac{1}{2}}} + \frac{w_{i+1,j,k+\frac{1}{2}} - w_{i,j,k+\frac{1}{2}}}{\Delta x_{i+\frac{1}{2}}} \right) \\
\tau_{zx_{i+\frac{1}{2},j,k-\frac{1}{2}}} &= \mu \left(\frac{u_{i+\frac{1}{2},j,k} - u_{i+\frac{1}{2},j,k-1}}{\Delta z_{k-\frac{1}{2}}} + \frac{w_{i+1,j,k-\frac{1}{2}} - w_{i,j,k-\frac{1}{2}}}{\Delta x_{i+\frac{1}{2}}} \right)
\end{aligned} \tag{2.21}$$

where μ is the dynamic viscosity of the liquid phase.

2.2.3. Surface Tension

The method applied to implement the surface tension force is based on the Continuum Surface Force model proposed by Brackbill et al. [28]. This force is implemented using equation (2.4). Since the δ function in Equation (2.4) is infinity at the interface and zero elsewhere, discretization of this term requires more consideration. Finite approximation of δ assumes that the surface tension force is applied at the vicinity of the interface including couple of computational cells. By this method, δ and hence the surface tension

force are smoothed. Another issue to calculate surface tension force is evaluation of the normal vector, $\hat{n}_{i,j,k}$, in equation (2.4).

As described by Bussmann [34], $\hat{n}_{i,j,k}$ is calculated by evaluating the gradient of smoothed $f_{i,j,k}$. The same δ function used to smooth surface tension force is applied to smooth $f_{i,j,k}$ values. The complete formulation of δ can be found at [34]. As an example, smoothed values of volume fraction at the cell (i,j) , $\bar{f}_{i,j}$, can be stated as:

$$\bar{f}_{i,j} = 0.396f_{i,j} + 0.1229(f_{i+1,j} + f_{i-1,j} + f_{i,j+1} + f_{i,j-1}) + 0.0281(f_{i+1,j+1} + f_{i-1,j+1} + f_{i+1,j-1} + f_{i-1,j-1}) \quad (2.22)$$

where the coefficients come from the definition of the finite δ function.

2.2.4. Pressure

At this stage, the explicit change in the velocity field due to convection, viscous forces, and the surface tension force, has been made and the intermediate velocity, \vec{V}' , has been calculated. Solving the equation (2.12) implicitly follows. Discretization of equation (2.12) at a computational cell yields to a set of equations including all of the neighboring cells. A 2D schematic of this stencil is shown in Figure 2.4.

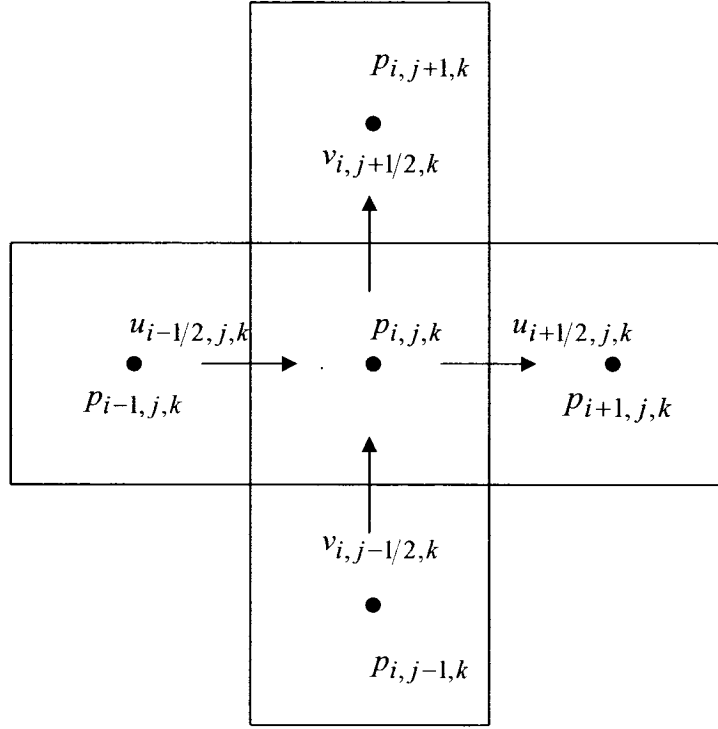


Figure 2.4: Stencil used to solve the pressure equation

A straightforward discretization of equation (2.12) will give:

$$a_{i,j,k} p_{i,j,k} + \sum_{nb} a_{nb} p_{nb} = b_{i,j,k} \quad (2.23)$$

where the index nb includes each of the six neighboring cells. The coefficients are defined as:

$$\begin{aligned}
a_{i+1,j,k} &= \frac{1}{\rho_{i+\frac{1}{2},j,k} \Delta x_{i+\frac{1}{2}}} \\
a_{i,j+1,k} &= \frac{1}{\rho_{i,j+\frac{1}{2},k} \Delta y_{j+\frac{1}{2}}} \\
a_{i,j,k+1} &= \frac{1}{\rho_{i,j,k+\frac{1}{2}} \Delta z_{k+\frac{1}{2}}} \\
a_{i-1,j,k} &= \frac{1}{\rho_{i-\frac{1}{2},j,k} \Delta x_{i-\frac{1}{2}}} \\
a_{i,j-1,k} &= \frac{1}{\rho_{i,j-\frac{1}{2},k} \Delta y_{j-\frac{1}{2}}} \\
a_{i,j,k-1} &= \frac{1}{\rho_{i,j,k-\frac{1}{2}} \Delta z_{k-\frac{1}{2}}} \\
a_{i,j,k} &= -(a_{i+1,j,k} + a_{i,j+1,k} + a_{i,j,k+1} + a_{i-1,j,k} + a_{i,j-1,k} + a_{i,j,k-1}) \\
b_{i,j,k} &= \frac{D_{i,j,k}}{\Delta t}
\end{aligned} \tag{2.24}$$

where densities at cell faces are calculated as the average density of two neighbor cells and $D_{i,j,k}$ is the non-zero divergence of the intermediate velocity calculated as:

$$D_{i,j,k} = \left(\frac{u'_{i+\frac{1}{2},j,k} - u'_{i-\frac{1}{2},j,k}}{\Delta x_i} + \frac{v'_{i,j+\frac{1}{2},k} - v'_{i,j-\frac{1}{2},k}}{\Delta y_j} + \frac{w'_{i,j,k+\frac{1}{2}} - w'_{i,j,k-\frac{1}{2}}}{\Delta z_k} \right) \tag{2.25}$$

Equation (2.23) along with coefficients stated in equations (2.24) and (2.25) yields to a set of equations represented by a positive definite matrix. This set of equations is solved at each time step using an Incomplete Cholesky Conjugate Gradient solver [35]. Appropriate boundary conditions are applied at the domain boundaries depending on the specific problem.

The next step for calculating the new velocity field is to update the calculated intermediate velocity field by including the effect of the pressure term. As an example for the x -momentum control volume shown in Figure 2.1:

$$u_{i+\frac{1}{2},j,k}^{n+1} = u'_{i+\frac{1}{2},j,k} - \frac{\Delta t}{\rho_{i+\frac{1}{2},j,k}^n} \frac{p_{i+1,j,k}^{n+1} - p_{i,j,k}^{n+1}}{\Delta x_{i+\frac{1}{2}}} \quad (2.26)$$

The final process at each time step is to advect the volume fraction based on the new calculated velocity field.

2.2.5. Volume Fraction Advection

As described in chapter one, volume fraction advection in VOF methods consists of two parts, interface reconstruction and the evaluation of fluxes of the liquid across the cell faces. As mentioned before, Youngs' [27] method is applied which uses a piecewise linear interface calculation (PLIC).

In Youngs' method, the interface is represented by a plane within each interface cell knowing the volume fraction, $f_{i,j,k}$, and the normal vector, $\hat{n}_{i,j,k}$. In 2D, the interface is simply a line crossing the cell. Figure 2.5 shows the volume fraction at each computational cell in a 2D problem. The real interface is shown by a thin solid line. The position of the interface and the velocities at the cell faces are used to determine the liquid fluxes across each face during each time step.

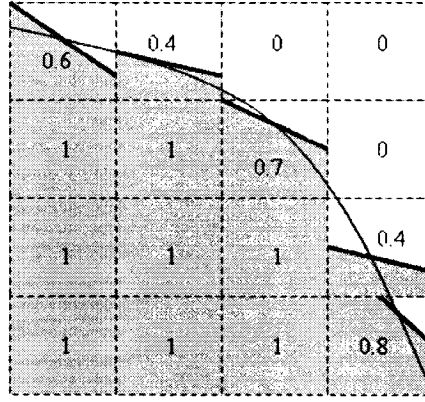


Figure 2.5: Interface representation at computational cells, PLIC method

Liquid fluxes across the cell faces are calculated based on an operator-split method. In this method, fluxes are calculated in each direction independently and in order. Following the calculation of fluxes in each direction, intermediate interfaces are reconstructed. Directional biased is minimized by changing the order of the advection from one time step to the next. Figure 2.6 illustrates a simple schematic showing the flux advection in the x -direction. Following is the method used to calculate the volume fraction advection.

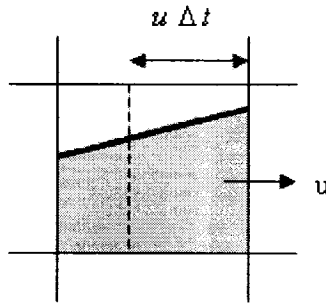


Figure 2.6: Volume fraction advection

The advection calculation begins with a reconstruction of the interface, followed by evaluation of a first interim field $f'_{i,j,k}$:

$$f'_{i,j,k} = \frac{f_{i,j,k}^n \Omega_{i,j,k} - \left(u_{i+\frac{1}{2},j,k}^{n+1} \langle f \rangle_{i+\frac{1}{2},j,k} - u_{i-\frac{1}{2},j,k}^{n+1} \langle f \rangle_{i-\frac{1}{2},j,k} \right) \Delta y_j \Delta z_k \Delta t}{\Omega'_{i,j,k}} \quad (2.27)$$

where

$$\Omega'_{i,j,k} = \Omega_{i,j,k} - \left(u_{i+\frac{1}{2},j,k} - u_{i-\frac{1}{2},j,k} \right) \Delta y_j \Delta z_k \Delta t \quad (2.28)$$

The interim field is reconstructed and the field is advected in the second direction:

$$f''_{i,j,k} = \frac{f'_{i,j,k} \Omega'_{i,j,k} - \left(v_{i,j+\frac{1}{2},k}^{n+1} \langle f \rangle_{i,j+\frac{1}{2},k} - v_{i,j-\frac{1}{2},k}^{n+1} \langle f \rangle_{i,j-\frac{1}{2},k} \right) \Delta x_i \Delta z_k \Delta t}{\Omega''_{i,j,k}} \quad (2.29)$$

where

$$\Omega''_{i,j,k} = \Omega'_{i,j,k} - \left(v_{i,j+\frac{1}{2},k} - v_{i,j-\frac{1}{2},k} \right) \Delta x_i \Delta z_k \Delta t \quad (2.30)$$

The second interim field is then reconstructed, followed by the evaluation of $f_{i,j,k}^{n+1}$

$$f_{i,j,k}^{n+1} = \frac{f''_{i,j,k} \Omega''_{i,j,k} - \left(w_{i,j,k+\frac{1}{2}}^{n+1} \langle f \rangle_{i,j,k+\frac{1}{2}} - w_{i,j,k-\frac{1}{2}}^{n+1} \langle f \rangle_{i,j,k-\frac{1}{2}} \right) \Delta x_i \Delta y_j \Delta t}{\Omega_{i,j,k}} \quad (2.31)$$

In the above equations the order of the advection is x - y - z . The $\langle f \rangle$ refers to the volume fractions of the *flux volume* and thus are not equal to the volume fractions of considering cell unless the cell is full or empty or the interface lies parallel to the flux direction.

Youngs [27] presents geometric algorithms to evaluate $\langle f \rangle$ for various interface geometries. These algorithms are somehow complex and are not repeated here.

2.2.6. Time Step Restriction

Since the evaluation of the convective, viscous and surface tension forces are performed explicitly, there should be a restriction for the computational time step to guarantee that the fluxes are not advected more than one computational cell at each time step. To implement this restriction, Courant number should be less than one.

$$\max \left[\frac{|u_{i,j,k}| \Delta t}{\Delta x_i}, \frac{|v_{i,j,k}| \Delta t}{\Delta y_j}, \frac{|w_{i,j,k}| \Delta t}{\Delta z_k} \right] < 1 \quad (2.32)$$

Additionally, the momentum can not diffuse more than one cell per time step:

$$\Delta t < \frac{\rho}{\mu} \cdot \min \left[\frac{(\Delta x_i)^2 (\Delta y_j)^2}{(\Delta x_i)^2 + (\Delta y_j)^2}, \frac{(\Delta x_i)^2 (\Delta z_k)^2}{(\Delta x_i)^2 + (\Delta z_k)^2}, \frac{(\Delta z_k)^2 (\Delta y_j)^2}{(\Delta z_k)^2 + (\Delta y_j)^2} \right] \quad (2.33)$$

And finally, there is a time limitation in modeling surface tension force as proposed by Brackbill et al. [28]:

$$\Delta t < \sqrt{\frac{\rho}{4\pi\sigma}} \min \left[(\Delta x_i)^{3/2}, (\Delta y_j)^{3/2}, (\Delta z_k)^{3/2} \right] \quad (2.34)$$

The minimum time step is selected from equations (2.32), (2.33), and (2.34) to guarantee stability of the solution.

2.3. Boundary Conditions

Boundary conditions required to solve the governing equations for the liquid phase generally consists of two parts; one is the boundary conditions needed at the computational domain boundaries and the other one is the boundary condition required at the liquid-gas interface. A boundary condition at the interface is needed because the computational code only solves the governing equations for the liquid phase and the effect of the surrounding gas is implemented by the means of the interface boundary condition. This section includes the domain boundary condition required for different problems and explains the method used to implement the interface boundary. Interface boundary is modified in this work and is applied using linear stability theory which is described completely in Chapter 3.

2.3.1. Domain Boundary Conditions

Based on the type of the problem being considered, domain boundary conditions are defined. Different problems reviewed in this study are shown in Figure 2.7. The 2D analysis considers both breakup time and breakup length of liquid sheets. The 3D analysis studies the breakup length of liquid sheets considering inflow/outflow boundaries in the stream-direction and periodic boundary condition in the span-direction. Following is a brief description about domain boundary conditions applied for each type of problems.

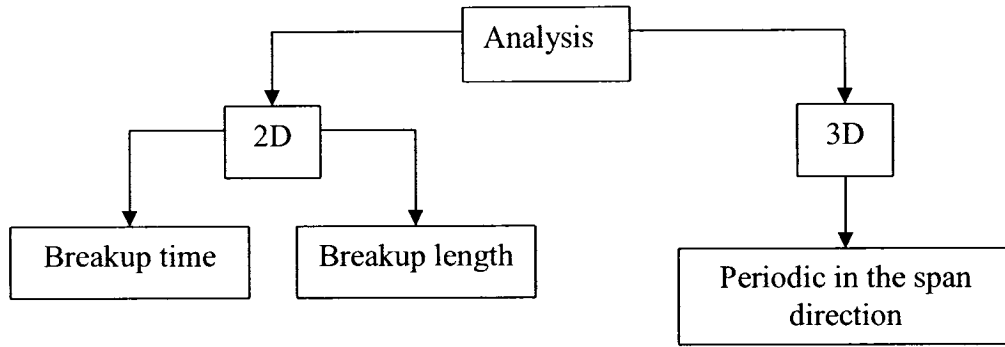


Figure 2.7: Flow chart of the analyses performed

To study the breakup time of the liquid sheet, time evolution of the sheet is considered and it is assumed that what happens in the computational domain is repeated exactly in the neighboring domains. As a result, a periodic boundary condition is required in the flow direction. As the main flow is assumed to be in the x -direction, boundary conditions in this direction are set to periodic. A periodic boundary is developed and added to the VOF solver explained in Chapter 2. Details of the developed code are presented in Appendix A. The boundary condition in the z -direction is set to outflow boundaries. The boundary conditions for temporal analysis are illustrated in Figure 2.8.

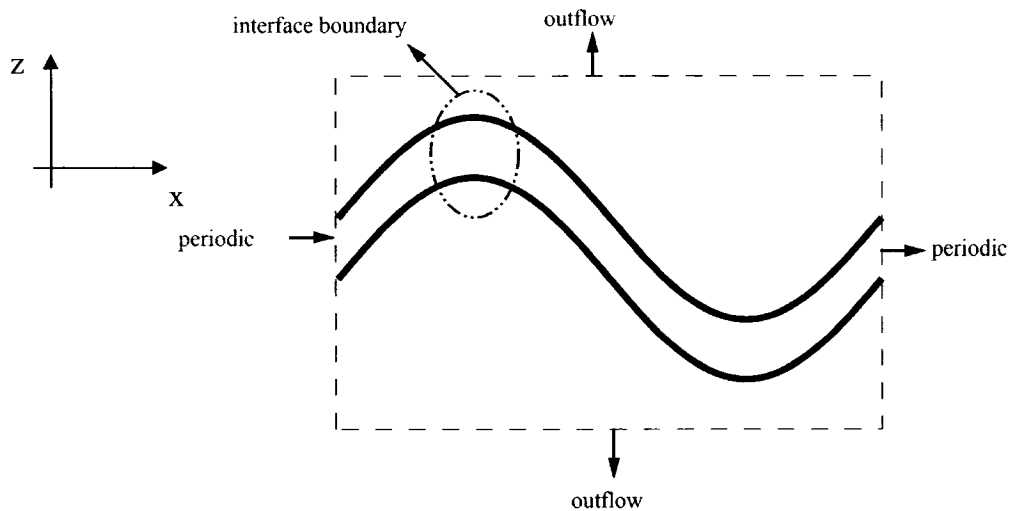


Figure 2.8: Boundary conditions for temporal analysis

To find the breakup length of liquid sheets, the spatial evolution of the sheet is studied. As a result, the liquid sheet comes in the computational domain through an inflow boundary and leaves the domain from an outflow boundary. Domain length is defined such that the liquid sheet disintegrates into smaller ligaments before leaving the computational domain. Boundary conditions in the z -direction are set to outflow as shown in Figure 2.9.

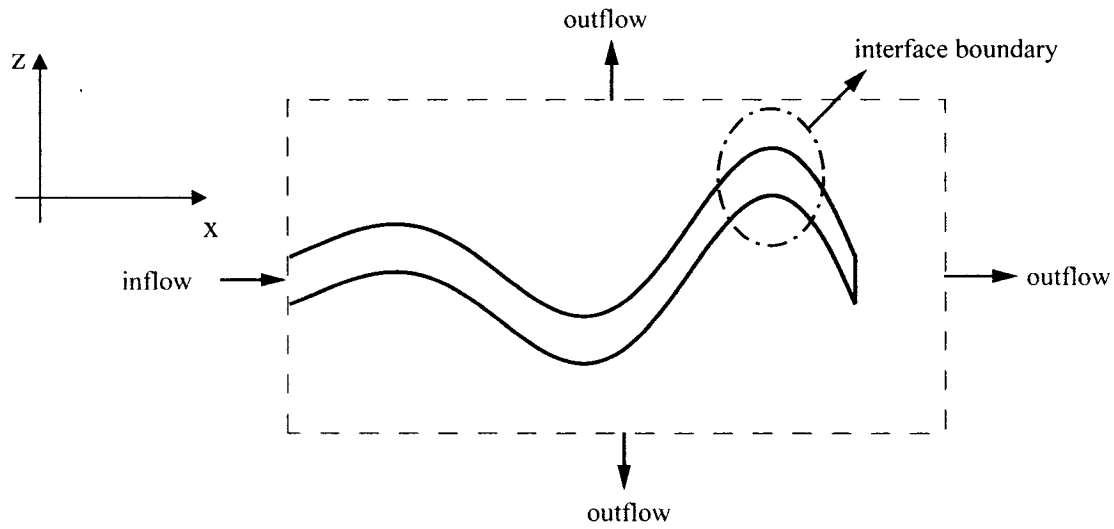


Figure 2.9: Boundary conditions for spatial analysis

For three-dimensional problems a periodic boundary condition is applied in the third direction (y -direction) while keeping inflow-outflow boundary in the flow direction. This type of the analysis includes 3D effects not affected by the presence of the free edge.

2.3.2. Interface Boundary Condition

Since the aerodynamic forces acting on the liquid-gas interface are the major source of the breakup process, the free surface boundary has a significant effect on the results. The

velocity boundary condition at the free surface is implemented by defining two velocities; external and tangential velocities. External velocities are imposed at cell faces between an interface cell and an empty cell while tangential velocities are defined at faces between two empty cells next to interface cells. These velocities are demonstrated in Figure 2.10.

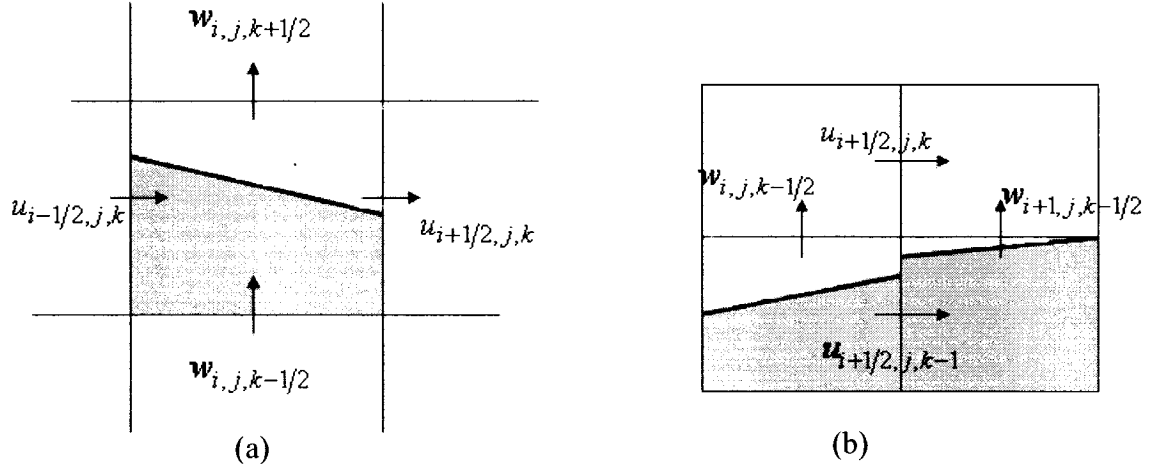


Figure 2.10: Interface velocities, (a) external velocity, $w_{i,j,k+1/2}$, (b) tangential velocity, $u_{i+1/2,j,k}$

External velocities are set according to the continuity equation. For example, in Figure 2.10 (a):

$$w_{i,j,k+1/2} = \left[\frac{\mu_g}{\mu_l} (w_{gas} - w_{i,j,k-1/2}) + w_{i,j,k-1/2} \right] - \Delta z / \Delta x (u_{i+1/2,j,k} - u_{i-1/2,j,k}) \quad (2.35)$$

where μ_g and μ_l are the gas and liquid viscosities and w_{gas} is the constant gas velocity in the z -direction. Tangential velocities are calculated based on the continuity of the shear stress across the interface. For instance, in Figure 2.10 (b),

$$u_{i+1/2,j,k} = \frac{\mu_g}{\mu_l} \times (u_{gas} - u_{i+1/2,j,k-1}) + u_{i+1/2,j,k-1} \quad (2.36)$$

u_{gas} is the gas velocity in the x -direction. u_{gas} and w_{gas} are constant through the simulation. Since the order of the magnitude of the gas viscosity is smaller than that of the liquid viscosity, u_{gas} and w_{gas} have a small effect on the interface velocity. In the problems where the gas velocity and pressure are important, the mentioned boundary conditions underestimate the effect of the gas phase and may lead to smearing the instabilities generated on the liquid-gas interface. To overcome this problem, the interface boundary condition has been modified for the present work and is implemented using the linear stability theory.

3. Linear Stability Theory

Linear stability analysis assumes that there are infinite number of infinitesimal disturbances traveling on the surfaces of the liquid sheet. These disturbances have different wavelengths, frequencies and growth rates. The general mathematical formulation of these disturbances is a function of space and time and can be stated as:

$$\eta = \text{Real}(\eta_0 \exp(i(kx - \omega t))) \quad (3.1)$$

where η is the disturbance amplitude (deviation from the undisturbed sheet) and is measured from the sheet centerline as indicated in Figure 3.1, η_0 is the initial amplitude, k is the wave number ($k = 2\pi/\lambda$ where λ is the wavelength), and ω is the wave frequency.

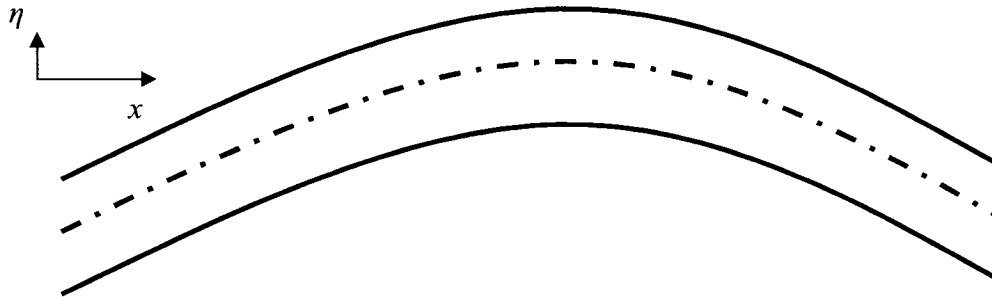


Figure 3.1: Disturbances traveling on the liquid sheet

The instability with the highest growth rate is identified as the most unstable disturbance which causes the liquid sheet to breakup into smaller ligaments. To find the most unstable wave, a mathematical function between wavelengths, frequencies and growth rates which satisfies the governing equations of the flow field is required. This mathematical function is so called “dispersion equation”, [12], and obtaining this equation has been the main subject of the linear stability analyses conducted so far [12], [13], [14], [17], and [18].

Linear stability analysis can be performed either temporally or spatially. Temporal linear stability analysis is responsible to find the breakup time of liquid sheets while the breakup length of liquid sheet is analyzed based on the spatial linear stability analysis. Because the difference between the temporal and spatial analyses is in the boundary conditions applied, the governing equations needed to be solved are first described following by the appropriate boundary conditions required for each analysis.

Since it is assumed that disturbances are small and infinitesimal, small disturbance variables are added to the flow variables. Therefore, each variable has two parts; the main part and the disturbance part. Since the main flow is assumed to be in the x -direction, the main velocities in the y - and z -directions are assumed to be zero. The flow variables can then be stated as:

$$\begin{aligned}\bar{u} &= U + u \\ \bar{v} &= v \\ \bar{w} &= w \\ \bar{p} &= p\end{aligned}\tag{3.2}$$

where the small variables demonstrate the disturbance variables. Governing equations for fluids contain mass and momentum conservation equations and are stated as:

$$\frac{\partial \bar{u}}{\partial x} + \frac{\partial \bar{v}}{\partial y} + \frac{\partial \bar{w}}{\partial z} = 0\tag{3.3}$$

$$\frac{\partial \bar{u}}{\partial t} + \bar{u} \frac{\partial \bar{u}}{\partial x} + \bar{v} \frac{\partial \bar{u}}{\partial y} + \bar{w} \frac{\partial \bar{u}}{\partial z} = -\frac{1}{\rho} \frac{\partial \bar{p}}{\partial x} + \nu \left(\frac{\partial^2 \bar{u}}{\partial x^2} + \frac{\partial^2 \bar{u}}{\partial y^2} + \frac{\partial^2 \bar{u}}{\partial z^2} \right) \quad (3.4)$$

$$\frac{\partial \bar{v}}{\partial t} + \bar{u} \frac{\partial \bar{v}}{\partial x} + \bar{v} \frac{\partial \bar{v}}{\partial y} + \bar{w} \frac{\partial \bar{v}}{\partial z} = -\frac{1}{\rho} \frac{\partial \bar{p}}{\partial y} + \nu \left(\frac{\partial^2 \bar{v}}{\partial x^2} + \frac{\partial^2 \bar{v}}{\partial y^2} + \frac{\partial^2 \bar{v}}{\partial z^2} \right) \quad (3.5)$$

$$\frac{\partial \bar{w}}{\partial t} + \bar{u} \frac{\partial \bar{w}}{\partial x} + \bar{v} \frac{\partial \bar{w}}{\partial y} + \bar{w} \frac{\partial \bar{w}}{\partial z} = -\frac{1}{\rho} \frac{\partial \bar{p}}{\partial z} + \nu \left(\frac{\partial^2 \bar{w}}{\partial x^2} + \frac{\partial^2 \bar{w}}{\partial y^2} + \frac{\partial^2 \bar{w}}{\partial z^2} \right) \quad (3.6)$$

These equations are identical to the governing equations (2.1) and (2.2), expanded for 3-dimensions and neglect the body force. Surface tension force considered in section 2.2.3 as a body force would be implemented in linear stability analysis as a boundary condition. The next step is to implement the variables from equation (3.2) to the governing equations (3.3), (3.4), (3.5), and (3.6). The idea of the linear stability theory is to linearize the governing equations by neglecting second and higher order terms containing disturbance variables. Additionally, main flow variables can be considered constant and the derivatives of these variables are therefore zero. By these assumptions equations (3.3), (3.4), (3.5), and (3.6) become:

$$\frac{\partial u}{\partial x} + \frac{\partial v}{\partial y} + \frac{\partial w}{\partial z} = 0 \quad (3.7)$$

$$\frac{\partial u}{\partial t} + U \frac{\partial u}{\partial x} = -\frac{1}{\rho} \frac{\partial p}{\partial x} + \nu \left(\frac{\partial^2 u}{\partial x^2} + \frac{\partial^2 u}{\partial y^2} + \frac{\partial^2 u}{\partial z^2} \right) \quad (3.8)$$

$$\frac{\partial v}{\partial t} + U \frac{\partial v}{\partial x} = -\frac{1}{\rho} \frac{\partial p}{\partial y} + \nu \left(\frac{\partial^2 v}{\partial x^2} + \frac{\partial^2 v}{\partial y^2} + \frac{\partial^2 v}{\partial z^2} \right) \quad (3.9)$$

$$\frac{\partial w}{\partial t} + U \frac{\partial w}{\partial x} = -\frac{1}{\rho} \frac{\partial p}{\partial z} + \nu \left(\frac{\partial^2 w}{\partial x^2} + \frac{\partial^2 w}{\partial y^2} + \frac{\partial^2 w}{\partial z^2} \right) \quad (3.10)$$

As an example to demonstrate when higher order terms are neglected, consider one of convective terms in the x -momentum equation:

$$\bar{u} \frac{\partial \bar{u}}{\partial x} = (U + u) \frac{\partial (U + u)}{\partial x} = U \frac{\partial U}{\partial x} + U \frac{\partial u}{\partial x} + u \frac{\partial U}{\partial x} + u \frac{\partial u}{\partial x} = U \frac{\partial u}{\partial x} + u \frac{\partial u}{\partial x} \approx U \frac{\partial u}{\partial x}$$

Appropriate boundary conditions are required to solve linearized governing equations. As mentioned before, these boundary conditions depend on the type of the analysis conducted. Boundary conditions needed for each analysis and resulting solution, i.e. dispersion equation, are presented separately for temporal and spatial analyses. Although the linearized governing equations and boundary conditions presented in this chapter are for viscous liquid sheets, it would be helpful to note that inviscid dispersion equation is used through this work. To investigate viscous effects on the breakup process, the liquid viscosity is changed in the computational code keeping the maximum growth rate and the corresponding wavelength equal to those of the inviscid case.

3.1. Temporal Linear Stability Analysis

To investigate the time evolution of the liquid sheet, temporal linear stability analysis is applied at the liquid-gas interface. This theory deals with the effect of different flow parameters on the breakup time of the liquid sheet. Consider equation (3.1) which represents the general equation of the disturbances. In the temporal analysis, k has only a

real part, $k=k_r$, while ω has both real and imaginary parts, $\omega = \omega_r + i\omega_i$. The reason for these definitions is further explained. Simplifying equation(3.1) with the assumptions made for k and ω gives:

$$\begin{aligned}
 \eta &= \text{Real}(\eta_0 \exp[i(k_r x - (\omega_r + i\omega_i)t)]) \\
 \eta &= \text{Real}(\eta_0 \exp(ik_r x - i\omega_r t + \omega_i t)) \\
 \eta &= \text{Real}(\eta_0 \exp(\omega_i t) \exp(i(k_r x - \omega_r t))) \\
 \eta &= \eta_0 \exp(\omega_i t) \text{Real}(\exp(i(k_r x - \omega_r t))) \\
 \eta &= \eta_0 \exp(\omega_i t) \text{Real}(\cos(k_r x - \omega_r t) + i \sin(k_r x - \omega_r t)) \\
 \eta &= \eta_0 \exp(\omega_i t) \cos(k_r x - \omega_r t)
 \end{aligned} \tag{3.11}$$

In equation (3.11) η_0 is a constant and the value of $\cos(k_r x - \omega_r t)$ is limited between zero and one. However the exponential part, $\exp(\omega_i t)$, which is a function of time, is responsible for the growth of the disturbance amplitude, η . This fact demonstrates the reason for the assumptions made to define k and ω . In equation (3.11), k_r is the wave number, ω_r is the wave frequency and ω_i is called the growth rate. Using equation (3.11) as the disturbance amplitude, the location of the sheet surface measured from the sheet center line can be stated as (sheet thickness is $2h$):

$$z = \pm h + \eta \tag{3.12}$$

The next step is to set the appropriate boundary conditions. As the main flow is in the x -direction and only the variation in time is important, the boundary condition in this direction is periodic. At the liquid-gas interface, three boundary conditions should be satisfied: (1) the velocity of the interface is equal to the time derivative of the location of the interface, (2) the shear stress is zero at the interface, and (3) the surface tension effect is equal to the pressure jump across the interface. These can be stated mathematically as:

$$\begin{aligned}
 w &= \frac{\partial \eta}{\partial t} = \eta_0 \exp(\omega_i t) \times [\omega_i \cos(k_r x - \omega_r t) + \omega_r \sin(k_r x - \omega_r t)] \\
 \frac{\partial u}{\partial z} + \frac{\partial w}{\partial x} &= 0 \\
 -p_l + 2\mu_l \frac{\partial w}{\partial z} + p_g &= \sigma \frac{\partial^2 \eta}{\partial x^2}
 \end{aligned} \tag{3.13}$$

These boundary conditions are applied at the liquid sheet interface. The location of the interface is calculated based on equation (3.12). There are various methods to solve equations (3.7), (3.8), (3.9), and (3.10) by applying the above mentioned boundary conditions. The most practical one is using the stream and potential functions approach. This method is presented in [12] and [14] and not repeated here. As mentioned before, the result would be an equation which states the relation between the wave numbers and growth rates of the waves traveling on the liquid sheet (so called dispersion equation). The inviscid solution can be stated as:

$$\left(\frac{\omega_i h}{U} \right) = \left(\frac{\rho_g / \rho_l}{We_g} \right)^{0.5} \times \frac{k_r h}{\rho_g / \rho_l + \tanh(k_r h)} \times \sqrt{We_g \times \tanh(k_r h) - (k_r h) \times (\rho_g / \rho_l + \tanh(k_r h))} \tag{3.14}$$

where We_g is the gas-based Weber number. The main velocity of the liquid sheet and half of the sheet thickness have been used to non-dimensionlize the variables. As equation (3.14) shows, the parameters affecting the dispersion equation are gas to liquid density ratio and gas based Weber number. This fact indicates that these parameters determine the most unstable wave traveling on the surfaces of the liquid sheet. To show the variation of the dispersion equation with flow parameters, equation (3.14) is plotted for different gas to liquid density ratios and different Weber numbers. The maximum growth rate and corresponding wavelength can be found by solving the equation: $d\omega_i/dk_r = 0$.

Figure 3.2 (a) shows that at a constant gas to liquid density ratio, the maximum growth rate increases by increasing the Weber number. Additionally, since the ligament size is a function of the dominant wavelength, an increase in the Weber number decreases the dominant wavelength which leads to the formation of smaller ligaments. The effect of the gas to liquid density ratio on the dispersion equation is illustrated in Figure 3.2 (b). As the gas to liquid density ratio increases, the maximum growth rate increases as well. The ratio, ρ_g/ρ_l does not change the most unstable wavelength considerably.

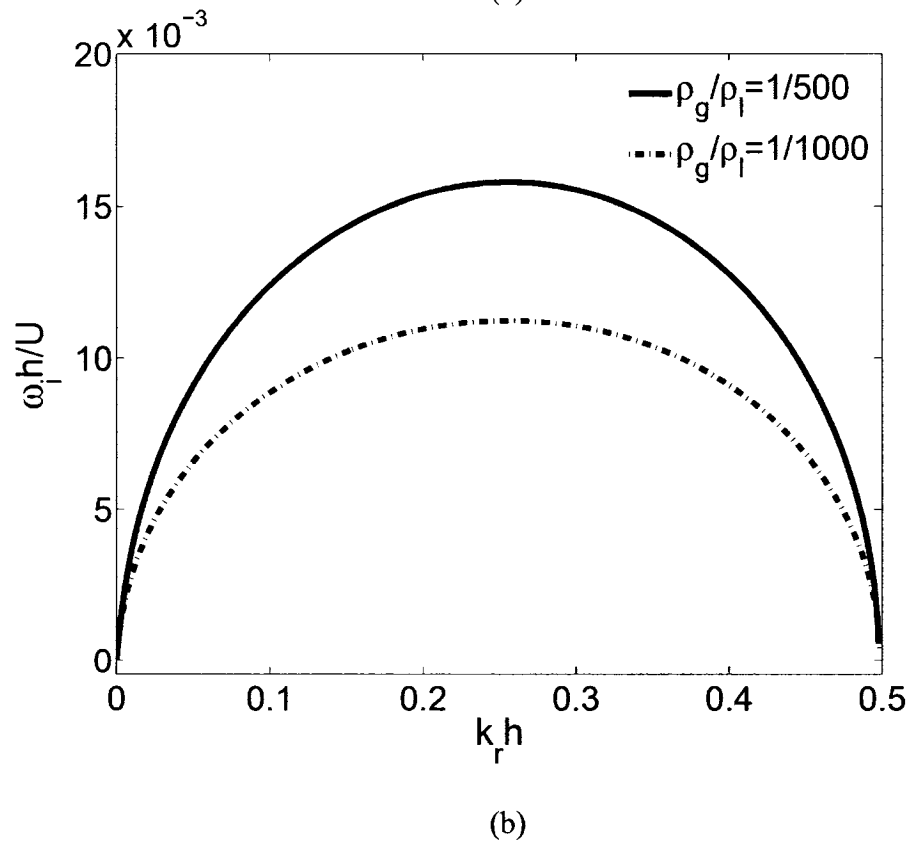
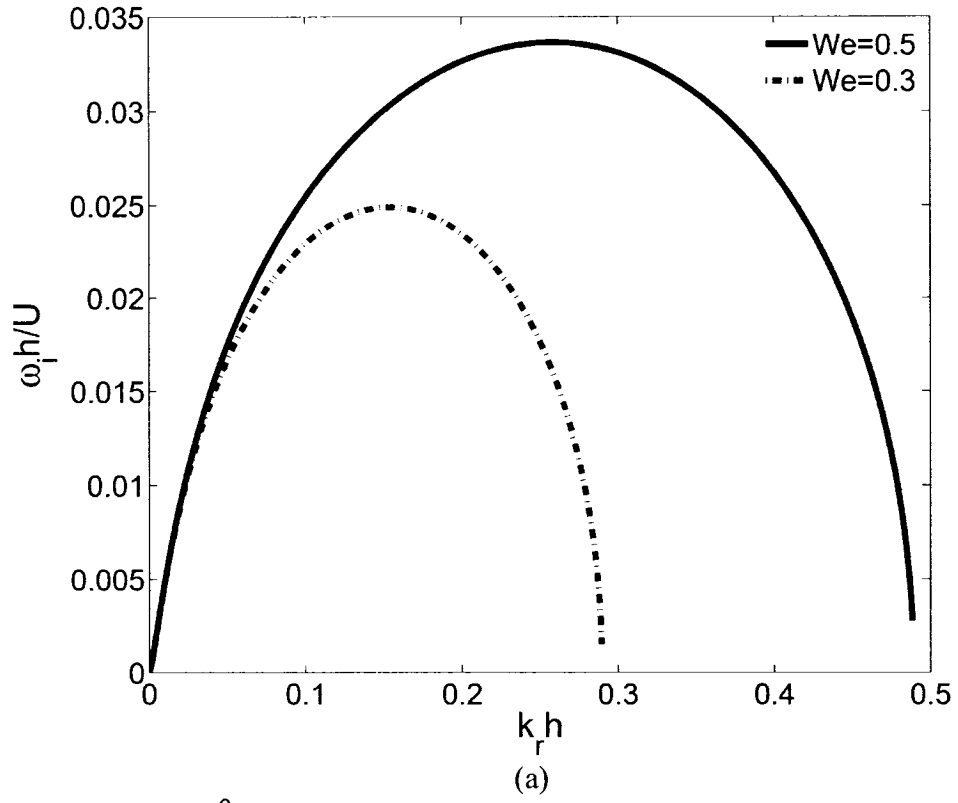


Figure 3.2: Solution of inviscid dispersion equation for (a) $\rho_g/\rho_l=1/100$ (b) $We_g=0.5$

At this point, the boundary condition required at the liquid-gas interface required for the computational code can be implemented. This implementation contains the following steps described below:

- Calculate Weber number and gas to liquid density ratio based on the sheet velocity, thickness and fluid properties.
- Find the maximum growth rate and corresponding wavelength by solving the dispersion equation for the non-dimensional numbers specified above.
- Apply the values corresponding to the most unstable wavelength to the disturbance equation, $\eta = \eta_0 \exp(\omega_i t) \cos(k_r x - \omega_r t)$.
- Estimate the time derivative of the location of the surface, $w = \partial \eta / \partial t$, to find the boundary velocity at computational cells containing the interface.

3.2. Spatial Linear Stability Analysis

To study the effect of flow parameters on the breakup length of the liquid sheet, spatial linear stability analysis is required. This theory assumes that the evolution of the liquid sheet in the space causes instabilities to grow and leads to the breakup of the liquid sheet. The development and implementation steps of the spatial theory are similar to those of the temporal theory. Again consider equation (3.1) which represents the general equation for the disturbances. In the spatial analysis, ω has only a real part, $\omega = \omega_r$ while the k contains both real and imaginary parts, $k = k_r + ik_i$. By applying these assumptions, the disturbance equation becomes:

$$\begin{aligned}
\eta &= \text{Real}(\eta_0 \exp[i((k_r + ik_i)x - \omega_r t)]) \\
\eta &= \text{Real}(\eta_0 \exp(ik_r x - k_i x - i\omega_r t)) \\
\eta &= \text{Real}(\eta_0 \exp(-k_i x) \exp(i(k_r x - \omega_r t))) \\
\eta &= \eta_0 \exp(-k_i x) \text{Real}(\exp(i(k_r x - \omega_r t))) \\
\eta &= \eta_0 \exp(-k_i x) \text{Real}(\cos(k_r x - \omega_r t) - i \sin(k_r x - \omega_r t)) \\
\eta &= \eta_0 \exp(-k_i x) \cos(k_r x - \omega_r t)
\end{aligned} \tag{3.15}$$

where ω_r is the wave frequency, k_r is the wave number, and k_i is the growth rate of the instabilities. As demonstrated by equation (3.15), in spatial analysis, the exponential part of the disturbance equation is a function of space and may grow as the liquid sheet evolves in the x -direction. This fact can justify the way k and ω are defined in the spatial analysis. Next step is to solve the linearized governing equations that are subjected to appropriate boundary conditions.

The boundary conditions in the x -direction are inflow and outflow at the left and right boundaries, respectively. The boundary conditions needed at the liquid-gas interface can be stated as:

$$\begin{aligned}
w &= \frac{\partial \eta}{\partial t} = \eta_0 \omega_r \exp(-k_i x) \sin(k_r x - \omega_r t) \\
\frac{\partial u}{\partial z} + \frac{\partial w}{\partial x} &= 0 \\
-p_l + 2\mu_l \frac{\partial w}{\partial z} z + p_g &= \sigma \frac{\partial^2 \eta}{\partial x^2}
\end{aligned} \tag{3.16}$$

The physical explanation of these boundary conditions is the same as the temporal ones mentioned before. The solution of the linearized governing equations by implementing the above boundary conditions would result in the dispersion equation for the spatial linear stability analysis. The method, which has been used to find the dispersion equation, is the stream and potential functions approach [13]. Details of the calculations are not repeated here. The inviscid solution of the dispersion equation can be stated as [13]:

$$k_i h = (k_r h) \times \left(\frac{\rho_g / \rho_l - k_r h / We_l}{\tanh(k_r h)} \right)^{0.5} \tag{3.17}$$

where We_l is liquid-based Weber number. The maximum growth rate and corresponding wavelength can be found by solving $dk_i/dk_r = 0$. The effects of Weber number and gas to liquid density ratio on the maximum growth rate and corresponding wavelength are illustrated in Figure 3.3. As the Weber number increases, the maximum growth rate increases as well and the most unstable wave shifts to smaller wavelengths (See Figure 3.3 (a)). Figure 3.3 (b) demonstrates the solution of the dispersion equation at $We_l=500$ for two different gas to liquid density ratios. The maximum growth rate increases at higher gas to liquid density ratios. In contrast to the temporal case where the gas to liquid density ratio does not affect the dominant wavelength considerably, in the spatial case the

dominant wavelength decreases significantly as the gas to liquid density ratio increases. The same approach as the temporal analysis is required to implement the liquid-gas interface boundary condition in the computational code.

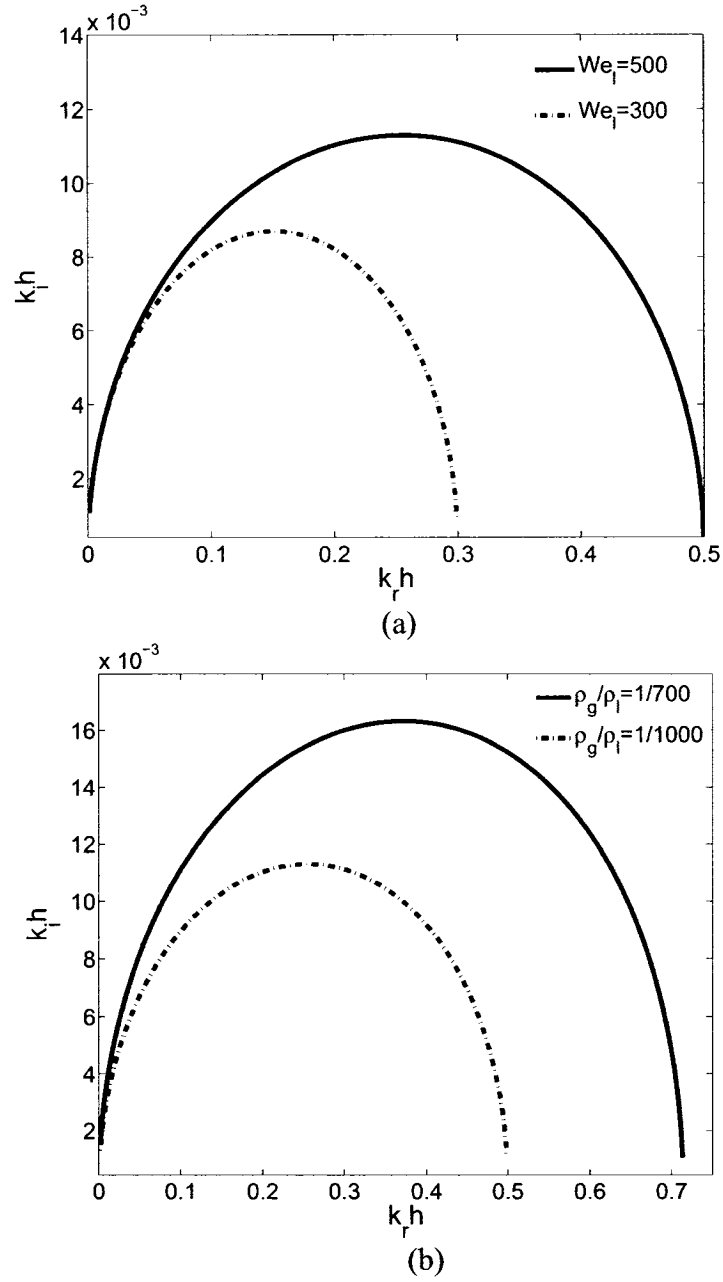


Figure 3.3: Inviscid solution of dispersion equation for spatial analysis for (a) $\rho_g/\rho_l=1/1000$ (b) $We_l=500$

4. Results

Numerical results based on the solution of the governing equations by implementing appropriate boundary conditions are presented in this chapter. Two-dimensional and three-dimensional results are presented in separate sections. As mentioned in the first chapter, span-wise ligaments are captured by 2D analysis while 3D analysis is required to capture both types of ligaments. Although 3D analysis is just an extension of the problem to the third dimension, this extension captures the stream-wise ligaments, generated physically due to 3D effects. In all the simulations it is assumed that the liquid sheet is leaving the nozzle exit with the main velocity of U in the x -direction and the surrounding gas is stationary.

4.1. Two-Dimensional Results

The formation of span-wise ligaments is studied while investigating the effect of the fluid properties on the breakup process. In this section, the variation of the breakup time with fluid parameters is first presented followed by the study of the effect of these parameters on the breakup length of liquid sheets. Since the temporal dispersion equation is defined according to the gas-based Weber number, We_g is used to present the results for the breakup time, while the results for the breakup length are presented based on the liquid based Weber number, We_l .

4.1.1. Breakup Time

The breakup time of the liquid sheet is defined as the time required for the liquid sheet to disintegrate into smaller ligaments. Since the evolution of the sheet by time is considered, as described in chapter 2.3, the boundary condition in the x -direction is periodic and the interface boundary condition is implemented using temporal linear stability analysis described in section 3.1. The effect of the fluid properties and flow parameters on the breakup time of liquid sheets is studied through three non-dimensional numbers: gas based Weber number, Ohnesorge number and gas to liquid density ratio which can be stated mathematically as:

$$We_g = \frac{\rho_g U^2 h}{\sigma} \quad ; \quad Oh = \sqrt{We_l} / Re = \frac{\mu}{(\rho_l \sigma h)^{0.5}} \quad ; \quad \frac{\rho_g}{\rho_l} \quad (4.1)$$

the physical meaning of Ohnesorge number can be interpreted as the ratio of viscous force to surface tension force.

The grid size is selected to initially provide eight computational cells per sheet thickness with $\Delta x = \Delta z$. Since the boundary condition in the x -direction is periodic, the domain length in this direction is set equal to one wavelength corresponding to the maximum growth rate, λ_{max} . The initial amplitude of the disturbance, η_0 , in equation (3.11) is equal to $\eta_0 = 0.075 \lambda_{max}$ [12]. More discussion about the effect of the initial amplitude of the disturbance on the breakup is presented in section 4.3 of this chapter.

Non-dimensional breakup time is defined as $t^* = tU/h$. To show that t^* is only a function of the non-dimensional parameters (We_g , Oh , and ρ_g/ρ_l), three different cases with

different flow parameters but the same Weber and Ohnesorge numbers are shown in Table 4.1. For all three cases, the gas to liquid density ratio is equal to $\rho_g/\rho_l=1/100$. Results show that although the surface tension has been increased three times from case 1 to case 3, by changing the sheet velocity and liquid viscosity appropriately to keep Weber and Ohnesorge numbers constant, the variation in t^* is smaller than 2.2%.

	$U(m/s)$	$h(m)$	$\sigma (N/m)$	$\mu (kg/ms)$	We_g	Oh	t^*
Case 1	7.7	250×10^{-6}	30×10^{-3}	27×10^{-3}	0.5	1.0	34.5
Case 2	11	250×10^{-6}	60×10^{-3}	38×10^{-3}	0.5	1.0	34.01
Case 3	13.4	250×10^{-6}	90×10^{-3}	47×10^{-3}	0.5	1.0	33.77

Table 4.1: Exclusive dependency of the non-dimensional breakup time on the non-dimensional parameters for $\rho_g/\rho_l = 1/100$

Figure 4.1 illustrates the time evolution of a $500 \mu m$ thick liquid sheet. \tilde{t} corresponds to the breakup time. Figure 4.1 (a) demonstrates the initial disturbance imposed on the liquid sheet. By marching in time, the instability is amplified due to the interaction between liquid sheet and the surrounding gas as shown in Figure 4.1 (b). Enhancement of the disturbance thickens some parts of liquid sheet and shrinks other parts as illustrated in Figure 4.1 (c). Finally the liquid sheet breaks from thin parts and disintegrates into smaller ligaments as shown in Figure 4.1 (d). The effect of the gas to liquid density ratio can be identified by comparing Figures 4.1 and 4.2. As the gas to liquid density ratio increases the dominant wavelength decreases slightly resulting in ligaments with smaller size. A comparison between Figures 4.1 and 4.3 demonstrates the effect of Weber number. Increasing Weber number causes a decrease in the dominant wavelength corresponding to the maximum growth rate. The disintegration of liquid sheets into ligaments equal to half of the most dominant wavelength is obtained in all cases, which is the characteristic of the sinuous type of the disturbances considered in this work.

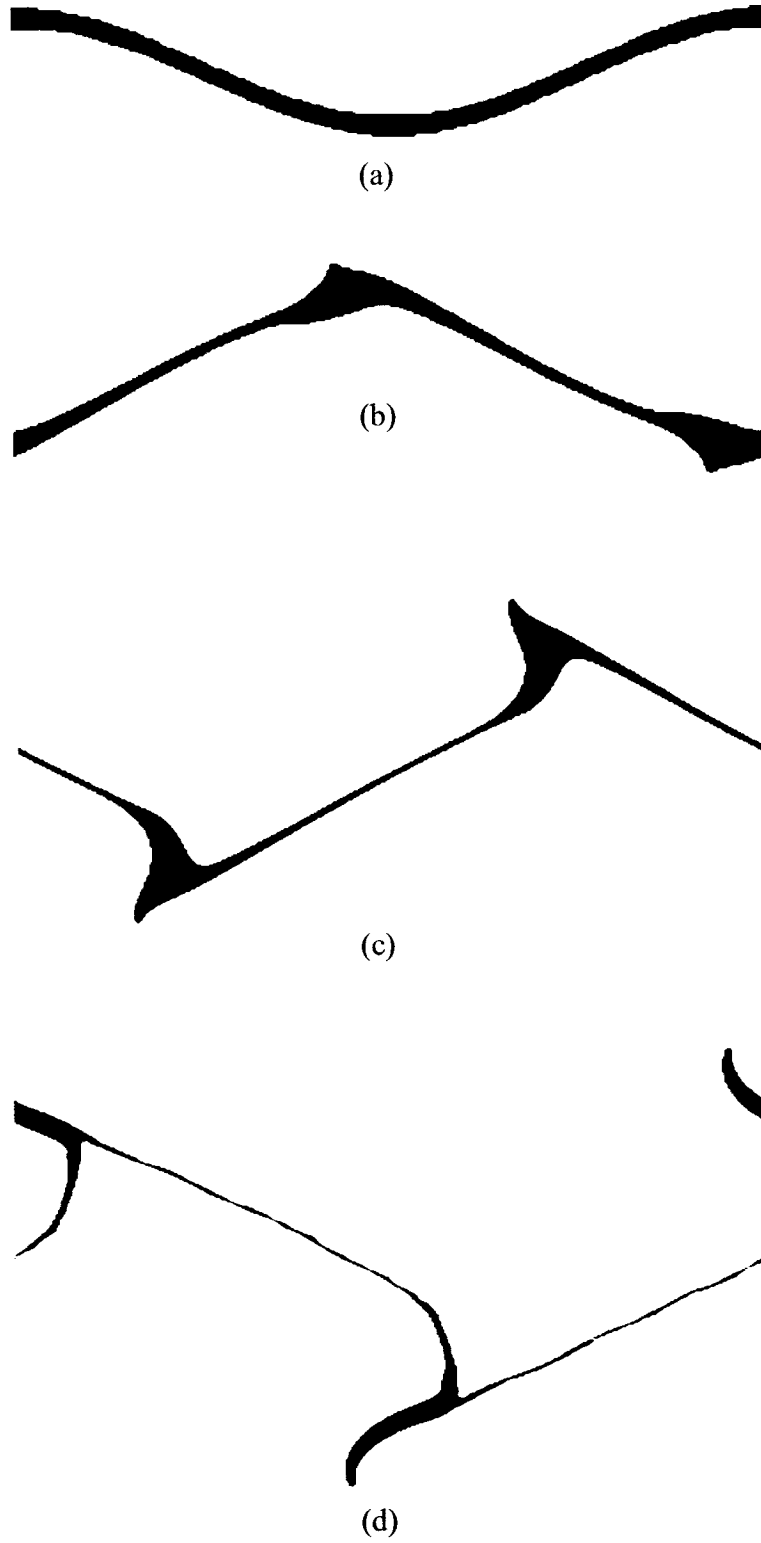


Figure 4.1: Time evolution of the liquid sheet for $We_g=0.3$, $Oh=1$, and $\rho_g/\rho_l=1/1000$, (a) $t^* = 0$, (b) $t^* = \tilde{t} / 4$, (c) $t^* = 3\tilde{t} / 4$, (d) $t^* = \tilde{t}$

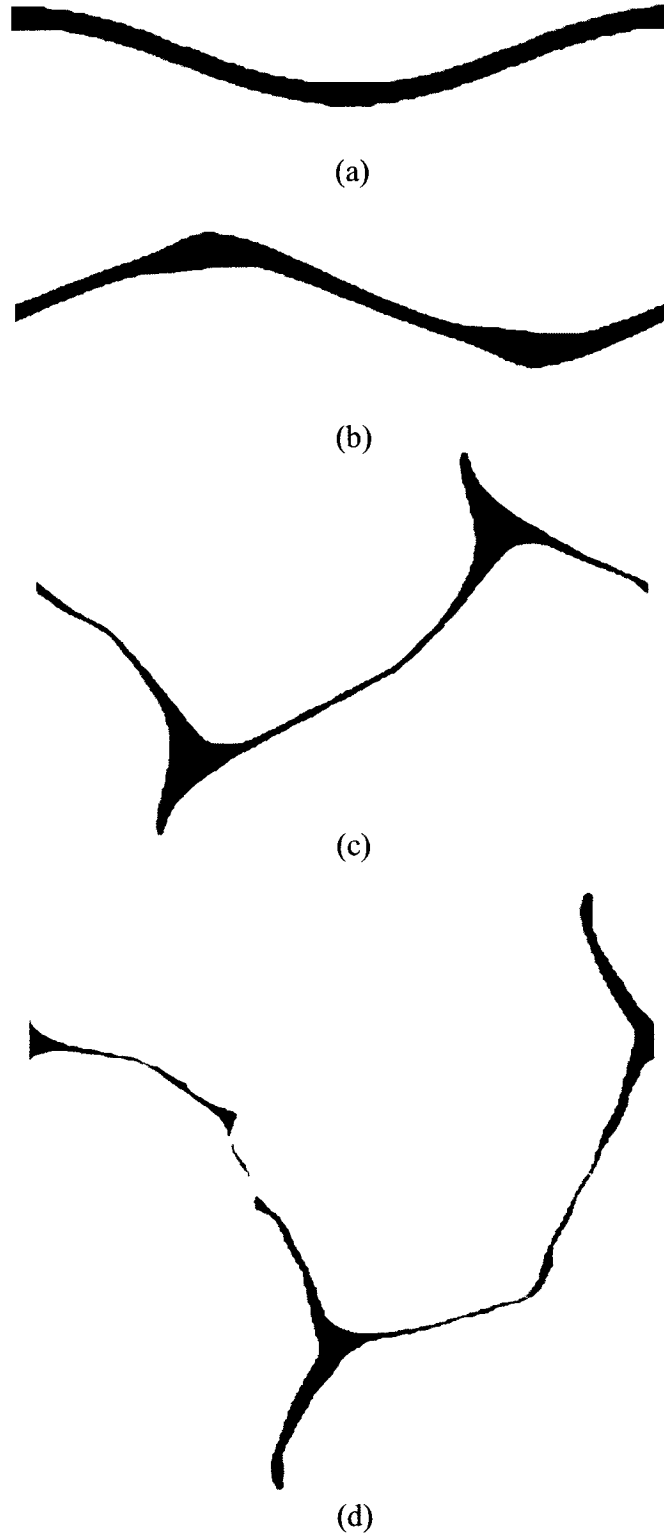


Figure 4.2: Time evolution of the liquid sheet for $We_g=0.3$, $Oh=1$, and $\rho_g/\rho_l=1/500$, (a) $t^*=0$, (b) $t^*=\tilde{t}/4$, (c) $t^*=3\tilde{t}/4$, (d) $t^*=\tilde{t}$



(a)



(b)



(c)



(d)

Figure 4.3: Time evolution of the liquid sheet for $We_g=0.5$, $Oh=1$, and $\rho_g/\rho_l=1/1000$, (a) $t^* = 0$, (b) $t^* = \tilde{t}/4$, (c) $t^* = 3\tilde{t}/4$, (d) $t^* = \tilde{t}$

The variations in the breakup time with the gas based Weber number is illustrated in Figure 4.4 for different gas to liquid density ratios for $Oh=1$. As the Weber number increases, the breakup time decreases showing the stabilizing effect of the liquid surface tension on the breakup process. Additionally, Figure 4.4 demonstrates that the breakup time decreases at higher values of the gas to liquid density ratio. This behavior is reported in [1], [12], and [14].

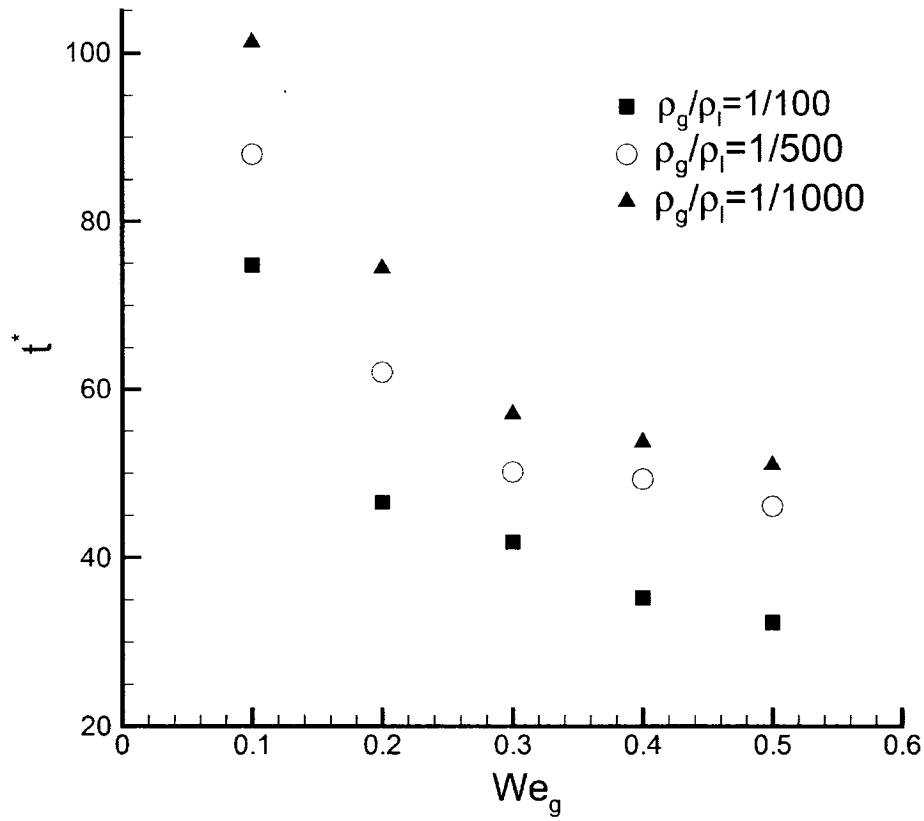


Figure 4.4: Effect of We_g and ρ_g/ρ_l on the breakup time for $Oh=1$

Li et al. [12] reported that at some specific range of We_g , which includes the range considered in this work, liquid viscosity has a destabilizing effect on the breakup process and the breakup time decreases by increasing the viscosity. This phenomenon is studied in the present work by changing the liquid viscosity while keeping the maximum growth

rate and the corresponding wavelength constant and equal to those of the inviscid case. Figure 4.5 illustrates the variation in the breakup time with Ohnesorge number for different Weber numbers at $\rho_g/\rho_l=1/500$ and $\rho_g/\rho_l=1/1000$. Results demonstrate that breakup time decreases as the Ohnesorge number increases showing the destabilizing effect of the liquid viscosity which is consistent with the work of Li et al.[12]

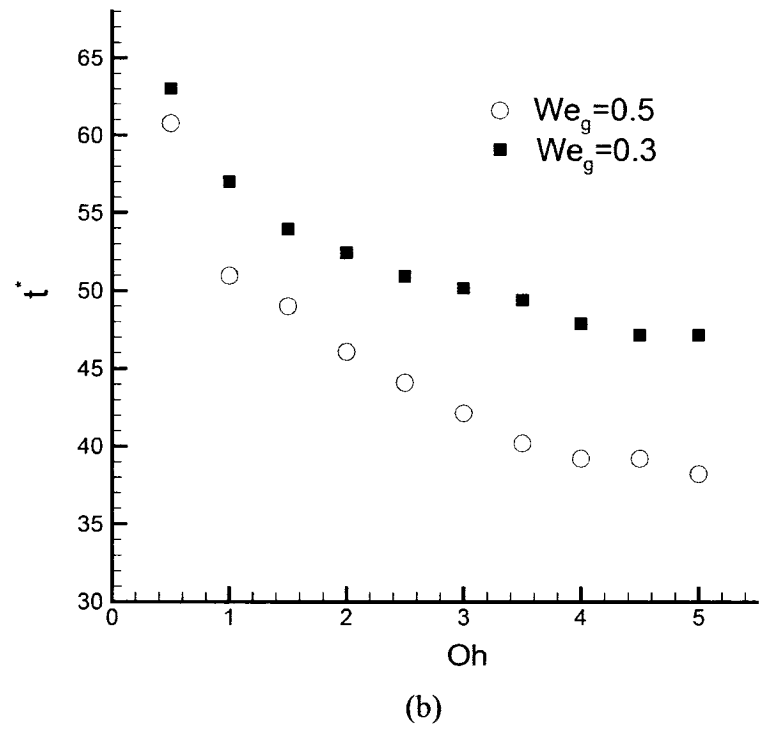
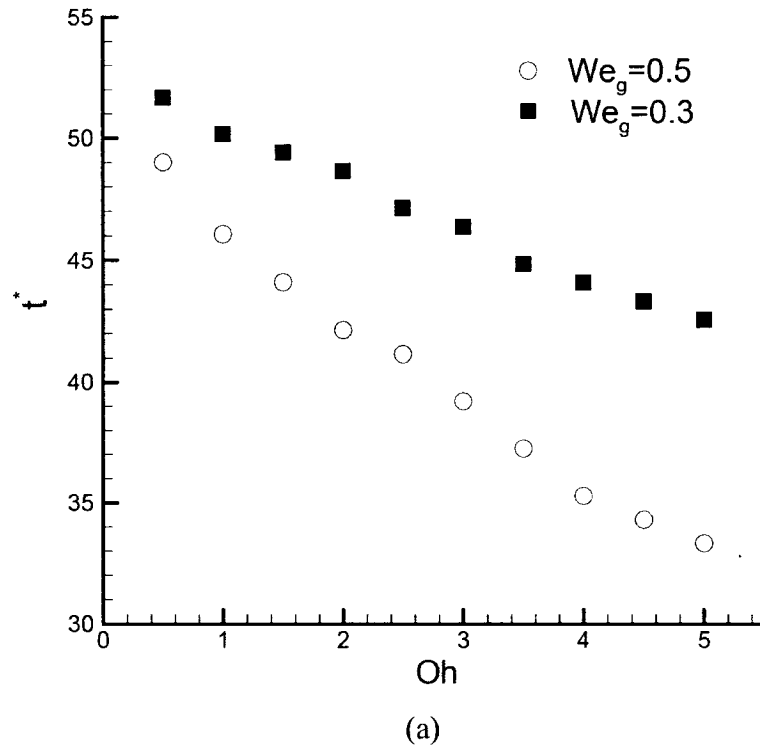


Figure 4.5: Effect of the Ohnesorge number on the breakup time, (a) $\rho_g/\rho_l=1/500$, (b) $\rho_g/\rho_l=1/1000$

4.1.2. Breakup Length

Breakup length is defined as the length in which the ligaments are separated from the liquid sheet. This length is shown in Figure 4.6.

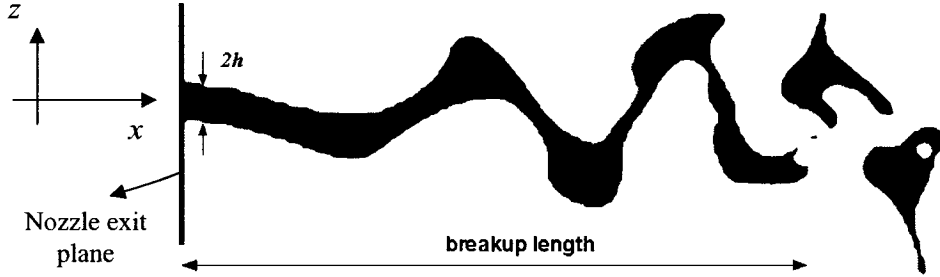


Figure 4.6: Breakup length

As described in chapter 2.3, boundary conditions required to solve the governing equations to find the breakup length is inflow/outflow in the x -direction and outflow/outflow in the z -direction. Furthermore, the boundary condition needed at the liquid-gas interface is implemented using spatial linear stability analysis. Non-dimensional parameters used to study the effect of flow parameters on the breakup length of liquid sheets are the same as the ones used in section 4.1.1 except, the Weber number is stated based on the liquid density.

$$We_l = \frac{\rho_l U^2 h}{\sigma} \quad ; \quad Oh = \frac{\mu}{(\rho_l \sigma h)^{0.5}} \quad ; \quad \frac{\rho_g}{\rho_l} \quad (4.2)$$

Similar to temporal analysis, the grid size is selected to have eight computational cells per sheet thickness at the inlet boundary with $\Delta x = \Delta z$. To guarantee that the liquid sheet breaks into ligaments before leaving the computational domain, the domain length in the

x -direction is defined as six times the dominant wave length corresponding to the maximum growth rate, λ_{max} . The initial amplitude is defined as $\eta_0 = 0.05 \lambda_{max}$ in equation (3.15) [13].

The non-dimensional breakup length is defined as the ratio of the breakup length to the sheet thickness, $L^* = L/2h$. Similar to the temporal analysis, to demonstrate that the breakup length is only a function of the above mentioned non-dimensional numbers, three different cases were examined with different flow conditions but with the same Weber and Ohnesorge numbers at the same gas to liquid density ratio. These cases are shown in Table 4.2. Comparing cases 1 and 3 indicates that even by doubling the surface tension but changing the sheet main velocity and the liquid viscosity to have the same Weber and Ohnesorge numbers, the change in the non-dimensional breakup length is less than 2.1%.

	$U(m/s)$	$h(m)$	$\sigma (N/m)$	$\mu (kg/ms)$	We_l	Oh	L^*
Case 1	8.6	250×10^{-6}	30×10^{-3}	77×10^{-3}	500	1.0	18.76
Case 2	12	250×10^{-6}	60×10^{-3}	110×10^{-3}	500	1.0	19.16
Case 3	15	250×10^{-6}	90×10^{-3}	136×10^{-3}	500	1.0	18.92

Table 4.2: Exclusive dependency of the non-dimensional breakup length on the non-dimensional parameters for $\rho_g/\rho_l = 1/800$

Evolution of a liquid sheet with a thickness of $500 \mu m$, $\rho_g/\rho_l = 1/1000$, and $Oh=1$ for different Weber numbers is shown in Figure 4.7. As indicated by the spatial linear stability theory, the most dominant wavelength decreases as the Weber number increases. Moreover, the breakup length decreases at higher values of the Weber number.

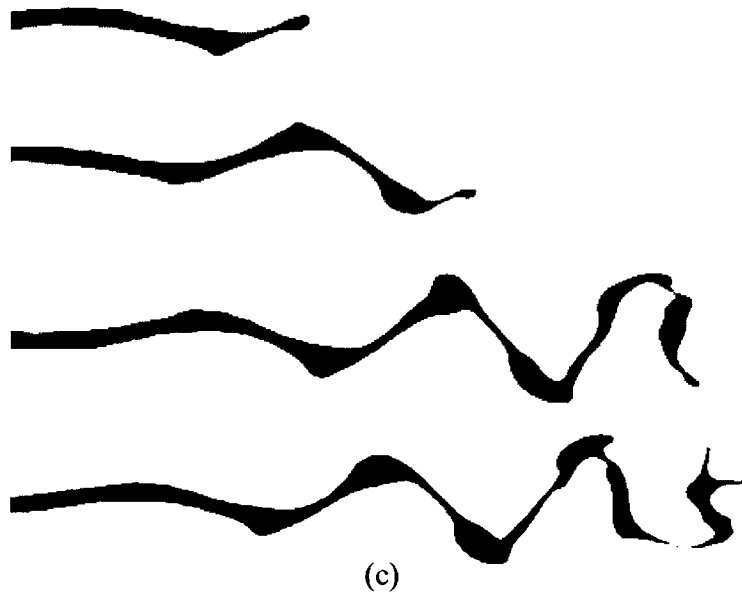
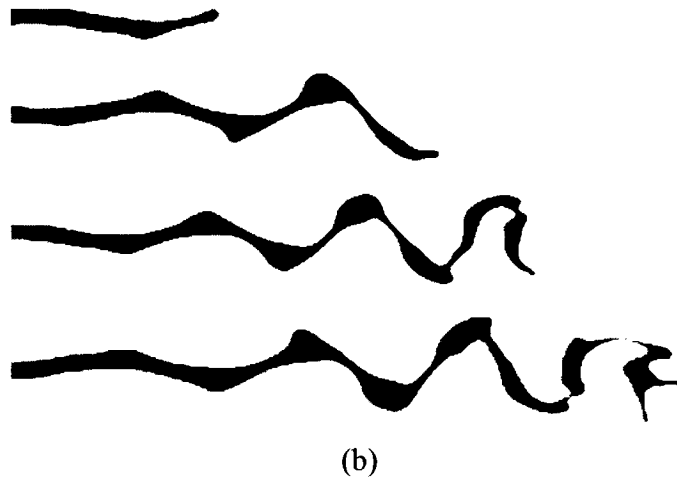
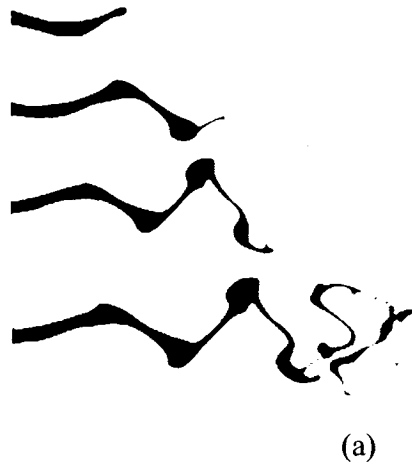


Figure 4.7: Spatial evolution of the liquid sheet with $\rho_g/\rho_l=1/1000$ and $Oh=1$ for various Weber numbers (a) $We_l=500$, (b) $We_l=400$, (c) $We_l=300$

To illustrate the effect of the gas to liquid density ratio on the spatial evolution of the liquid sheet, two different cases are shown in Figure 4.8 for $We_l=400$ and $Oh=1$. The breakup length decreases at higher values of the gas to liquid density ratio.

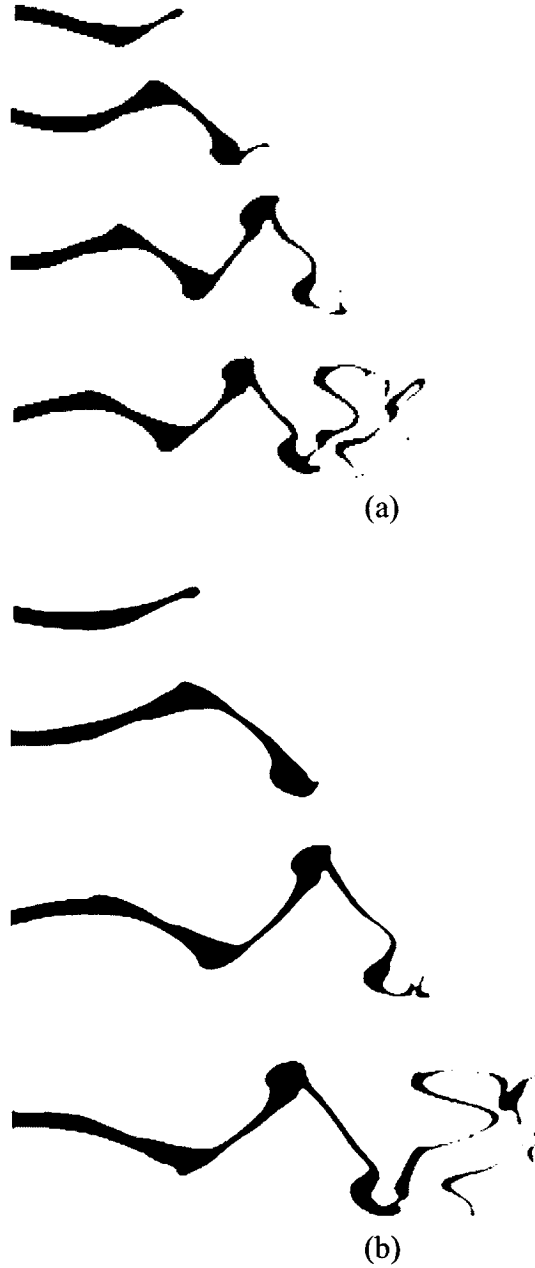


Figure 4.8: Spatial evolution of the liquid sheet with $We_l = 400$ and $Oh=1$ for various gas to liquid density ratios (a) $\rho_g/\rho_l=1/800$, (b) $\rho_g/\rho_l=1/1200$

Figure 4.9 demonstrates the variation of the non-dimensional breakup length with the Weber number, We_l , for different gas to liquid density ratios for $Oh=1$ (sheet thickness = $500 \mu m$). As the Weber number increases, the breakup length decreases which demonstrates the stabilizing effect of the liquid surface tension on the breakup mechanism. Additionally, at higher values of the ρ_g/ρ_l , the breakup length decreases. The same behavior has been reported by Li [13].

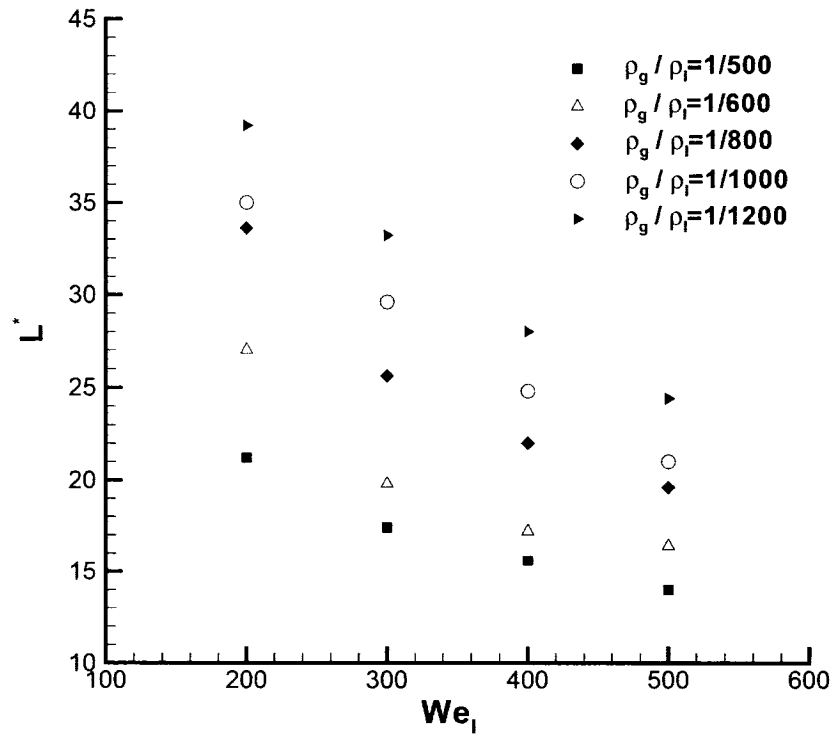


Figure 4.9: The effect of Weber number on the breakup length for different gas to liquid density ratios for $Oh=1$

Li [13] reported that the liquid viscosity stabilizes the liquid sheet by increasing the breakup length. Similar to the temporal part described in section 4.1.1, to investigate the

effect of the liquid viscosity, variation of the breakup length as a function of Ohnesorge number is studied while keeping the maximum growth rate and corresponding wavelength constant and equal to those of the inviscid case. The variation of breakup length with Ohnesorge number is shown in Figure 4.10 for $We_l=100$ and $\rho_g/\rho_l=1/1000$. As viscosity increases, the disturbances grow slower which results in an increase in the breakup length consistent with the work of Li [13].

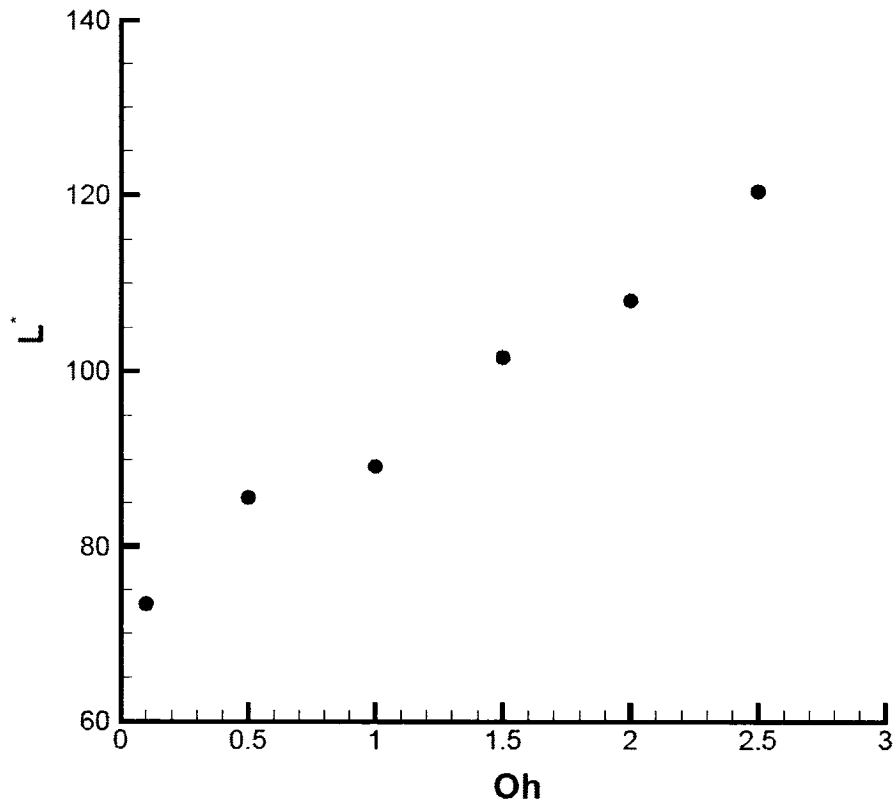


Figure 4.10: Variation of the breakup length with Ohnesorge number for $We_l=100$ and $\rho_g/\rho_l=1/1000$

4.2. Three-Dimensional Results

In this section, the liquid sheet is extended in the y -direction to include 3D effects in the breakup phenomenon. The results of the spatial linear stability analysis described in section 3.2 are used to find the maximum growth rate and the corresponding wavelength in the flow direction to implement the interface boundary condition. The 3D results are presented assuming periodic boundary condition in the span-direction (i.e. y -direction).

The liquid sheet emerging from the nozzle would have initial instabilities in the span-direction right at the nozzle exit. These instabilities might be generated due to the inner nozzle flow and the explosion of cavity bubbles as described in section 1.1. Generally, these instabilities have different wavelengths. Kim et al. [18] have shown that among all the instabilities in the span-direction, the one with the same wavelength as the most dominant wave in the flow direction would be dominant. Hence, once the wavelength corresponding to the most unstable wave in the flow direction (x -direction) is determined by the linear stability analysis (discussed in section 3.2) this wavelength is used to introduce the instabilities in the span-direction (y -direction) as well. The major difference between instabilities in the x - and y - directions is that the waves in the x -direction are moving while instabilities in the y -direction are stationary. In this work it is assumed that the liquid sheet is periodic in the span direction and it is disturbed by a wave with the wavelength equal to the most dominant wave in the flow direction. (A case with no initial disturbance in the span-direction is presented in Appendix B.)

Since the major goal of a three-dimensional analysis is to capture both kind of ligaments generated, the formation of span-wise and stream-wise ligaments are presented first followed by the effect of fluid properties on the breakup process. Figure 4.11 (a) illustrates a 3D view of the liquid sheet. Figures 4.11 (b) and (c) show the volume fraction of the liquid in stream- and span-direction planes respectively (shown in Figure 4.11 (a)). It can be seen that span-wise ligaments are generated similar to the 2D analysis (Figure 4.11 (b)). Additionally, stream-wise ligaments are captured (Figure 4.11 (c)). The generation of stream-wise ligaments is due to three-dimensional effects.

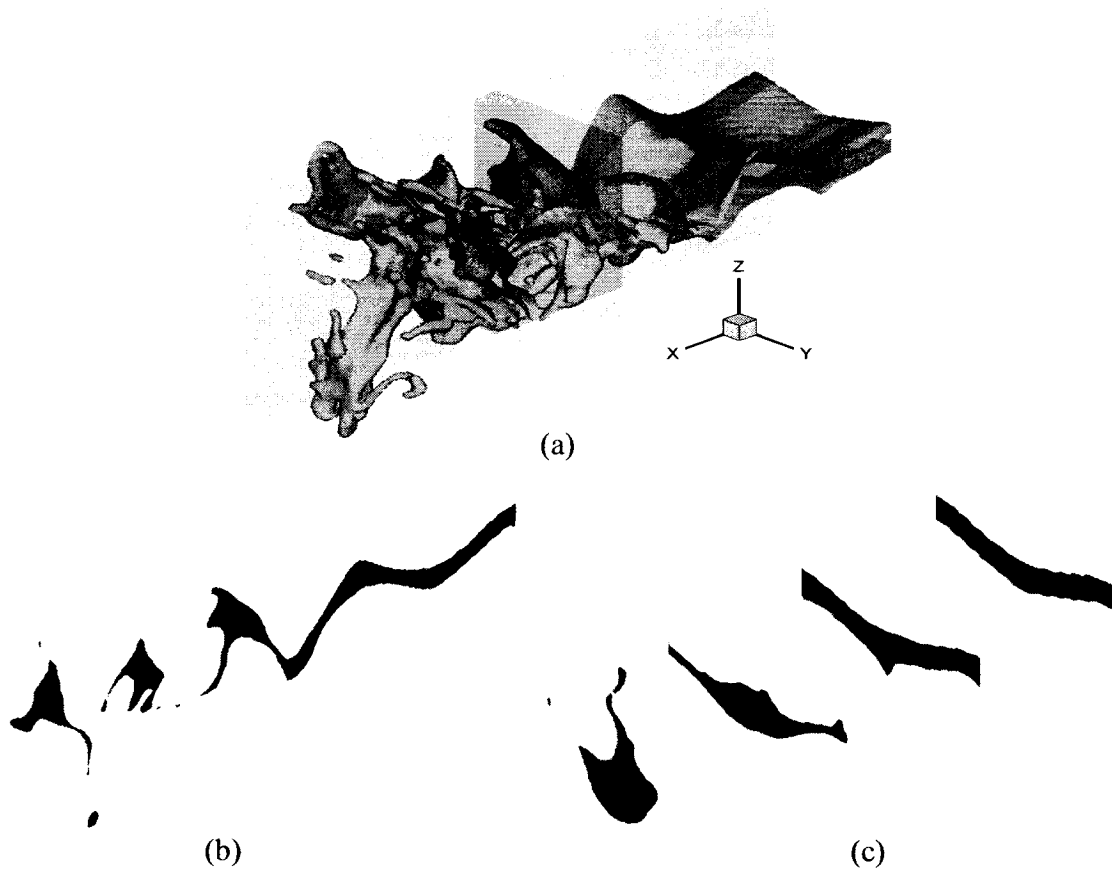


Figure 4.11: 3D liquid sheet, (a) 3D view, (b) span-wise ligaments, (c) stream-wise ligaments

To investigate how stream-wise ligaments are generated, Figure 4.12 shows velocity vectors at the cross section of the liquid sheet downstream of the nozzle exit. As indicated by circles, velocity vectors have a component in the span direction, y -direction. Since there is no initial velocity in the y -direction and the velocities induced at the liquid-gas interface by the linear stability analysis are only in the z -direction, this span-wise velocity is generated due to 3D effects. The velocity in the y -direction along with the velocity in the z -direction make pairs of counter-rotating vorticity vectors which are in the flow direction, x -direction, and are called stream-wise vorticities. These vorticities cause the liquid sheet to rotate in the flow direction and are responsible for the generation of stream-wise ligaments.

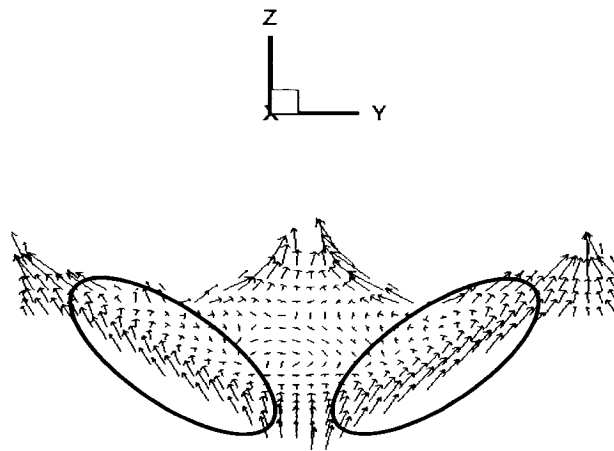


Figure 4.12: Stream-wise counter-rotating vorticities

The generation of the span-wise ligaments has been presented completely in section 4.1.2 where the 2D spatial analysis is discussed. Consequently, the remainder of this section deals with the formation of the stream-wise ligaments. Since the formation of stream-wise ligaments is due to the generation of stream-wise vorticities, the effect of fluid properties on the strength of the stream-wise vorticities, x -vorticities, is studied. The x -

vorticities would be presented at planes where the stream-wise ligaments start to form as shown in Figure 4.13.

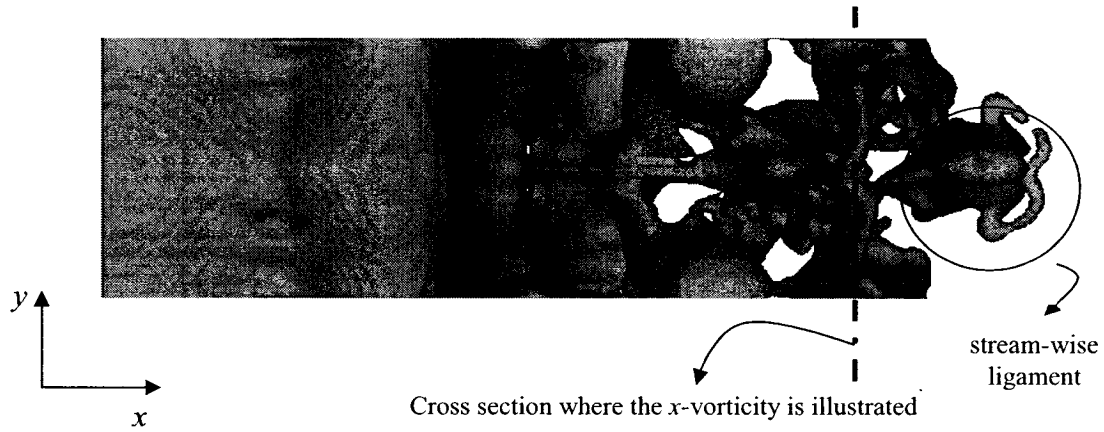


Figure 4.13: Top view of the liquid sheet

Figure 4.14 illustrates the effect of the gas to liquid density ratio on the strength of the stream-wise vorticity for $We_l=500$ and $Oh=1$. Since the dominant wavelength decreases by increasing ρ_g/ρ_l , the intensity of the x -vorticity is higher in larger gas to liquid density ratios. Figures 4.15 and 4.16 show the variation of the x -vorticity with the Weber number for two different ρ_g/ρ_l . By increasing the Weber number, the intensity of the stream-wise vorticities increase due to the higher values of the sheet velocity and smaller dominant wavelengths. The effect of the viscosity on the strength of the stream-wise vorticity is illustrated in Figures 4.17 and 4.18 for two different Weber numbers. The lower Ohnesorge numbers lead to stronger counter-rotating vorticities demonstrating the stabilizing effect of the viscosity in the spatial analysis.

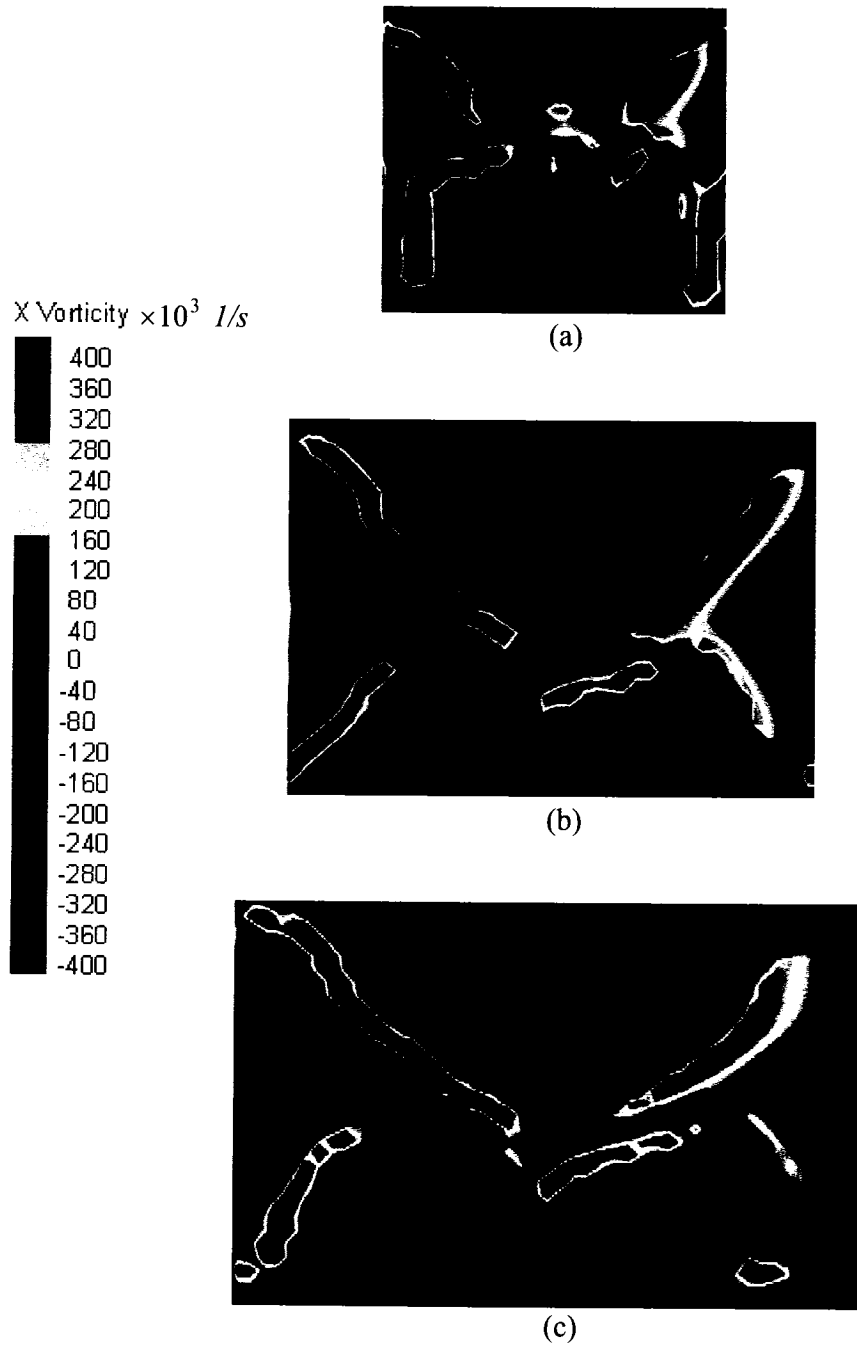


Figure 4.14: Effect of gas to liquid density ratio on the stream-wise vorticity for $We_l=500$ and $Oh=1$, (a) $\rho_g/\rho_l=1/500$, (b) $\rho_g/\rho_l=1/700$, (c) $\rho_g/\rho_l=1/800$

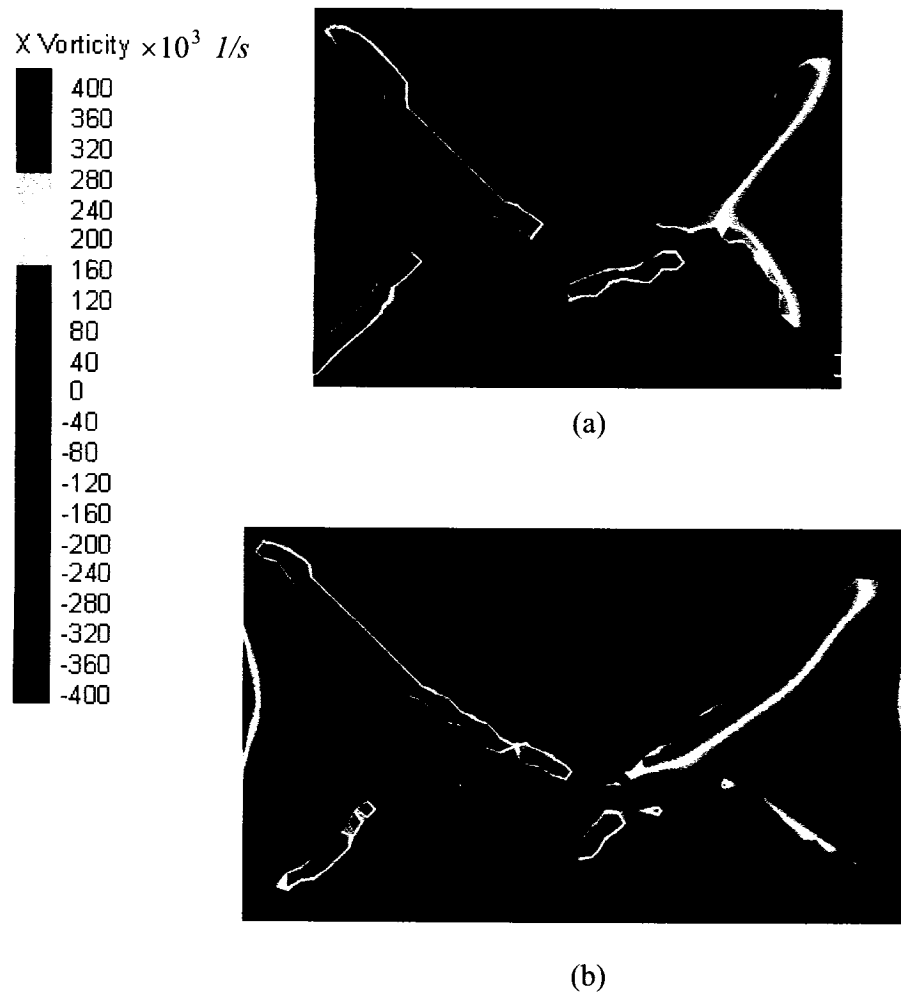
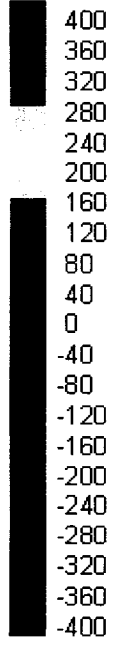
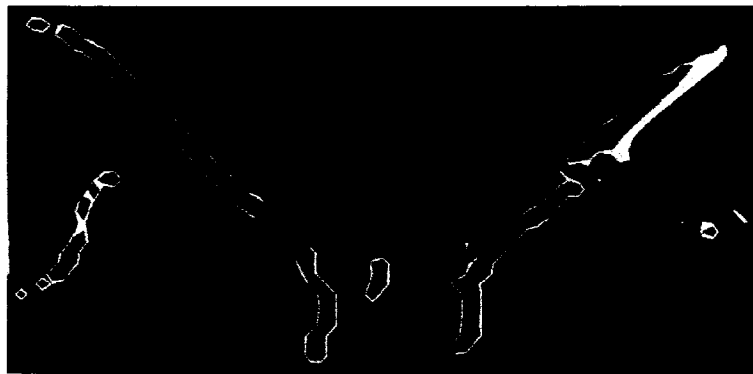


Figure 4.15: The effect of Weber number on the x -vorticity for $\rho_g/\rho_l=1/700$ and $Oh=1$,
 (a) $We_l = 500$ (b) $We_l = 400$

X Vorticity $\times 10^3$ 1/s



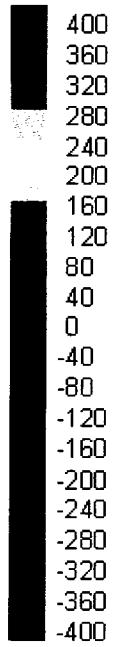
(a)



(b)

Figure 4.16: The effect of Weber number on the x -vorticity for $\rho_g/\rho_l=1/1000$ and $Oh=1$
(a) $We_l = 500$, (b) $We_l = 400$

X Vorticity $\times 10^3$ 1/s



(a)



(b)

Figure 4.17: Effect of Ohnesorge number on the x -vorticity for $\rho_g/\rho_l = 1/700$ and $We_l = 500$, (a) $Oh = 2$, (b) $Oh = 3$

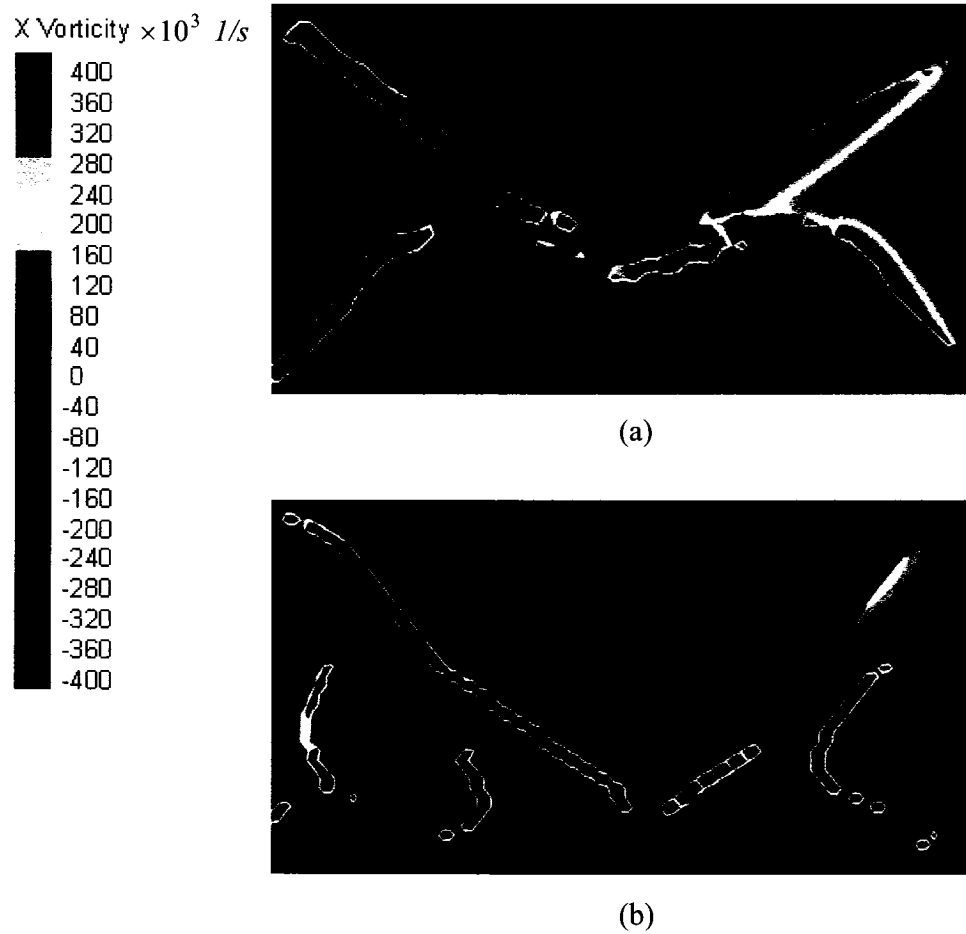


Figure 4.18: Effect of Ohnesorge number on the x -vorticity for $\rho_g/\rho_l = 1/700$ and $We_l = 300$, (a) $Oh = 2$, (b) $Oh = 3$

As mentioned in Chapter 1, liquid breakup predicted by VOF methods is mostly based on the numerical errors rising from geometric reconstruction of interfaces associated with VOF methods [26]. This section shows that implementing interface boundary condition by linear stability analysis leads to results in which the grid size is not the main source of breakup.

Table 4.3 shows the variation in the breakup length of the liquid sheet for various mesh sizes for $We_l = 500$, $Oh = 2$, $\rho_g/\rho_l = 1/1000$. Since it is more straightforward to define a unique breakup length in 2D rather than in 3D, the results are based on the 2D analysis described in section 3.2. The breakup length is presented as the time average over two period time of the moving liquid sheet. The number of cells per sheet thickness increases by refining the mesh size and keeping the sheet thickness constant. Figure 4.19 shows that the breakup length has an oscillatory behavior but the change in the breakup length is less than 13% illustrating that the mesh size is not dominant in the breakup process. This fact is a significant achievement in using VOF methods to model the breakup phenomenon as these methods are highly dependent on the grid size [26].

Computational cell per sheet thickness	Non-dimensional breakup length
5.4	34.2
6.25	36.4
7.5	35.3
8.3	33.5
9.2	33.6
10.4	32.6
11.7	32.8
12.5	31.8

Table 4.3: The effect of the mesh size on the breakup length for $We_l = 500$, $Oh = 2$, $\rho_g/\rho_l = 1/1000$

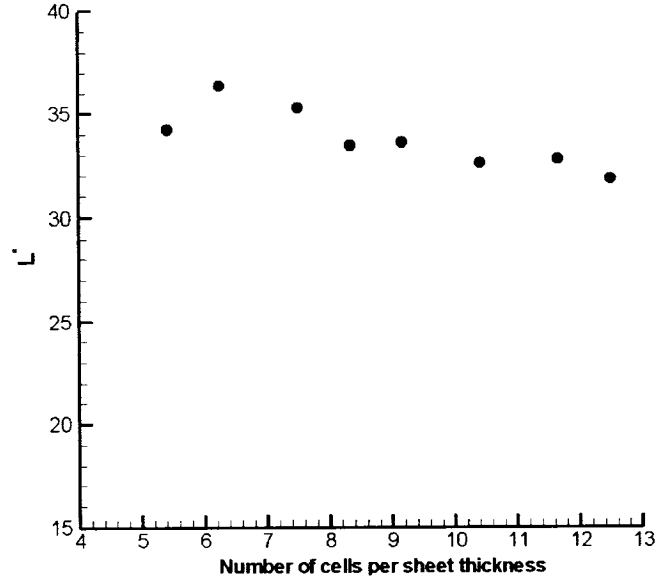


Figure 4.19: Variation of the breakup length with the mesh size

To investigate the effect of the grid size in 3D, a liquid sheet with a periodic boundary condition in the span-direction is simulated considering three different grid sizes for $We_l = 500$, $Oh = 2$, $\rho_g/\rho_l = 1/1000$. The sheet thickness is fixed in all cases. The grid sizes used are shown in Table 4.4. Case 1 represents a coarse mesh while case 3 is the finest grid size used. The top views of the liquid sheet for these three cases are shown in Figure 4.20.

	Case 1	Case 2	Case 3
Mesh size	$10 \mu m$	$8 \mu m$	$6 \mu m$
Cell per sheet thickness	5	6.5	8.3

Table 4.4: Grid size used for the mesh study

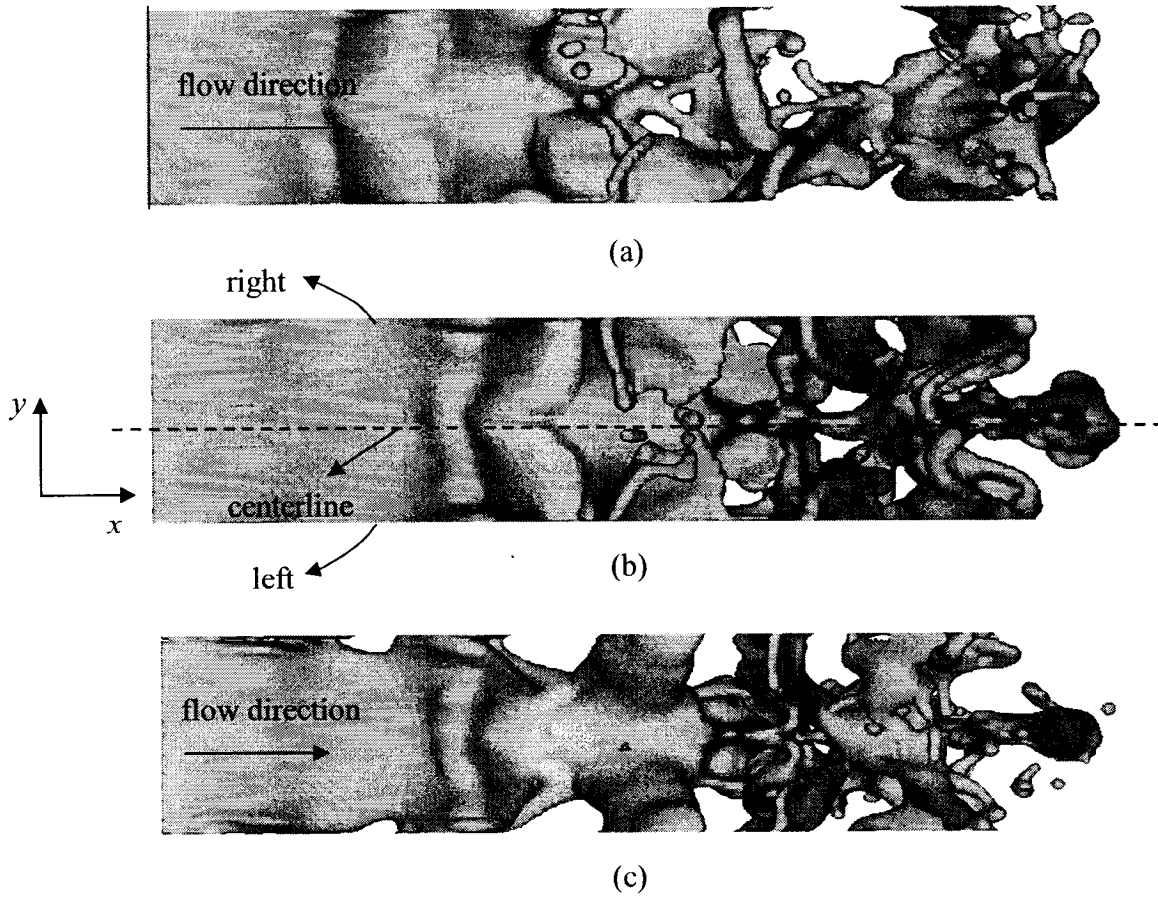


Figure 4.20: The effect of the mesh size on a 3D liquid sheet for $We_l = 500$, $Oh = 2$, $\rho_g/\rho_l = 1/1000$, (a) case 1, (b) case 2, (c) case 3

Since the boundary condition in the span direction (y -direction) is periodic, the main flow is in the x -direction, and there is no preference for the flow field at the left and right boundaries (shown in Figure 4.20 (b)), the flow should have some symmetry with respect to the centerline. As illustrated in case 1 for the coarse mesh, this symmetry is not achieved while for two other cases the flow is almost symmetric with respect to the centerline.

Based on the 2D and 3D mesh study mentioned above, it is concluded that at least providing 6-7 computational cells per sheet thickness is required for the numerical

simulation. All of the 3D results presented in this work provide 8 initial computational cells per sheet thickness with $\Delta x = \Delta y = \Delta z$.

4.3. Effect of Initial Disturbance

Inoue [16] described that the initial amplitude of the disturbances affects the final results of breakup. To investigate this effect, the breakup lengths of liquid sheets with the same flow conditions but different initial disturbances, η_0 , are compared.

Table 4.5 shows the non-dimensional breakup length for $We_l = 400$, $Oh=1$ and $\rho_g/\rho_l=1/1000$ for three different initial disturbances; $\eta_0 = 0.04\lambda_{max}$, $\eta_0 = 0.05\lambda_{max}$, and $\eta_0 = 0.06\lambda_{max}$ where λ_{max} is the most dominant wavelength. The breakup lengths are presented at three different span locations: 1/4 of the wavelength, half of the wavelength, and 3/4 of the wavelength in the span direction. These locations are shown in Figure 4.21 . Results show that the breakup length of the liquid sheet depends on the initial disturbance and decreases as η_0 increases.

	1/4 span	1/2 span	3/4 span
$\eta_0 = 0.04\lambda_{max}$	25.6	26.8	23.5
$\eta_0 = 0.05\lambda_{max}$	20.4	24.4	20.4
$\eta_0 = 0.06\lambda_{max}$	17.6	17.4	17

Table 4.5: Effect of the initial disturbance on the non-dimensional breakup length

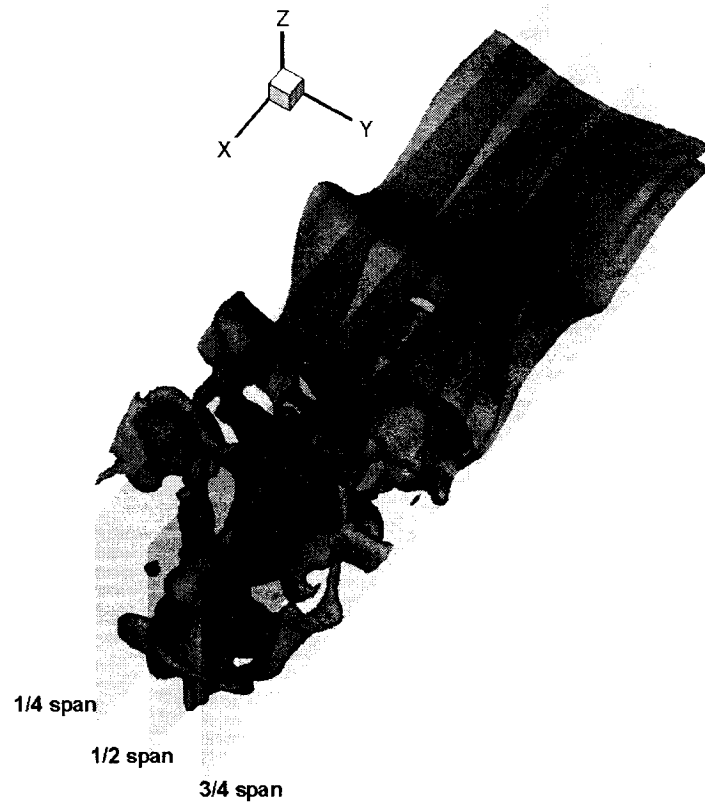


Figure 4.21: Span-wise locations used in Table 4.5

5. Closure

5.1. Conclusion

A two- and three-dimensional study of the primary breakup of liquid sheets is conducted to capture span-wise and stream-wise ligaments. A VOF-based code is used to solve governing equations for the liquid phase and to capture the interface between the liquid and surrounding gas. Since the interaction between the gas and liquid is the major source of the breakup phenomenon, the interface boundary condition is modified and it is applied using linear stability analysis.

To capture span-wise ligaments, a two-dimensional analysis is performed. This analysis includes investigating the effect of fluid properties on the breakup time and breakup length of liquid sheets. Fluid properties are grouped into three non-dimensional numbers, Weber number, Ohnesorge number and the gas to liquid density ratio. To implement appropriate interface boundary conditions to study the breakup time and breakup length, temporal and spatial linear stability analyses are performed, respectively. These analyses, find the maximum growth rate and corresponding wavelength of the most dominant wave traveling on the liquid sheet for each flow condition. These maximum values are used to implement the interface boundary condition. It is shown that the non-dimensional breakup time and length remain almost constant for different fluid properties but for the same non-dimensional numbers.

The liquid surface tension tends to stabilize the liquid sheet by increasing the breakup time. Increasing the gas to liquid density ratio decreases the breakup time. In the certain range of Weber number considered in this work, $0.1 < We_g < 0.5$, the liquid viscosity destabilizes the liquid sheet by decreasing the breakup time. The results are consistent with the work of Li et al [12].

The evolution of the liquid sheet in space is considered to investigate the effect of fluid properties on the breakup length. It is shown that both liquid surface tension and viscosity stabilize the liquid sheet by increasing the breakup length. Higher values of the gas to liquid density ratios lead to smaller breakup lengths. The results show consistency with the work of Li [13].

The study is extended to 3D to capture the stream-wise ligaments as well as the span-wise ones. The sheet is perturbed in the span-direction by a wave with a wavelength equal to that of the most dominant wave in the flow direction. However, it is shown that even without disturbances in the span-direction, span-wise disturbances are generated due to the 3D effects in addition to the effect of the free edge. To investigate the effect of flow properties on the generation of the stream-wise ligaments, a periodic boundary condition is applied in the span direction.

It is shown that stream-wise ligaments are formed due to stream-wise vorticities generated downstream of the flow. These vorticities are generated due to the coupling with span-wise vorticities. The study, concerning the effect of fluid properties on the

strength of stream-wise vorticities, shows that decreasing the liquid surface tension and viscosity and increasing the gas density, intensify the stream-wise vortices.

Finally, it is shown that using linear stability analysis to apply the interface boundary condition may lead to results in which the mesh size is not a dominant parameter controlling the breakup phenomenon. It is recommended to initially provide at least 7 computational cells to get realistic results.

5.2. Future Work

- When a liquid sheet emerges from a nozzle exit, both temporal and spatial instabilities grow simultaneously. Therefore, involving both effects in a unique analysis would lead to more realistic results. In order to apply appropriate boundary conditions at the interface, a new dispersion equation should be derived in which both the wave number and wave frequency are complex numbers and the growth rate of instabilities would be a function of both time and space.
- As mentioned in the 3D result section, the 3D effects would induce some disturbances on the liquid sheet. One issue that may be considered is that how much of these disturbances are due to the presence of the free edge. In the other words, how far the effect of the free edge can penetrate in the liquid sheet. As a preliminary study three different cases with the same flow conditions but different lengths in the span-direction are considered. The lengths considered are three, four, and five wavelengths in the span direction. The velocity vectors and x -vorticities contours are shown in

Figures 5.1 and 5.2. The left boundary is assumed to be symmetric. It can be seen that an increase in the span-length changes the shape of the velocity vectors. Further investigation of the free edge effect can be conducted as an extension to this work.

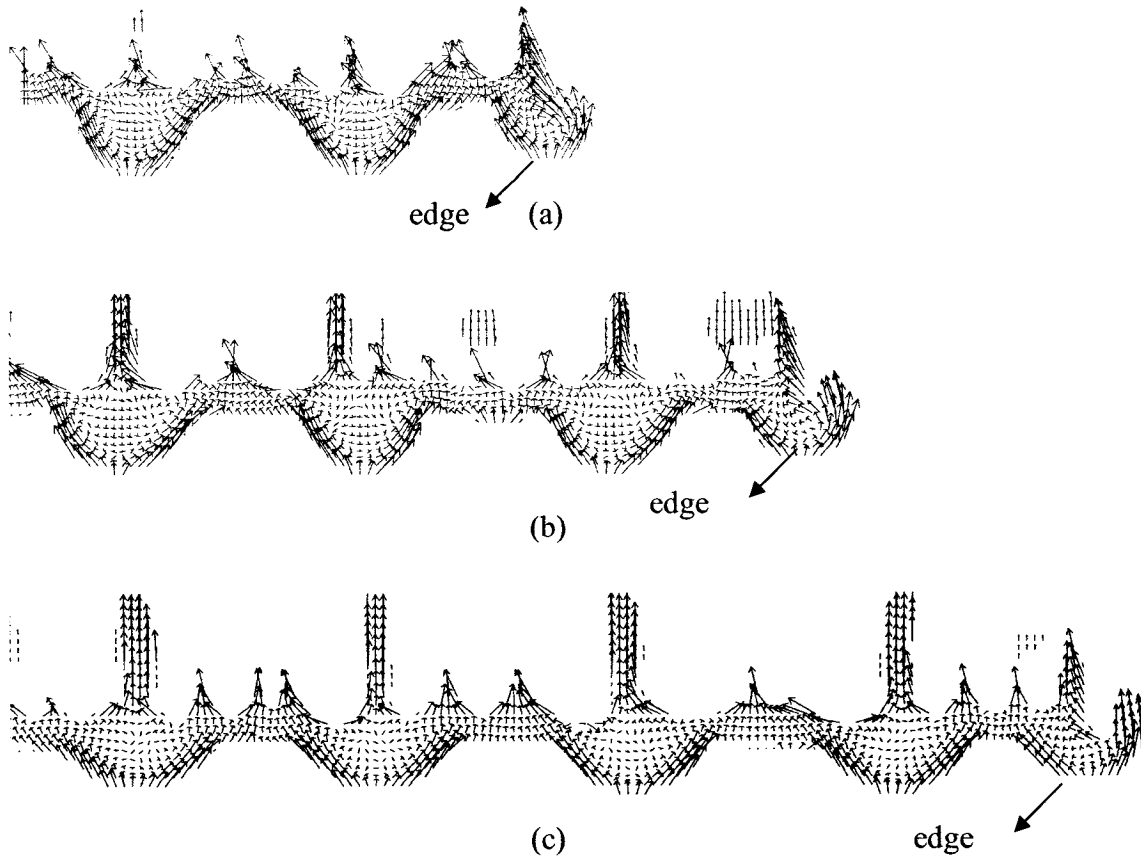


Figure 5.1: Velocity vectors for different span length, (a) three-wavelength, (b) four-wavelength, (c) five-wavelength

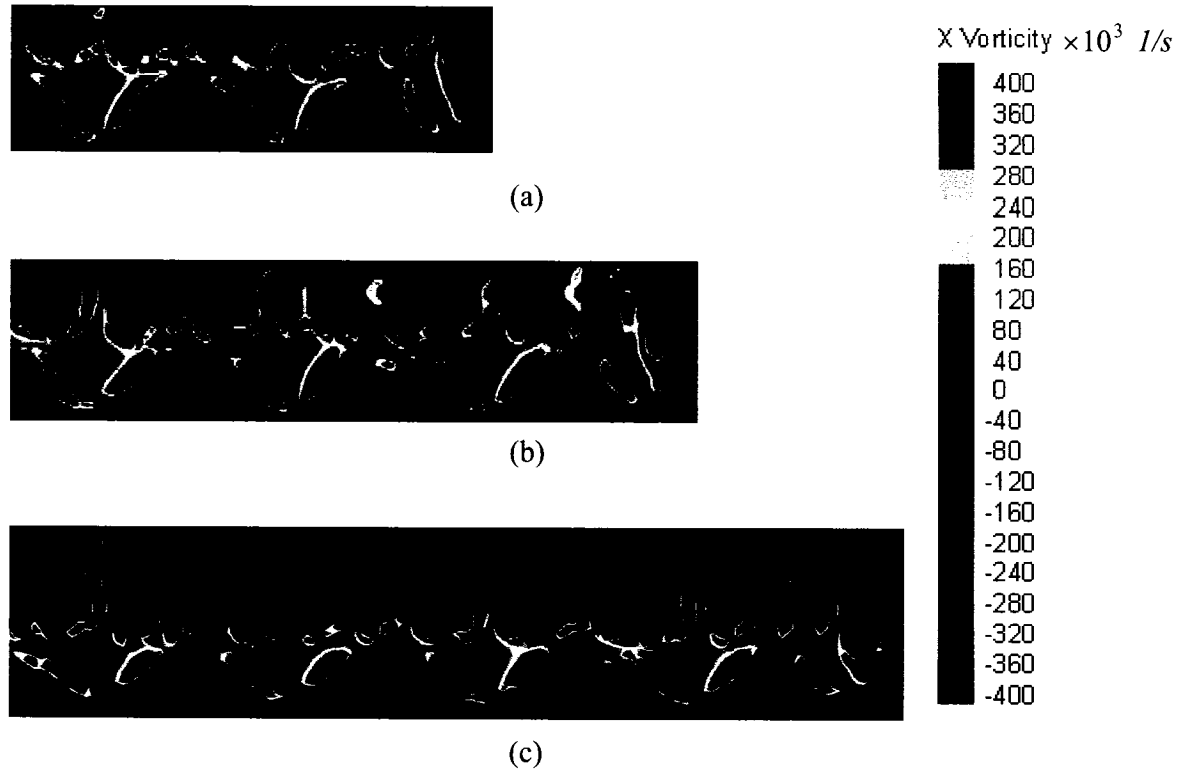


Figure 5.2: x-vorticity contour for different span lengths, (a) three-wavelength, (b) four-wavelength, (c) five-wavelength

- Primary breakup explained in this work would result in formation, velocity and size of the ligaments generated from liquid sheets. As stated in the introduction section, the next step of the breakup is secondary breakup which is the formation of smaller droplets from ligaments. The secondary breakup results in a distribution for final diameter and velocity of droplets. Results of the present work can be used in a typical spray model to track the trajectory of formed droplets. This model can include combustion phenomenon. In this case the analysis has a wide range of application in gas turbine combustion chambers and internal combustion engines.

References:

1. W.A. Sirignano, C. Mehring, “*Review of theory of distortion and disintegration of liquid streams*”, Progress in Energy and Combustion Science, 26, 2000.
2. F. M. White, “*Fluid mechanics*”, McGraw-Hill , 1986
3. L. Rayleigh, “*On the instability of jets*”, Proc. Lond. Math. Soc.
4. M. J. McCarthy, Molloy, “*Review of stability of liquid jets and the influence of nozzle design*”, Chemical Engineering Journal, 7, 1974.
5. D. B. Bogoy, “*Drop formation in circular liquid jets*”, Annual review of fluid mechanics, 11, 1979.
6. W.W. Hagerty, J.F. Shea, “*A study of the stability of plane fluid sheets*”, Journal of Applied Mechanics, 22, 1955.
7. N. Dombrowski, R. P. Fraser, “*A photographic investigation into the disintegration of liquid sheets*”, Mathematical and Physical Sciences, 247, 1954.
8. A. Mansour, N. Chigier, “*Dynamic behavior of liquid sheets*”, Physics of Fluids, 3, 1991
9. I.S. Carvalho, M.V. Heitoyr, D. Santos, “*Liquid film disintegration regimes and proposed correlations*”, International Journal of Multiphase Flow, 28, 2002.
10. B. E. Stapper, W. A. Sowa, G. S Samuelsen, “*An experimental study of the effects of liquid properties on the breakup of a two-dimensional liquid sheet*”, Journal of Engineering for Gas Turbines and Power, 114, 1992.
11. N. Dombrowski, W. R. John, “*The aerodynamic instability and disintegration of viscous liquid sheets*”, Chemical Engineering Science, 18, 1963.

-
12. X. Li, R. S. Tankin, "*On the temporal instability of a two-dimensional viscous liquid sheet*", Journal of Fluid Mechanics, 226, 1991.
 13. X. Li, "*Spatial instability of plane liquid sheets*", Chemical Engineering Science, 48, 1993.
 14. P. K. Senecal, D. P. Schmidt, I. Nouar, C. J. Rutland, R. D. Reitz, M. L. Corradini, "*Modeling high-speed viscous liquid sheet atomization*", International Journal of Multiphase Flow, 25, 1999.
 15. KIVA code, Los Alamos National Lab.
 16. O. Inoue, "*Vortex simulation of spatially growing three-dimensional mixing layers*", AIAA, 27, 1989.
 17. C. Mehring, W. A. Sirignano, "*Nonlinear capillary wave distortion and disintegration of thin planar liquid sheets*", Journal of Fluid Mechanics, 388, 1999.
 18. I. Kim, W.A. Sirignano, "*Three-dimensional wave distortion and disintegration of thin planar liquid sheets*", Journal of Fluid Mechanics, 410, 2000.
 19. F. M. White, "*Viscous fluid flow*", McGraw-Hill, 1991.
 20. S. P. Lin, Z. L. Wang, "*Three types of linear theories for atomizing liquids*", ILASS Americas Proceedings, 2006.
 21. M. Gaster, "*A note on the relation between temporally-increasing and spatially-increasing disturbances in hydrodynamic stability*", Journal of Fluid Mechanics, 14, 1962.
 22. C. W. Hirt, B. D. Nichols, "*Volume of fluid method for the dynamic of free boundaries*", Journal of Computational Physics, 39, 1981.

-
23. Ashgriz. N., Poo. J. Y., “*FLAIR: flux line-segment model for advection and interface reconstruction*”, Journal of Computational Physics, 93, 1991.
24. Glimm. J., Brayan. O. M., Menikoff. R., Sharp. D., “*Front tracking applied to Rayleigh-Taylor instability*”, SIAM Journal on Scientific and Statistical Computing, 7, 1986.
25. S. Zaleski, “*Computation of multi-phase flow by Volume of Fluid and high-order front tracking methods*”, Modélisation en Mécanique, Université Pierre et Marie Curie.
26. M. Raessi, J. Mostaghimi, M. Bussmann, “*A new method for calculating interface normal vectors and curvatures when modeling free-surface flows*”, ILASS Americas Proceedings, 2006.
27. D. L. Youngs, in: K. Morton and M. Baines, editors, “*Numerical methods for fluid dynamics*”, Academic Press, New York, 1982.
28. J. U. Brackbill, D. B. Kothe, C. Zemach, “*A continuum method for modeling surface tension*”, Journal of Computational Physics, 100, 1992.
29. D. B. Kothe, R. C. Mjolsness, “*RIPPLE: A new model for incompressible flows with surface tension*”, AIAA, 30, 1992
30. M. Bussmann, J. Mostaghimi, S. Chandra, “*On a three-dimensional volume tracking model of droplet impact*”, Physics of Fluids, 11, 1999.
31. F. H. Harlow, J. E. Welch, “*Numerical calculation of time dependent viscous incompressible flow of fluid with free surface*”, Physics of Fluids, 8, 1965
32. J. H. Ferziger, M. Peric, “*Computational methods for fluid dynamics*”, Springer, Berlin, 1997.
33. B. Van Leer, “*Toward the ultimate conservative finite difference scheme IV*”, Journal of Computational Physics, 32, 1979.

-
34. M. Bussmann, "*A three-dimensional model of an impact droplet*", PhD thesis, University of Toronto, 2000.
35. Kershaw D. S., "*The incomplete Cholesky conjugate gradient method for the iterative solution of systems of linear equations*", Journal of Computational Physics, 26, 1978.

Appendix A

For the temporal analysis of liquid sheets, periodic boundary condition is required in the moving direction. As the main flow is in the x -direction, description of implementing periodic boundary condition in this direction is presented. First it is helpful to have a quick and brief explanation about the code structure.

The computational grid consists of 3-D cubes extending in x -, y - and z -direction. Beyond the computational mesh, there are extra grids called ghost cells required to implement domain boundary conditions. Ghost cells are extended one grid besides the first and last computational mesh in each direction. Figure A.1 shows computational and ghost cells in a 2-D problem. Ghost cells are shown in the gray color. Figure A.1 also illustrates the numbering used in the code. In 3-D problems, the numbering is extended in the z -direction as well.

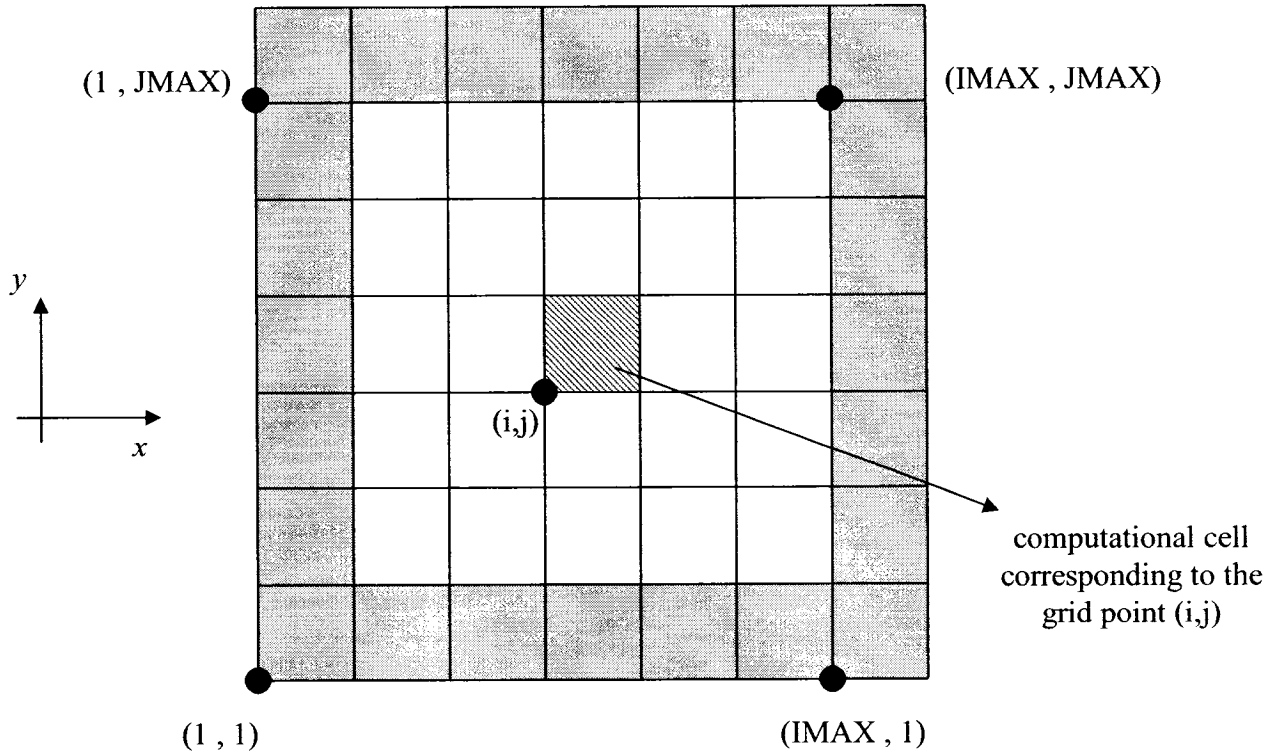


Figure A.1: Structure of computational mesh

Ghost cells located at the left and right columns of Figure A.1 are used to implement the periodic boundary conditions. For all of the left ghost cells, $i = 1, 1 < j < JMAX$ while for the right column of ghost cells, $i = IMAX, 1 < j < JMAX$.

Periodic boundary in the x -direction implies that the flow which exits from the right boundary would enter to the left boundary or vice versa with the same flow variables. To

implement this concept, the right ghost cells should be identical to the first column of computational cells in the left. As well, the left ghost cells should have the same flow variables as the first right computational cells. This concept is shown in Figure A.2.

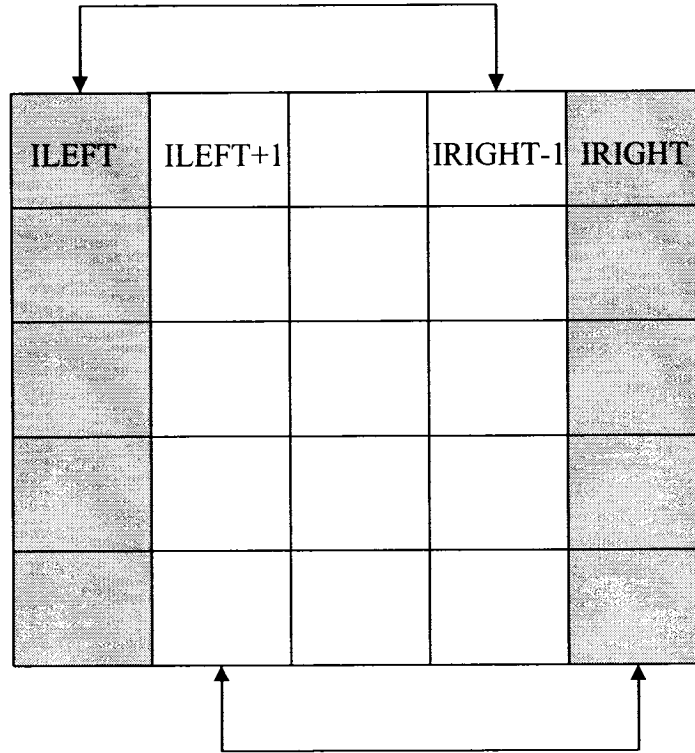


Figure A.2

The above mentioned procedure is implemented for all flow variables at left and right boundaries to apply the periodic boundary condition in the x -direction. As an example suppose a variable called F . To have periodic boundary condition in the x -direction we have:

```
DO J=1,JMAX
```

```
  F( ILEFT,J ) = F( IRIGHT-1,J )
```


$$F(\text{IRIGHT},J) = F(\text{ILEFT}+1,J)$$

END DO

where ILEFT and IRIGHT indicate ghost cells at left and right boundaries shown in Figure A.2.

After finding each variable at each computational time, the above commands are used to impose periodicity in the x -direction. As described in Chapter 2, all of the variables except pressure are found explicitly. So implementation of periodic boundary is very straightforward.

To calculate pressure, a matrix should be constructed. To form this matrix, all the neighboring cells should be identified to each computational cell. To identify the right neighbor of each cell a variable called “IJUMP” is used. The definition for this variable, the way to identify the right neighbor, has been modified to implement periodic condition in the x -direction. This modification is in such a way that at each computational row shown in Figure A.2 (j constant) the cell “ILEFT+1” is introduced as the right neighbor of cell “IRIGHT-1”.

Appendix B

In order to show that span-wise (y -direction) instabilities could be generated due to 3D and free edge effects, a case with no initial disturbance in the y -direction is studied. Figure B.1 illustrates the liquid sheet moving in the x -direction with no initial disturbance in the y -direction for $We_l = 1000$, $Oh = 1$, and $\rho_g/\rho_l = 1/1000$. It can be seen that as the liquid sheet evolves in space, instabilities are generated in the span-direction. To demonstrate the formation of these disturbances, Figure B.2 illustrates velocity vectors of the liquid sheet at four different planes shown in Figure B.1. It can be seen that the free edge and 3D effects induce instabilities in the span direction.

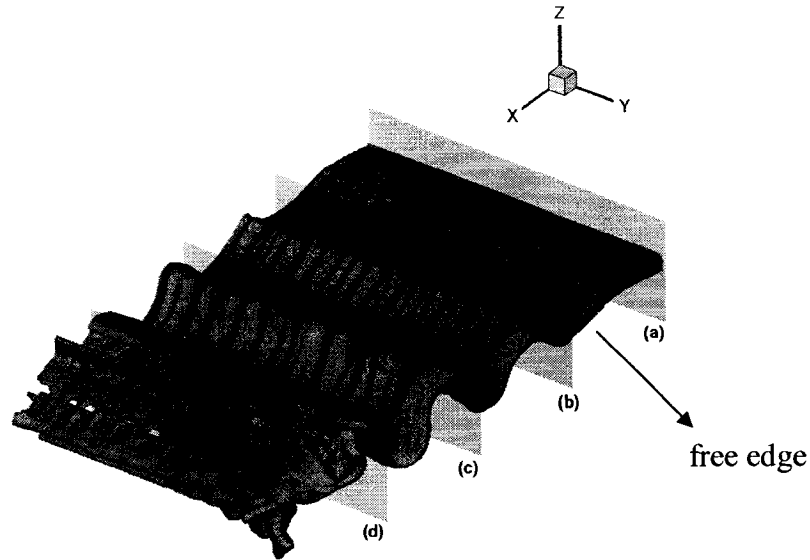


Figure B.1: Liquid sheet with no initial disturbance in y -direction

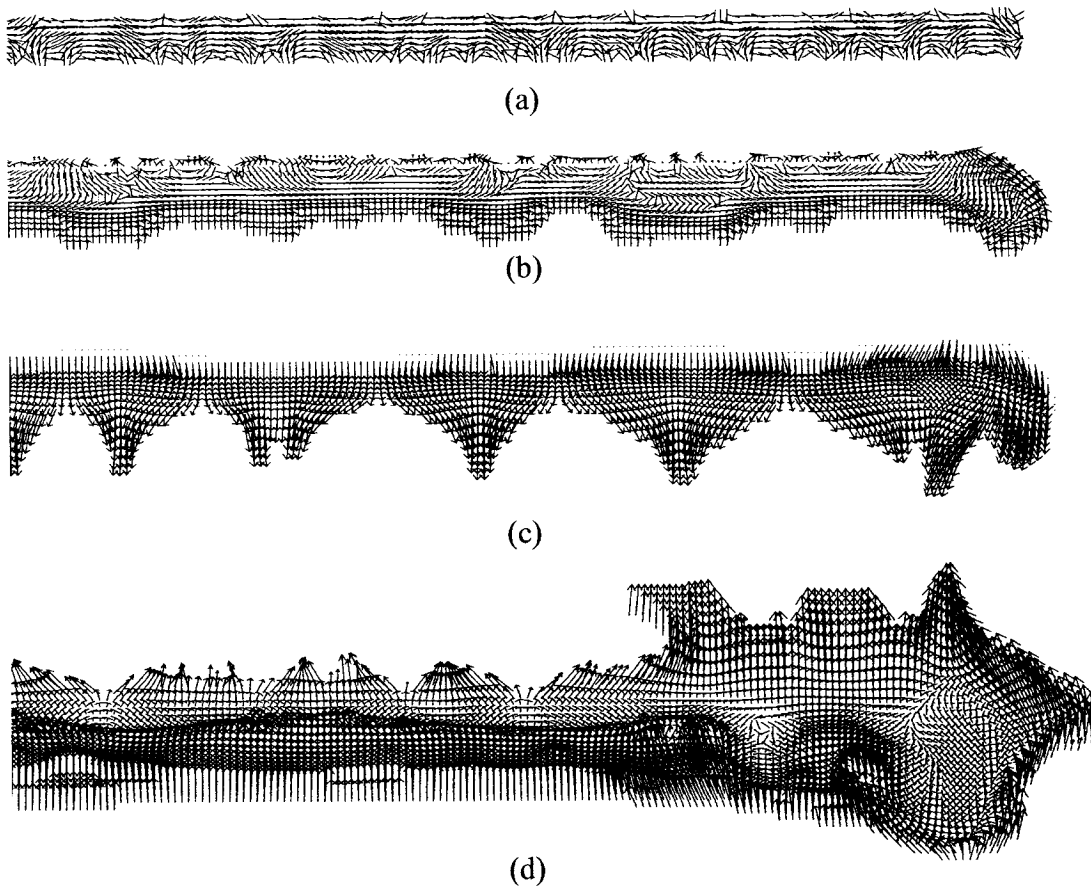


Figure B.2: Velocity vectors in cross sections of Figure B.1